ABSTRACT

Title of dissertation: Dynamics and Control of Non-Smooth Systems with Applications to Supercavitating Vehicles

Vincent Nguyen, Doctor of Philosophy, 2011

Dissertation directed by: Professor Balakumar Balachandran
Department of Mechanical Engineering

The subject matter of this dissertation relates to the dynamics of non-smooth vehicle systems, and in particular, supercavitating vehicles. These high-speed underwater vehicles are designed to have sustained vaporous or ventilated gas cavities that form over the entire vehicle. In terms of the modeling, the system non-smoothness is caused by the interaction forces generated when the vehicle contacts the cavity. These planing interactions can cause stable and unstable dynamics, some of which could be limit-cycle dynamics. Here, planing forces are considered on the basis of non-cylindrical cavity shapes that include shifts induced by the cavitator angle of attack. Incorporating these realistic physical effects into a vehicle system model generates a unique hydrodynamic non-smoothness that is characterized by non-constant switching boundaries and non-constant switched dynamics. Nonlinear stability analyses are carried out, Hopf bifurcations of equilibrium solutions are identified, and stabilizing control is investigated. Also considered is partially cavitating system dynamics, where active fin forces are used to support the vehicle. Non-steady planing is also considered, which accounts for vehicle motions into the cavity, and

this planing provides a damping-like component in the planing force formulation. Modeled with non-steady planing is a physical time delay relating to the fact that the cavity, where planing occurs, is based on the previous cavitator position and orientation data. This delay is found to be stabilizing for certain values of speed. Maneuvering is considered by using inner-loop and outer-loop control schemes. A feedback inner-loop scheme helps reject fast planing instabilities, while a numeric optimal control approach is used to generate outer-loop commands to guide the vehicle through desired maneuvers. The maneuvers are considered for operations with tight body to cavity clearance, and in which planing is prevalent. Simple search algorithms along with a penalty method for handling the constraints are found to work the best due to the complexity of the non-smooth system dynamics.

Dynamics and Control of Non-smooth Systems with Applications to Supercavitating Vehicles

by

Vincent Nguyen

Dissertation submitted to the Faculty of the Graduate School of the
University of Maryland, College Park in partial fulfillment
of the requirements for the degree of
Doctor of Philosophy
2011

Advisory Committee:
Professor Balakumar Balachandran, Chair and Advisor
Professor Shapour Azarm
Professor Amr Baz
Assistant Professor Nikhil Chopra
Professor Norman Wereley

Acknowledgments

I would like to thank Dr. Balakumar Balachandran for his guidance through this entire research process, he has always found the time to fit me into his increasingly busy schedule. I would also like to acknowledge Dr. Abraham Varghese, Dr. Guojian Lin, and Dr. Munther Hassouneh, all of whom have provided invaluable collaborations for this research. This dissertation has been made possible by the sponsorship of the U. S. Office of Naval Research (ONR) ULI Program through Award No. N000140610271 and through ONR Award No. N000140310103 with Dr. Kam Ng and Dr. Ron Joslin as technical monitors for this work. Finally, I thank my wife and my family for their continued encouragement and support.

Table of Contents

List of Tables

List of Figures

Chapter 1

Introduction and Background

Non-smooth systems can be generally defined as systems where the vector field representation of the system is non-smooth. A typical state-space representation of a system's dynamics is shown in Eq. (1.1), where x is a vector of the system states, t is time, and u represents a vector of the system inputs. By using the state-space representation, here, a non-smooth system is defined as a system where the function f is not C^1 continuous with respect to time and the states.

$$\dot{\mathbf{x}} = f(t, \mathbf{x}, \mathbf{u}(\mathbf{t})) \tag{1.1}$$

Non-smoothness can occur due to non-smooth forces, system geometry, or non-smooth inputs. When the discontinuities that cause the non-smoothness are finite and well defined, it is often helpful to treat the non-smooth system as a switched combination of smooth systems. In most systems of interest (in terms of the importance of including the non-smoothness), the dynamics of the switched systems are dramatically different. Typical examples of non-smoothness are systems with friction or impacts.

In general, vehicle systems are systems wherein a vehicle moves in space. Often times, the forces acting upon the vehicle are best defined in a moving reference frame that follows the vehicle. This is because in these systems, many of the forces relate

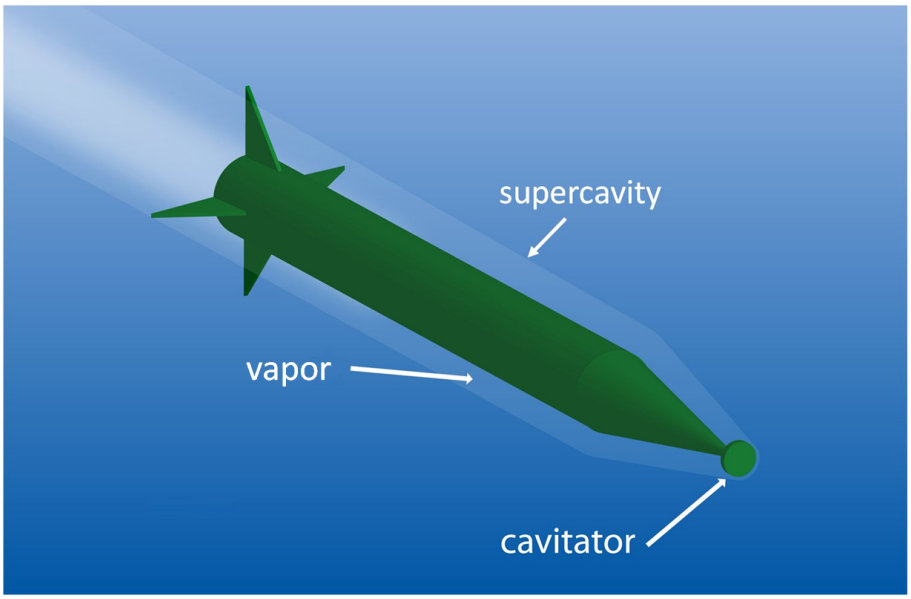

Figure 1.1: Supercavitating vehicle.

to relative positions and angles with respect to the vehicle. An example would be tire forces for a wheeled terrestrial vehicle that depend heavily on slip angles, and these are easiest defined with respect to the vehicle orientation. Another example is from flight dynamics, wherein the lift and drag forces generated from the control surfaces depend on the angle of attack.

1.1 Supercavitating Vehicles

The physical problem of interest for this work is supercavitating underwater vehicles. Cavitation is generally described as vapor bubble formation caused by pressure drops associated with a body moving in a fluid. Cavitation is generally considered as being a detrimental and corrosive process, since the effects of collapsing vapor bubbles causes damage to the body in the fluid. Collapsing bubble cavitation

is known as initial cavitation, and this type of cavitation is widely associated with pumps and propellers [5]. However, partial cavitation and supercavitation, relate to sustained cavities. Partial cavitation relates to a sustained cavity that encompasses some part of the body and supercavitation relates to a sustained cavity that encompasses the entire body [40]. This leads to supercavitating vehicles, which are high-speed underwater vehicles wherein a gas cavity surrounds the entire body of the vehicle. For these vehicles, the cavity is formed by vapor due to cavitation at the nose (created by a blunt trailing edged cavitator, Figure 1.1) and this cavity may be aided through forced ventilation. Supercavitating vehicles have the advantage of reduced drag (due to the reduction in wetted surface area), which allows for high speeds. The high-speed capabilities are particularly advantageous for weapon or counter-weapon systems, although other applications such as high-speed underwater transport have been proposed. Supercavitating vehicles face stability challenges due to the nonlinear, non-smooth planing forces that arise from interaction between the body and the cavity wall.

If the planing force function with respect to immersion is smooth (aside from at zero immersion), then the supercavitating vehicle system can be considered as a piecewise smooth system. When considering motions in the vertical plane, in a general sense, the system dynamics can be divided into three regions with the dynamics in each region individually characterized by smooth dynamics. One while planing on the top surface, one while planing on the bottom surface, and one where the vehicle is completely inside the cavity and is touching neither surface. These regions are illustrated in Figure 1.2. For the most part, the cavity will form in

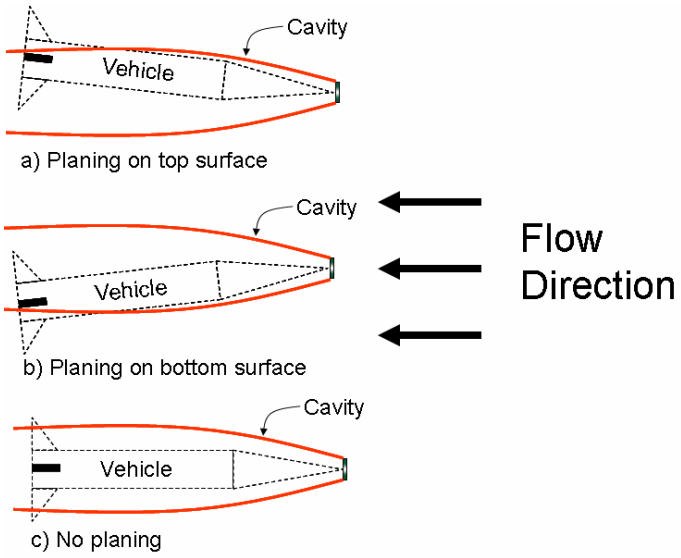

Figure 1.2: Regions of smooth dynamics.

the direction of the flow with respect to the cavitator (the cavity shift effects due to cavitator angle of attack can also play a role and this is discussed later in this work). The switching points between regions are determined by the point where the body begins to contact the cavity. For a constant cavity shape, the switching point is defined by the angle made by the body with respect to the flow. Similarly, when assuming a constant cavity shape, the planing force can also be written as a function of the angle of the body with respect to the flow, since this angle also determines the immersion area. Constant cavity approximations allow for simpler characterization of the system dynamics and they are often utilized. However, within this work, non-constant cavity shapes are considered. This inclusion creates not only non-constant switching boundaries, but also non-constant switched dynamics, since the immersed area (and hence planing force) depends on the cavity shape.

Supercavitating vehicle systems differ from the traditional impacting non-

smooth systems. The use of non-constant cavity shapes creates moving switching points and non-constant switched dynamics. In the supercavitating vehicle system, the non-smoothness is not directly position dependent as with impacting systems (instead related to the attitude of the vehicle with respect to the cavity). Additionally the planing is "soft" in that movements well into the cavity surface are allowable. The planing force formulations can also be highly complex and nonlinear, and these formulations do not lend themselves to a direct analytical treatment.

1.2 Literature Review

1.2.1 Dynamics and Control of Non-smooth Systems

Much work has been conducted in the area of non-smooth system dynamics, particularly, related to impact and friction problems. The following is a brief summary of this work.

Tao and Lewis [41] applied adaptive control techniques for systems with non-smooth nonlinearities such as backlash, dead-zone, component failure, friction, hysteresis, and saturation and time-delay effects. Adaptive control is particularly attractive for systems where non-smoothness is unknown. Neural networks and other adaptive techniques are used for fault detection, feedback control, friction compensation, and control of linear time-delay systems.

Queiroz, Malisoff, and Wolensk [38] presented a collection of research results dealing with non-smoothness in optimal control problems. Non-smoothness can arise from the system itself, or the *min* operations carried out for the optimization.

This research survey dealt with developments in mathematical control theory, optimization, and control engineering brought on by advances in non-smooth analysis. New optimality conditions for delay differential inclusions and effects of non-smooth analysis on Hamilton-Jacobi and Lyapunov function theory have been presented.

Li, Soh, and Wen [24] look at switched systems that are defined as sets of continuous variable systems with a discrete event system that controls the switching. These systems can be characterized as having non-smooth behavior. They present a cycle analysis method and some results about conditions for Lyapunov functions within each type of cycle and continuous system. A method to provide chaotic synchronization for chaos based encryption systems is also presented. Fillipov and Aizerman theories for piecewise continuous systems are presented in reference [3]. Numerical schemes for convergence, and bifurcations and chaos of a van der Pol-Duffing oscillator with columb friction are presented along with several other system examples. A collection of lecture notes for non-smooth dynamical systems is presented in reference [21]. Presented are Lyapunov exponents for non-smooth systems, Conley index theory, KAM theory, and Melnikov's method. An extension of Melnikov's method is presented in reference [2]. Here, the method is extended to study higher dimensional systems (greater than three). They are able to predict chaotic orbits for simple frictional models (stick-slip models), and attempt to apply the Melnikov method to other physical systems such as those with multi-body dynamics. Leine and Nijmeijer use convex analysis to look at the dynamics and bifurcations of non-smooth systems [23]. This combines the non-smooth mechanics approach with non-smooth dynamics analysis.

Experimental work in the area of non-smooth dynamics has also been conducted in studies [33] and [36]. These works relate to bifurcations in systems with impacting dynamics. Another study pertaining to cantilever tip impacts is presented in reference [6]. Drill-string dynamics, which include stick-slip friction interaction and impacting, is discussed in reference [25].

Much of the work in the area of mechanical non-smooth systems relates to friction and impact type dynamics. Again these studies differ from supercavitating systems due to the character of the switching boundaries, the relatively "soft" switched dynamics, and the complexity of the planing forces.

1.2.2 Trajectory Planning for Vehicle Systems

Maneuvering or trajectory planning is a question that is inherent to vehicle systems. Since motion or specific maneuvers for these systems can generally be achieved by multiple (or potentially infinite number of) control input functions, optimal control methods become important for determining "best" inputs. An optimal control approach for a flexible hull swimming vehicle is considered in reference [4]. Due to the complexity of the hydrodynamics for flexible hull vehicles, an analytic treatment is intractable. Instead a numeric genetic evolutionary algorithm is applied to effectively increase swimming performance. An optimal approach for yaw control on a four-wheel vehicle is presented in study [10]. Here, parameters of a particular control form are optimized to enhance yaw performance. A hybrid control strategy for an autonomous vehicle is considered in reference [12]. Here, feasible trajecto-

ries are carried out by lower level continuous control systems where a higher level control layer is used to choose between discrete feasible trajectories in order to optimize overall performance. This type of optimization can be applied to systems with complex dynamics since only families of feasible trajectories need to be considered. Motion planning is also discussed with the option of including obstacles or "no-fly" areas. Another similar hybrid approach is used in reference [11]. Again, since only a discrete set of feasible trajectories are being considered by the upper level control scheme, the optimal control problem can be solved in real time. Another computationally efficient optimal control problem is posed in reference [17], wherein trajectory planning is considered for an omni-directional vehicle. Here, a restricted set of allowable controller inputs is considered to reduce optimization complexity. Path following techniques for underwater vehicles are presented in references [22, 9]. In these studies, the vehicle attempts to follow a prescribed path.

1.2.3 Supercavitating Vehicle Studies

Dzielski and Kurdila present a four-state dynamic model of a supercavitating vehicle [8]. A simplified cavity model and planing force model are utilized. With this model, unstable and limit-cycle behavior can be observed, demonstrating the complex nature of the vehicle dynamics. A specific linearizing controller was also considered in which the nonlinearities were canceled leaving a controllable linear system. This approach is however specific to the model parameters and assumes exact knowledge of the system behavior. Lin, Balachandran, and Abed [30] looked

at the use of a switching controller for the same system. They also investigated the presence of bifurcation behavior in the dynamic system and presented a control method to delay an observed Hopf bifurcation which represents the onset of limit-cycle (tail slap) behavior [29]. In reference [26], Lin *et al.* present results on absolute stability for sector bounded nonlinearities, and these general results are applied to the supercavitating vehicle system. Kirschner, Rosenthal and Uhlman [20] also looked at supercavitating vehicle dynamics. In their study, the planing force is modeled as the force derived from a nonlinear, non-smooth spring and damper combination. In this work, the authors also accounted for the time delay generated by the fact that the cavity radius in the area of planing is actually a function of previous cavitator position. The effects of the time delay are closely examined in references [15] and [16]. In these studies, control efforts that work to stabilize the delay-free system are found to be ineffective in stabilizing the delayed system. And for certain operating conditions, the delay has a destabilizing effect. Guidance using a tracking method is considered in reference [43]. Simple tracking maneuvers are considered by using two outer-loop control strategies consisting of a pole placement method and receding horizon control scheme, both of which are applied to a feedback linearized system. Trajectory optimization for supercavitating vehicles is presented in references [39] and [1]. In these studies, optimal control methods are used to determine the maneuvering characteristics of supercavitating vehicles. The time-delay effect is accounted for in this work, along with fin force effects generated by the distinct individual fin immersion depths (due to the position of the vehicle inside of the cavity). The resulting maneuvers considered in this work do not involve

any planing of the vehicle. In the previous studies, a multitude of interesting and complicated dynamic behavior have been presented. *However, the cavity and planing force models are often simplified and this is one area of research intended to be pursued in this work.*

There has also been work in the area of cavity modeling. Initially cavity shapes were used to design body shapes along constant pressure surfaces [40]. There have been several analytical models developed for predicting cavity shapes. Logvinovich has presented a detailed analytical discussion of cavity shape and cavity body interactions in reference [31]. An iterative potential flow model for supercavitation is presented in studies [42] and [19]. These studies help generate a numeric model for cavity shape given cavitator and flow parameters. Partial cavity dynamics are significantly more difficult to model since the body protrusion greatly affects the cavity shape. Several schemes are outlined in reference [40]. However, all of these methods for approximating partial cavity shapes are based on supercavitating cavity models. A numeric potential flow model for partial cavity shapes is presented in reference [44].

Another area of development for supercavitating vehicles is with the planing forces generated by the body-cavity interactions. Analytical planing force models are presented in references [32], [37], and [14]. Since planing for supercavitating vehicles deals with non-flat surfaces, experimental testing is complicated and data are limited. Some model validations have been conducted [7].

1.3 Contributions

The first aim of this work to better characterize the non-smoothness in the supercavitating vehicle system and explore the resulting dynamics. In all of the previous research, cylindrical cavities without cavitator angle of attack shift effects are assumed in order to simplify planing force calculations. In this work, a method to allow for non-cylindrical shifted cavities is presented. This introduces more physically realistic force modeling, which however dramatically changes the nature of the non-smooth forces. This creates a "soft" non-smoothness with non-constant switching boundaries and switched dynamics. Dynamics and bifurcations of system responses are explored for these systems as well as stabilization techniques.

A partially cavitating vehicle dynamics model is presented in an effort to move towards full mission modeling, from launch (no cavitation), to partial cavitation (partially wetted vehicle), to full supercavitation. This is also an area of research not accounted for in any of previous research studies. Without the planing forces at the rear of the vehicle, it is found that a more active fin input is required to stabilize the vehicle.

Another item overlooked in much of the previous research is non-constant planing. In an effort to reduce the complexity of the planing formulation, steady planing force models (not accounting for vehicle motions into or out of the cavity) are often utilized. In this work, a model that accounts for these "impacting" forces is presented. Within this model development, a full description of the origins of the immersion depth and immersion rate terms has been provided for use in the planing

force formulation. This is an aspect that has been overlooked in much of the previous literature, and these terms have been previously presented in a somewhat arbitrary manner. Through careful representation of the immersion terms, time-delay effects can also be properly included in this impacting model. The time delay is introduced by the fact that the cavity at the rear of the vehicle (where planing is present), is generated by a previous cavitator position and orientation. In this delayed and impacting model, the time delay is found to be stabilizing for certain cavity sizes. This is a observation that is contradictory to the findings of previous time-delay studies.

All of these modeling efforts are meant to more properly characterize the physical non-smoothness present in these systems. In addition to the dynamics and stability observations made for these systems, maneuvering is also considered in this dissertation effort. Maneuvers are presented by defining specific ending conditions given a particular initial condition. A numeric optimal control approach is utilized to find control inputs that accomplish the maneuvers in the quickest possible time. Unlike other optimal control studies for supercavitating vehicles [1, 39], maneuvers in this work are considered for operation regions where non-smooth interactions are prevalent (such as speeds where the cavity-body clearances are tight). The resulting maneuvers inherently include planing. This introduces a great deal of complexity, especially, since the instabilities that these vehicle systems demonstrate stem from the vehicle-cavity interactions. An inner-loop control scheme and an outer-loop control scheme are proposed, wherein a inner feedback loop helps stabilize the planing motions of the vehicle, while the outer-loop guides the vehicle towards the desired

end condition. This control configuration works well with the inner-loop rejecting the fast timescale instabilities not addressable by the coarse outer-loop control. The non-smoothness in this system is fairly complex, with dramatically different dynamics when planing (versus not planing), and small windows of operation (due to tight body-cavity clearances) which leads to rapid switching between different dynamics. With such complicated dynamics, simple search algorithms that are coupled with optimization constraints (determined by the direct integration of the dynamics) handled as penalties, work the best for solving the optimal control problem. This approach could be extended for use for other complicated non-smooth vehicle systems.

1.4 Dissertation Objectives and Organization

The overall goal of the work is to achieve a better understanding of the dynamics of supercavitating vehicles, and by extension, illustrate a method to analyze the dynamics of other non-smooth systems. Specific objectives include the following:

1. Examine the dynamics of supercavitating vehicles by considering cavity models that incorporate realistic physical effects

2. Examine the dynamics of partially cavitating vehicles

3. Examine the dynamics of a time delayed, non-constant planing, supercavitating vehicle system

4. Examine the maneuvering capabilities for supercavitating vehicles and provide a framework to evaluate maneuvering for other complicated, non-smooth vehicle systems.

The rest of this dissertation is organized as follows. In Chapter two, dynamics of systems using shifted cylindrical cavities are discussed. This includes a description of the the basic dynamics model as well as a planing force formulation that is used throughout the rest of the work. In Chapter three, a method for accounting for non-cylindrical cavities is introduced, along with dynamics results for these systems that can be compared with previous research findings. Included are non-smooth bifurcations and methods of stabilizing the vehicle motions for the non-cylindrical cavity system. Additional modeling aspects are addressed in the following chapter. Here, vehicle dynamics for partial cavities, and an impacting time-delayed model are presented. Maneuvering on the basis of an optimal control approach is discussed in Chapter five. Here, maneuvers are considered for the previously discussed systems, as well as for a six degree-of-freedom system, by using a numeric optimal control approach that has been tailored to deal with the non-smooth vehicle dynamics. This is followed by a summary of the contributions and a discussion of potential future directions. Appendices related to this dissertation are included at the end to provide additional details and representative algorithms used in the present work

Chapter 2

Vehicle Dynamics with Cylindrical Shifted Cavities

In much of the previous vehicle system analysis, the cavity is assumed to be of cylindrical form [1, 8, 15, 16, 29, 30, 39]. In these studies, a closed-form solution for the cavity radius at the rear of the vehicle is utilized to generate an approximate cylindrical cavity for planing force calculations. In these formulations, the influence of the cavitator angle of attack on the cavity radius are ignored. In this chapter, a different cavity model is presented that allows for the inclusion of cavitator angle-of-attack effects, which are incorporated as a shift to the nominal cavity radius. The cylindrical assumption is maintained in order to highlight the cavity shift effects. A more accurate shifted non-cylindrical cavity planing (utilizing the entire cavity profile) is then considered in the following chapter.

To help illustrate the different approaches for modeling vehicle-cavity interactions, three different scenarios are illustrated in Figure 2.1. In part a), a vehicle orientation is shown with a typically assumed cylindrical cavity. The cylinder radius is determined by an estimate of the nominal cavity radius at the rear of the vehicle. The vehicle body is depicted to be entirely within the cavity. The same body orientation with a shifted cylindrical cavity, is shown in part b). As illustrated, the cavitator angle-of-attack can shift the cavity location at the rear of the vehicle which affects when planning occurs and how much immersion is present when

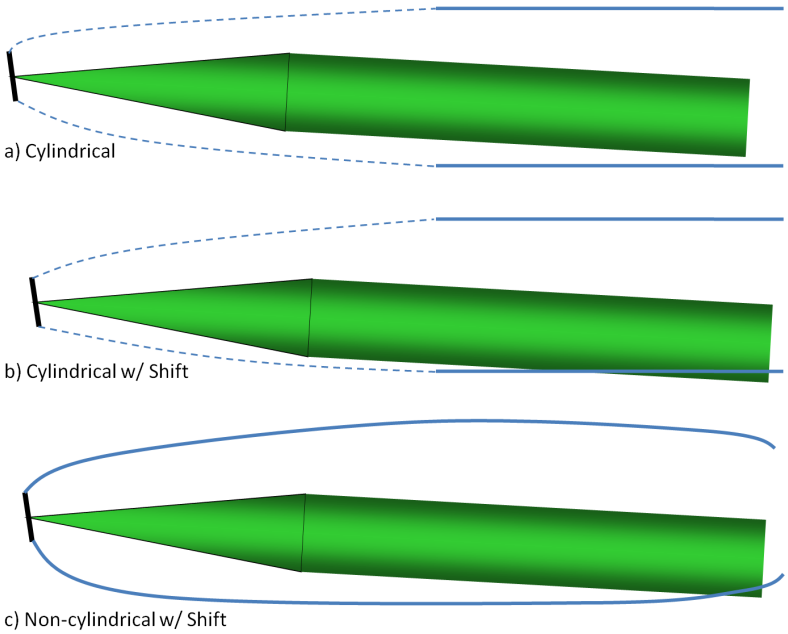

Figure 2.1: Three different scenarios in modeling body-cavity interactions: a) vehicle within a cylindrical cavity, b) vehicle within a cylindrical cavity with shifted axis, and c) vehicle within a non-cylindrical cavity.

planing. A shifted full non-cylindrical cavity is shown in part c). The immersion at the rear of the vehicle is the same as with the shifted cylindrical cavity (since the shifted cylindrical cavity radius and position is determined by the size and position of the non-cylindrical cavity at the rear). However, the immersed volume is different, which changes the planing forces due to immersion.

2.1 Basic Dive-Plane System Model

The dive-plane system model described in this section introduces a basic vehicle dynamics representation that is used as a basis for the subsequent system models presented in this work. The basic dive-plane system model comes from references

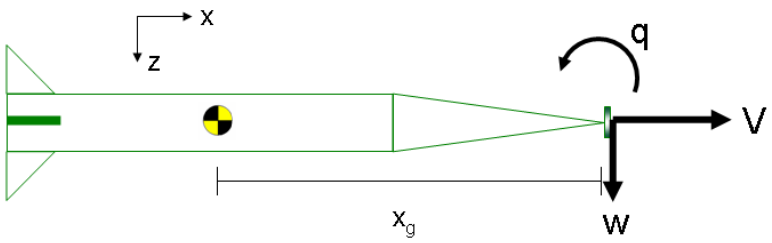

Figure 2.2: Coordinate system definition for system model.

[29] and [30], and this model is based on a model originally presented in reference [8]. The model is comprised of four states defined in a non-inertial reference frame which accounts for two-dimensional ridged body movements in the dive-plane. The dive-plane is defined as the plane formed by the vertical axis (as described by gravity direction) and the vehicle velocity vector. The vehicle's forward velocity, V, is assumed constant, and the model tracks the vertical position, z, the transverse speed, w, along with the pitch angle, θ, and the pitch rate q. The transverse speed, w, is at the cavitator and is defined as being perpendicular to the vehicle axis. The coordinate system is attached to the moving vehicle and its orientation along with the speed direction definitions are shown in Figure 2.2. The control action is made up of the cavitator and fin deflection angles, δ_c and δ_e, respectively. The lift force generated by the control elements are approximated to be linearly related to their angle of attack with respect to the flow. The variable n is the ratio of lift effectiveness between the fins and cavitator, and m represents the density ratio of the body with respect to the surrounding water. Along with some additional small angle assumptions, the equations of motion are represented as shown in Eqs. (2.1) - (2.4). The first matrix term in Eq. (2.1) includes effects due to body orientation

and the coordinate system. The second term incorporates the effect of the control action. The third matrix includes the effect of gravity. The system is linear with the exception of the planing force term, F_p, and the fourth matrix takes into account this nonlinear and non-smooth planing force that occurs when the body contacts the cavity wall. In this representation, the planing force is taken as a point force applied at the end of the vehicle.

$$\begin{pmatrix} \dot{z} \\ \dot{w} \\ \dot{\theta} \\ \dot{q} \end{pmatrix} = \begin{pmatrix} 0 & 1 & -V & 0 \\ 0 & a_{22} & 0 & a_{24} \\ 0 & 0 & 0 & 1 \\ 0 & a_{42} & 0 & a_{44} \end{pmatrix} \begin{pmatrix} z \\ w \\ \theta \\ q \end{pmatrix} + \begin{pmatrix} 0 & 0 \\ b_{21} & b_{22} \\ 0 & 0 \\ b_{41} & b_{42} \end{pmatrix} \begin{pmatrix} \delta_e \\ \delta_c \end{pmatrix} + \begin{pmatrix} 0 \\ c_2 \\ 0 \\ 0 \end{pmatrix} + \begin{pmatrix} 0 \\ d_2 \\ 0 \\ d_4 \end{pmatrix} (-V^2[1 - (\frac{R_c - R}{h'R + R_c - R})^2]\frac{1 + h'}{1 + 2h'}\alpha) \tag{2.1}$$

$$\begin{aligned} a_{22} &= \frac{CVT}{m}(\frac{-1-n}{L})S + \frac{17}{36}nL \\ a_{24} &= VTS(C\frac{-n}{m} + \frac{7}{9}) - VT(C\frac{-n}{m} + \frac{17}{36})\frac{17}{36}L^2 \end{aligned}$$

$$
\begin{aligned}
a_{42} &= \frac{CVT}{m}(\frac{17}{36} - \frac{11n}{36}) \\
a_{44} &= \frac{-11CVTnL}{36m} \\
b_{21} &= \frac{CV^2Tn}{m}(\frac{-S}{L} + \frac{17L}{36}), \quad b_{22} = \frac{-CV^2TS}{mL} \\
b_{41} &= \frac{-11CV^2Tn}{36m}, \quad b_{42} = \frac{17CV^2T}{36m} \\
c_2 &= g, \quad d_2 = \frac{T}{m}(\frac{-17L}{36} + \frac{S}{L}), \quad d_4 = \frac{11T}{36m} \\
S &= \frac{11}{60}R^2 + \frac{133L^2}{405}, \quad T = \frac{1}{7S/9 - 289L^2/1296} \\
C_x &= C_{x0}(1+\sigma), \quad C = 0.5C_x\frac{{R_n}^2}{R^2} \\
R_c &= R_n\sqrt{0.82\frac{1+\sigma}{\sigma}}K_2, \quad K_1 = \frac{L}{R_n(\frac{1.92}{\sigma} - 3)} - 1 \\
K_2 &= \sqrt{1 - (1 - \frac{4.5\sigma}{1+\sigma}){K_1}^{40/17}} \\
\dot{R}_c &= \frac{-\frac{20}{17}(0.82\frac{1+\sigma}{\sigma})^{0.5}V(1 - \frac{4.5\sigma}{1+\sigma})(K_1)^{23/17}}{K_2(\frac{1.92}{\sigma} - 3)}
\end{aligned}
\tag{2.2}
$$

$$
h' = \begin{cases} 0 & \frac{R_c - R}{R} > \frac{L|w|}{RV} \\ \frac{L|w|}{RV} - \frac{R_c - R}{R} & \text{otherwise} \end{cases}
\tag{2.3}
$$

$$
\alpha = \begin{cases} \frac{w - \dot{R}_c}{V} & \frac{w}{V} > 0 \\ \frac{w + \dot{R}_c}{V} & \text{otherwise} \end{cases}
\tag{2.4}
$$

The body is represented as a conical section followed by a cylindrical section, as shown in Figure 1.1. In this formulation, the cavity is approximated as a cylinder with a radius equal to the cavity radius at the rear of the vehicle, and the planing is approximated as a cylindrical body planing on a cylindrical cavity surface. The cavity radius at the rear of the vehicle is calculated by using a formulation that depends only on the cavitation number, σ, and the cavitator radius. The cavitation

number is a non-dimensional term that determines the extent of the cavitation, and this number is defined according to Eq. (2.5). In this expression, ρ represents the fluid density, V is the vehicle velocity, p_∞ is the ambient fluid pressure, and p_c is the cavity pressure. The model is run with a vaporous cavity, and since the fluid and cavitator parameters are constant, the cavity radius which is considered to depend only on the forward speed of the vehicle which (within each simulation run), is constant. In this form, the influence of the cavitator angle of attack on the cavity radius are neglected.

$$\sigma = \frac{p_\infty - p_c}{0.5\rho V^2} \tag{2.5}$$

The planing force function is shown in Eqs. (2.3)-(2.4). The planing force is a non-smooth function since there is no force when the vehicle is not in contact with the cavity wall. The quantity h', which represents the immersion depth, is the source of the non-smoothness. The $\dot{R}_c$ is the cavity closure rate (at the rear of the vehicle), which is included as a correction factor to the angle of immersion, α. By using the cylinder-cylinder assumption, the planing force can be determined as a function of the angle of the flow velocity with respect to the body. Since forward speed is constant, this angle can be determined from the transverse speed. A representation of the planing force with respect to the transverse speed is shown in Figure 2.3.

This system can show unstable behavior when no control is present [8], [27]. By using a simple linear feedback controller, stable limit cycles can be observed [8], [27]. The control law is shown in Eqs. (2.6), and only the cavitator deflection angle

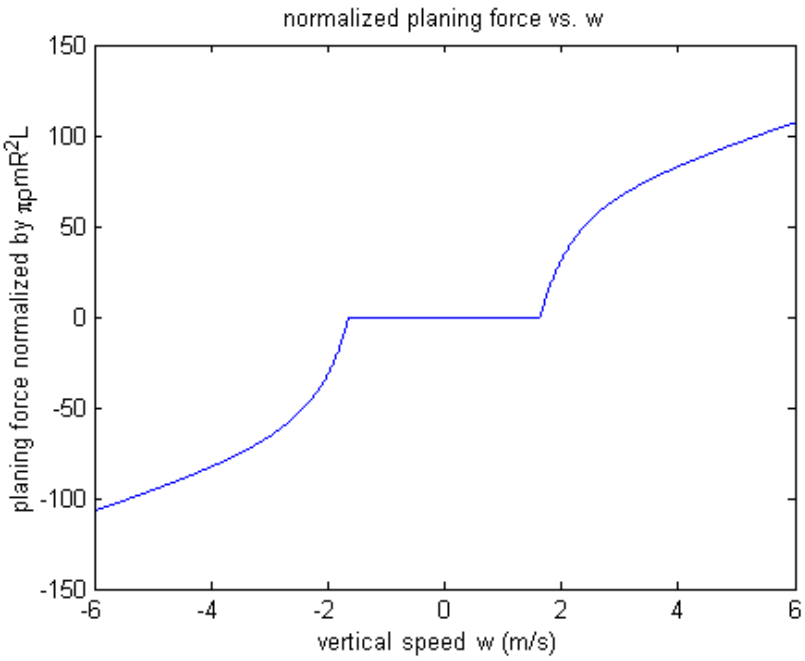

Figure 2.3: Original planing force versus transverse speed.

is varied while holding the fin deflection constant at 0.0 *radians*. The transverse velocity, w is not utilized in the feedback formulation since it is difficult to measure in an actual application. A simulation was run by using the following parameters: $g = 9.81\ m/s^2$, $m = 2$, $R_n = 0.0191\ m$, $R = 0.0508\ m$, $L = 1.8\ m$, $V = 70.9740\ m/s$, $\sigma = 0.0335$, $n = 0.5$, and $C_{x0} = 0.82$. The vehicle parameters are chosen to match those used in the previous literature [8, 29, 30]. The results obtained are presented in Figure 2.4. Since the model assumes constant forward speed (with respect to the vehicle axis), the transverse speed, w, defines the velocity angle with respect to the body. Limit-cycle motions about the $w = 0$ axis indicate the potential for two-sided tailslap behavior where the vehicle contacts both the top and bottom surfaces during the oscillatory motion. The two-sided planing can be confirmed for

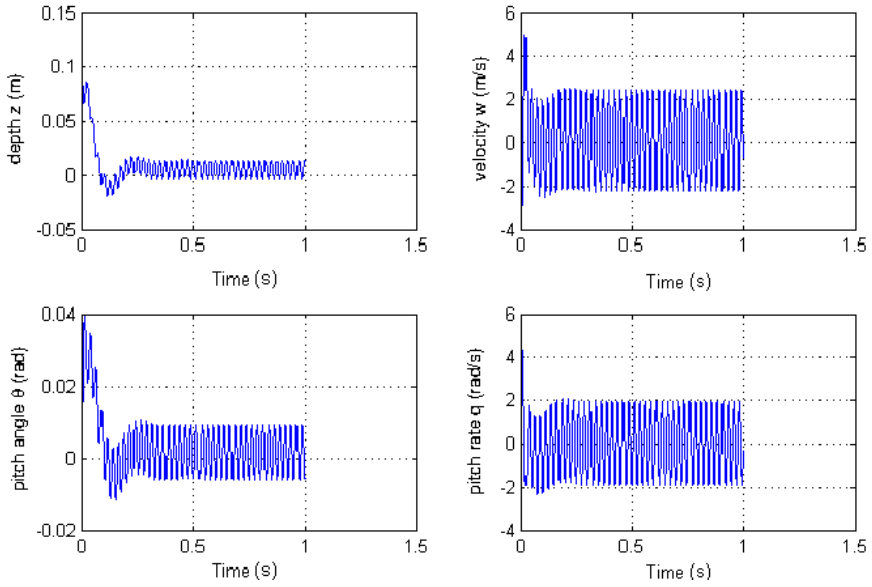

Figure 2.4: Simulation run demonstrating limit-cycle behavior with original cavity model and planing force formulation; controlled case.

this simulation run by tracing the vehicle and cavity motions.

$$\begin{aligned} \delta_e &= 0 \\ \delta_c &= 15z - 30\theta - .3q \end{aligned} \tag{2.6}$$

2.2 Integration of Numeric Cavity Model

The first item modified is the cavity model. The original model uses a closed-form solution for the cavity radius. The numeric cavity model described in references [19, 42] is then implemented. The cavity model utilizes an iterative potential flow solver. The cavitation number and cavitator shape (disc) is input into the numeric

model and the entire non-dimensional (normalized with respect to cavitator diameter) cavity shape for axis-symmetric flow (no angle of attack for the cavitator) is predicted.

The cavitator angle of attack also affects the cavity shape, and since the cavity model only provides the shape of the cavity for an axi-symmetric flow, the angle of attack effects are included as a refinement to the axi-symmetric data. This refined cavity shape is calculated as a shift of the axi-symmetric data produced by the cavity model. The shift factor is a term derived from Logvinovich [31], and this factor is based on the principle that the momentum created by the cavitator lift applies an equal and opposite momentum upon the wake. The shift can be expressed as in Eq. (2.7), where W_y expresses the lift force along the transverse direction (with respect to the flow), and R represents unshifted the cavity radius. The transverse lift force W_y can then be expressed as in Eq. (2.8). In this expression, α represents the cavitator angle of attack (with respect to the flow), D_n represents the cavitator diameter, and C_d represents the coefficient of drag for axi-symmetric flow.

$$shift(x) = -\frac{W_y}{\pi\rho V^2}\int_0^x \frac{ds}{R(s)^2} \tag{2.7}$$

$$W_y = sin(\alpha)\cdot cos(\alpha)\frac{1}{2}\rho\pi\frac{D_n^2}{4}C_d \tag{2.8}$$

When normalized with respect to D_n, the shift can be expressed as in Eq. (2.9). Here the $'$ designation refers to the non-dimensional form, so that $shift' = shift/D_n$, $R' = R/D_n$, and $x' = x/Dn$. The cavity model generates the non-dimensional axi-symmetric cavity profile, $R'(x')$, as well as the coefficient of drag, C_d. The

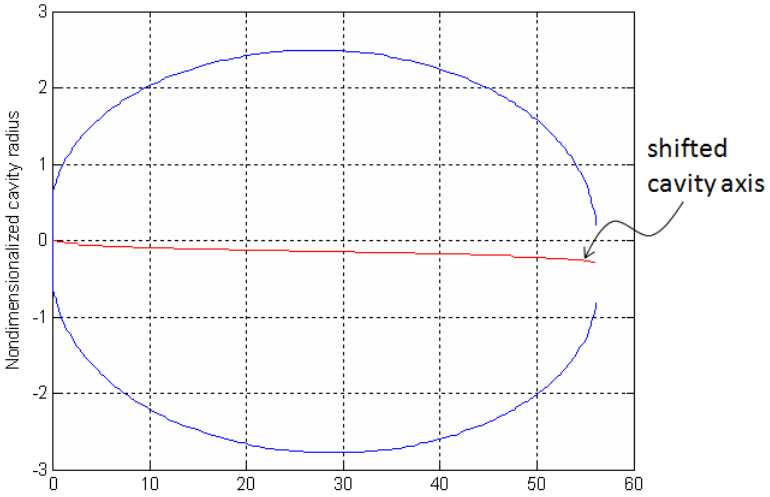

Figure 2.5: Non-dimensional cavity shape with angle of attack effects.

non-dimensional cavity profile for non-axi-symmetric flow can then be expressed by adding the shift, as in Eq. (2.10). The inclusion of the cavity shift introduces non-symmetry and cavity radius dependence on the states and control. An example of the cavity shift is shown in Figure 2.5. The flow direction is taken along the positive x-axis and an angle of attack of 10 *degrees* is assumed.

$$shift'(x) = -\frac{C_D}{8} sin(\alpha) cos(\alpha) \int_0^{x'} \frac{ds}{R'(s)^2} \tag{2.9}$$

$$R'_{shifted}(x) = R'(x) + shift'(x) \tag{2.10}$$

For the following simulation run, the original planing force formulation is retained. The original model assumed a cylindrical cavity shape; so as before, only the cavity radius at the rear of the vehicle (at distance of L) is considered. However, the entire cavity profile from the numeric model (as well as the C_D) is needed to calculate the shift associated with the angle of attack. The cavitator angle of attack

is dependent on both the states (which determines the angle of attack of the body with respect to the flow) and the control (cavitator angle of attack with respect to the body). The cavity radius is no longer constant and varies throughout the simulation. Additionally, since the shift is non-symmetric, the cavity shape is not symmetric, and a distinction must be made between planing on the top surface or bottom surface.

2.2.1 Simulation Runs with Numeric Cavity Model

The simulations were run with the same parameters as in the initial simulation; that is, $g = 9.81\ m/s^2$, $m = 2\ kg$, $R_n = 0.0191\ m$, $R = 0.0508\ m$, $L = 1.8\ m$, $V = 70.9740\ m/s$, $\sigma = 0.0335$, $n = 0.5$, and $C_{x0} = 0.82$. The results are presented in Figure 2.6 and a qualitative difference in the system behavior is evident. Limit cycles are not present. This is partially related to the difference in the nominal (unshifted) cavity radius calculated from the numeric model. A comparison of the cavity radius versus cavitation number is shown in Figure 2.7. The numeric model provides a larger cavity radii than the original model. The larger radius creates a larger cavity to body clearance at a given speed (cavitation number). The larger cavity to wall clearance is enough to transition the system out of the limit cycle region when the original run parameters are used. It should be noted that the new cavity model does not eliminate limit-cycle behavior in all scenarios. If the speed were decreased, or the body radius increased (to cause lower body to wall clearances), limit cycles can be observed. Limit-cycle observations will be discussed in a subsequent section.

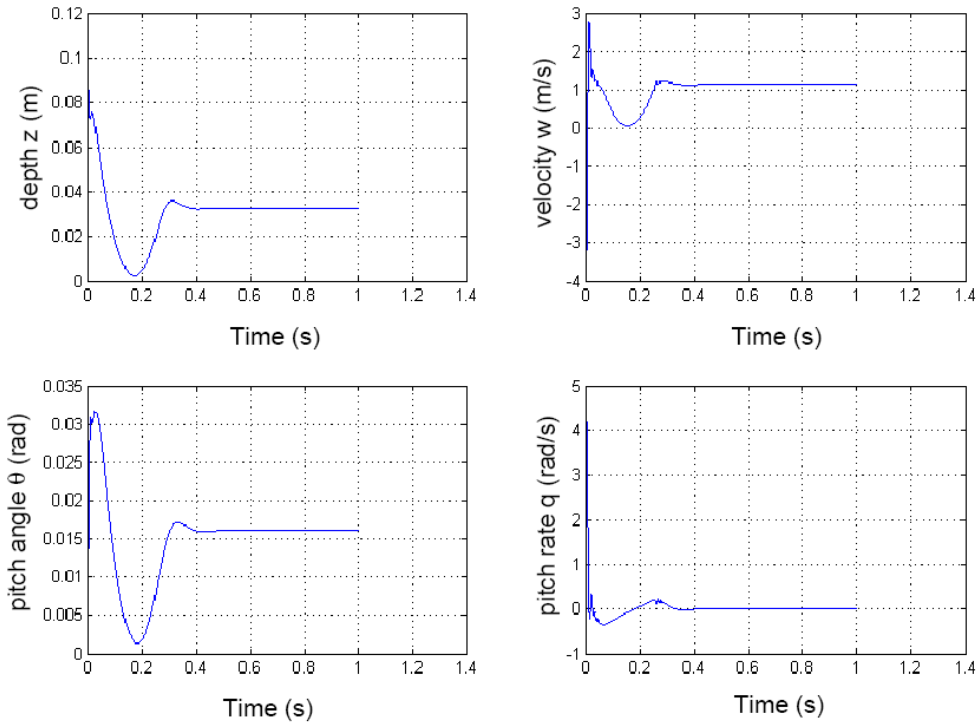

Figure 2.6: Simulation run with numeric cavity model and original planing force formulation with linear feedback.

However, the qualitative difference in behavior when using the same run parameters, does show the significance of the cavity model. Angle-of-attack effects can be seen in Figure 2.8, wherein the effective cavity radius (depending on top or bottom planing) observed during the simulation is shown.

2.3 Planing Force Model

The second item to be refined is the planing force formulation. Three planing force models were investigated. The models were developed by Hassan [14], Logvinovich [32], and Paryshev [37]. Dzielski presents an interpretation of the three

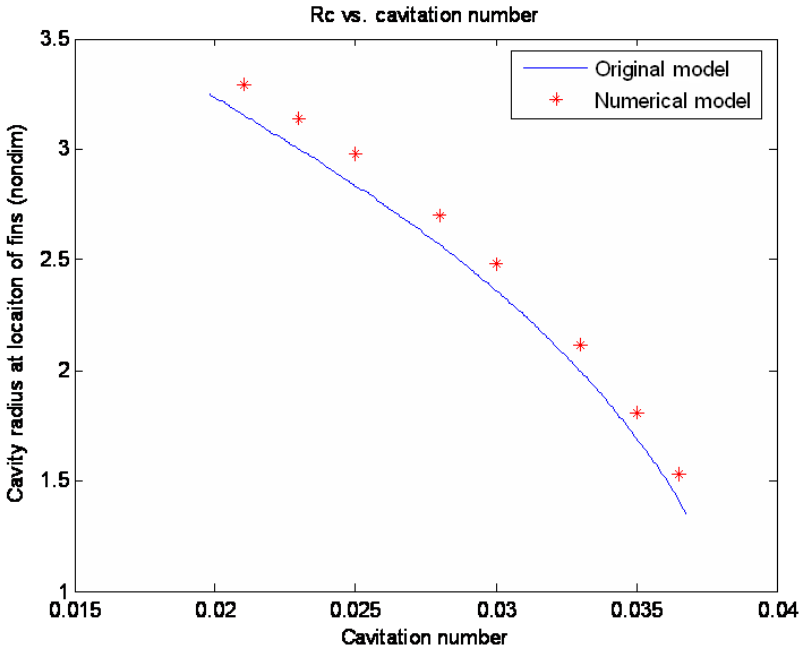

Figure 2.7: Cavity radius versus cavitation number as obtained from the cavity model used in earlier studies [8, 29, 30] and the numerical model. Planing force direction convention taken with respect to the positive transverse velocity direction w.

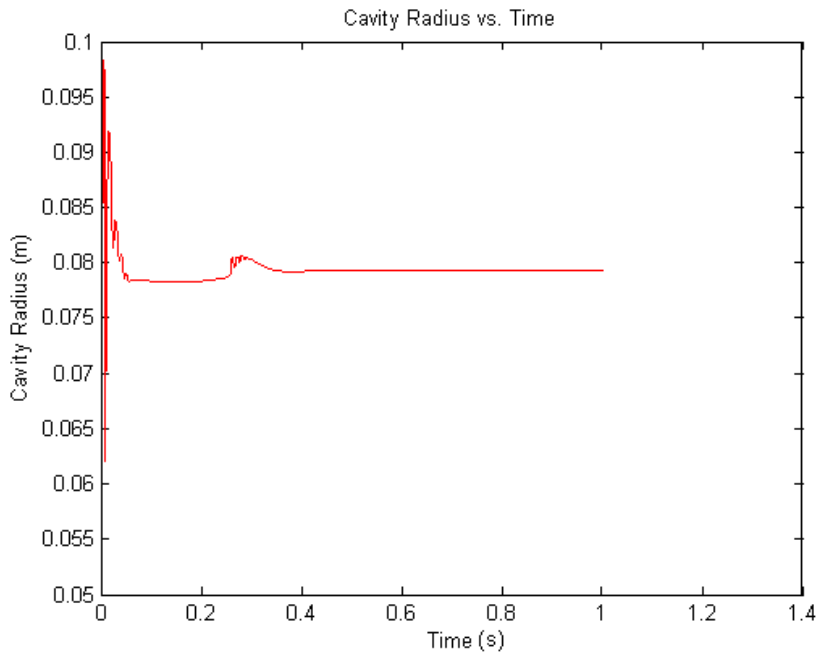

Figure 2.8: Effective cavity radius (depending on top/bottom planing) versus time for simulation run by using numeric cavity model with angle of attack effect.

approaches in relation to a cylinder planing on a cylindrical surface [7]. Given the definition of terms provided in Figure 2.9, the apparent mass can be calculated according to Eq. (2.11), where $\Delta = R - r$. The Hassan and Logvinovich models make use of m_L^* as the apparent mass, while the Paryshev model makes use of m_P^*. The derivative with respect to h is then taken, and Eq. (2.12) is used in integrating the planing force. For a cylinder planing on a cylinder, Eq. (2.13) represents the planing force. A closed-form solution for the integral can be found for the Hassan and Paryshev models. The Hassan model simplifies to the planing force model used in the previous works (as presented in the previous section). The Paryshev solution for the cylinder-cylinder case is given in Eq. (2.14), where X_P is the force centroid.

$$
\begin{aligned}
m_L^* &= \pi\rho R^2 \left(1 - \left(\frac{\Delta}{\Delta + h}\right)^2\right) \\
m_P^* &= \pi\rho r^2 h \left(\frac{2\Delta + h}{(\Delta + h)^2}\right) \qquad (2.11) \\
\frac{dm_L^*}{dh} &= 2\pi R^2 \Delta^2 (\Delta + h)^{-3} \\
\frac{dm_P^*}{dh} &= 2\pi r^2 \Delta^2 (\Delta + h)^{-3} \qquad (2.12) \\
F_H &= \left[\int_0^{h_0/tan(\alpha)} \frac{dm_L^*}{dh} dx\right] \left(\frac{r + h}{r + 2h}\right) \dot{h}^2 \\
F_L &= \left[\int_0^{h_0/tan(\alpha)} \frac{dm_L^*}{dh} \left(\frac{r + h}{r + 2h}\right) dx\right] \dot{h}^2 \\
F_P &= \left[\int_0^{h_0/tan(\alpha)} \frac{dm_P^*}{dh} dx\right] \dot{h}^2 \qquad (2.13)
\end{aligned}
$$

$$
\begin{aligned}
F_P &= \pi\rho r^2 V^2 sin(\alpha) cos(\alpha) \left(1 - \frac{\Delta^2}{(h_0 + \Delta)^2}\right) \\
X_P &= \left(\frac{h_0}{tan(\alpha)}\right) \left(\frac{h_0 + \Delta}{h_0 + 2\Delta}\right) \qquad (2.14)
\end{aligned}
$$

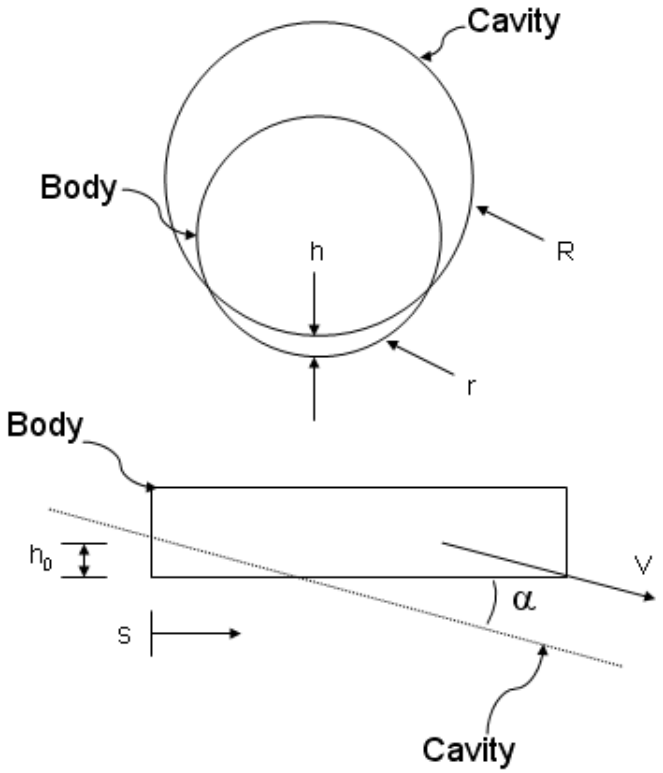

Figure 2.9: Diagram of a cylinder planing on a cylindrical surface.

The three methods provide different planing forces. A comparison of the planing force results (in relation to w in the system model) is shown in Figure 2.10. The Logvinovich results were calculated by using a numerical integration. Both Paryshev and Logvinovich produce higher planing forces than the planing formulation used in the original model. The Paryshev method was chosen for integration into the model since it was shown to better fit experimental results for both static and dynamic planing [7].

All of these planing force representations are for steady planing (no body acceleration or velocity into or out of the fluid). A derivation of the Paryshev

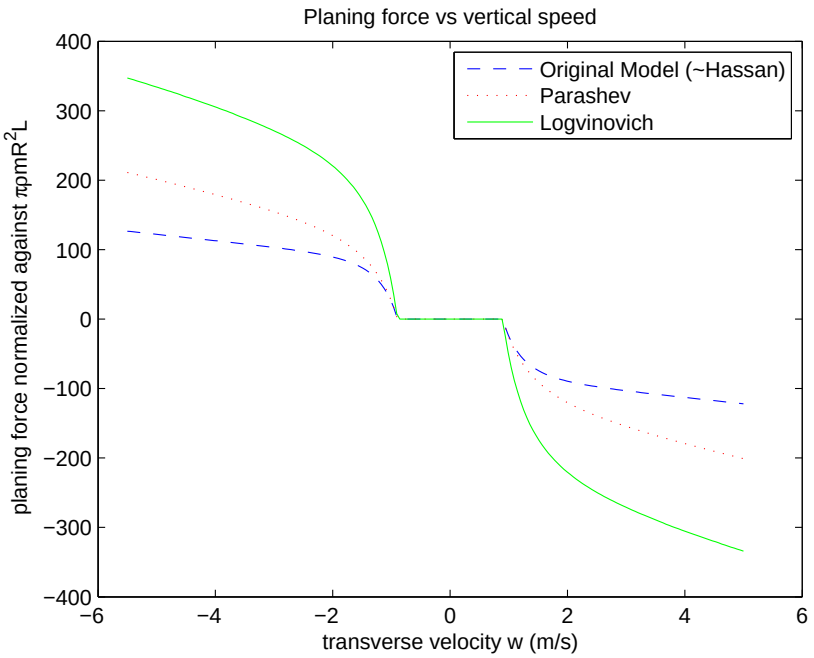

Figure 2.10: Comparison of planing force models for cylindrical cavity shapes.

planing force model as applied in this dissertation is presented next.

2.3.1 Paryshev Planing Force

Paryshev defines the forces on an expanding cylinder planing on a cylindrical cavity. The force per unit length is given by the rate of change of momentum of the fluid displaced by the planing cylinder. This is shown in Eq. (2.15), where m_y^* represents the apparent mass due to the planing, and m_R^* is the apparent mass due to the expansion of the cylinder. For the supercavitating vehicle dynamics, the contribution of the m_R^* can be ignored since the radius of the body does not change. The expression for the force can then be expanded as shown in Eq. (2.16). If only steady planing is considered (there is no acceleration into or out of the fluid) the

second term involving $\frac{dV_y}{dt}$ can be dropped.

$$f = \frac{d}{dt}\left(m_y^* V_y + m_R^* \tilde{V_R}\right) \tag{2.15}$$

$$f = \frac{dm_y^*}{dt} V_y + m_y^* \frac{dV_y}{dt} \tag{2.16}$$

The expression for the apparent mass m_y^* is given in Eq. (2.17), and this expression is a function of the immersion depth h. The gap Δ is defined as $\Delta = R - r$. The rate of change of the apparent mass m_y^* can then be described as shown in Eq. (2.18). Again, since the radius of the body does not change, the gap is constant with time, so $\frac{d\Delta}{dt} = 0$. The term, $\frac{dm_y^*}{dh}$, can be expressed as in Eq. (2.19). The total planing force can then be determined by integrating over the entire wetted area as represented as in Eq. (2.20), with $V_y = \dot{h}$.

$$m_y^* = \pi \rho r^2 h \left(\frac{2\Delta + h}{(\Delta + h)^2}\right) \tag{2.17}$$

$$\frac{dm_y^*}{dt} = \frac{\partial m_y^*}{\partial h}\frac{dh}{dt} + \frac{\partial m_y^*}{\partial \Delta}\frac{d\Delta}{dt} \tag{2.18}$$

$$\frac{dm_y^*}{dh} = 2\pi r^2 \rho \Delta^2 (\Delta + h)^{-3} \tag{2.19}$$

$$F_P = \int \frac{dm_y^*}{dh} \dot{h}^2 ds \tag{2.20}$$

For the case of a cylindrical cavity, the planing force can be integrated over the planing area and the obtained solution is given in Eq. (2.21). In these equations, h_0 is the immersion depth at the aft of the vehicle, as shown in Figure 2.9. The immersion rate term $\dot{h}$ can be expressed as $V sin(\alpha)$. The force centroid can also be calculated, as shown in Eq. (2.22), with X_P measured from the aft of the vehicle.

Again, the Paryshev planing force representation was chosen, as it has been shown to provide a better fit to experimental planing force data [7].

$$F_P = \pi\rho r^2 V^2 sin(\alpha)cos(\alpha)\left(1 - \frac{\Delta^2}{(h_0+\Delta)^2}\right) \quad (2.21)$$

$$X_P = \left(\frac{h_0}{tan(\alpha)}\right)\left(\frac{h_0+\Delta}{h_0+2\Delta}\right) \quad (2.22)$$

2.4 Simulation Results with Numeric Cavity Model and Paryshev Planing Force Formulation

By utilizing the new cavity and planing force representations additional simulations can be carried out. The same parameters as used in the previous simulation runs are utilized, $g = 9.81\ m/s^2$, $m = 2\ kg$, $R_n = 0.0191\ m$, $R = 0.0508\ m$, $L = 1.8\ m$, $V = 70.9740\ m/s$, $\sigma = 0.0335$, $n = 0.5$, and $C_{x0} = 0.82$. The same linear feedback control law is implemented as given by Eqs. (2.6), where only the cavitator is actuated and the fins are assumed to be passive. The same parameters are utilized to present a direct comparison with the previous simulation run shown in Figure 2.4, where two-sided tailslap behavior is observed.

The simulation results are presented in Figure 2.11. At steady state, limit-cycle oscillations are observed. The steady-state oscillations in w do not cross the $w = 0$ axis. Assuming a small cavity shift, this indicates that there is no two-sided tailslap behavior (oscillations where the cavity boundaries are crossed on both sides). The cavity and supercavitating body motions can be tracked to confirm that the oscillations are indeed only about the bottom planing surface. The lack of two-

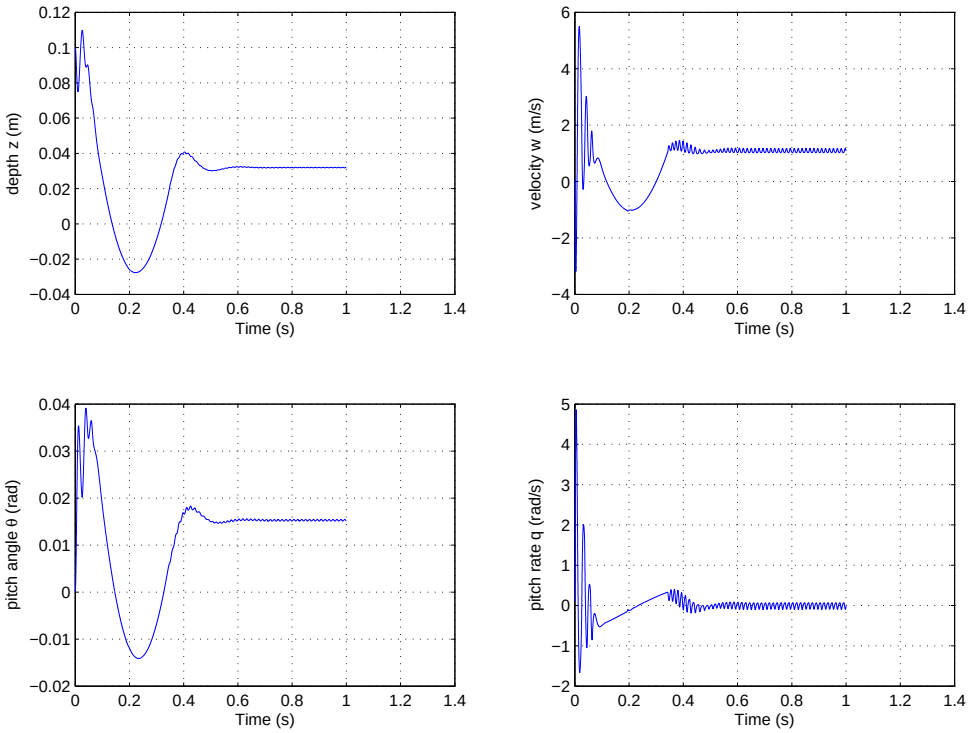

Figure 2.11: Results obtained with cylindrical planing force formulation and linear feedback.

sided tailslapping is due to the different cavity and planing force models used here. As discussed in the previous section, the cavity model used in this effort provides a slightly larger nominal (un-shifted) cavity radius than that used in the previous studies [8, 29, 30] (Figure 2.7), and the increased cavity to body clearance is partially responsible for inhibiting the two-sided tailslap behavior.

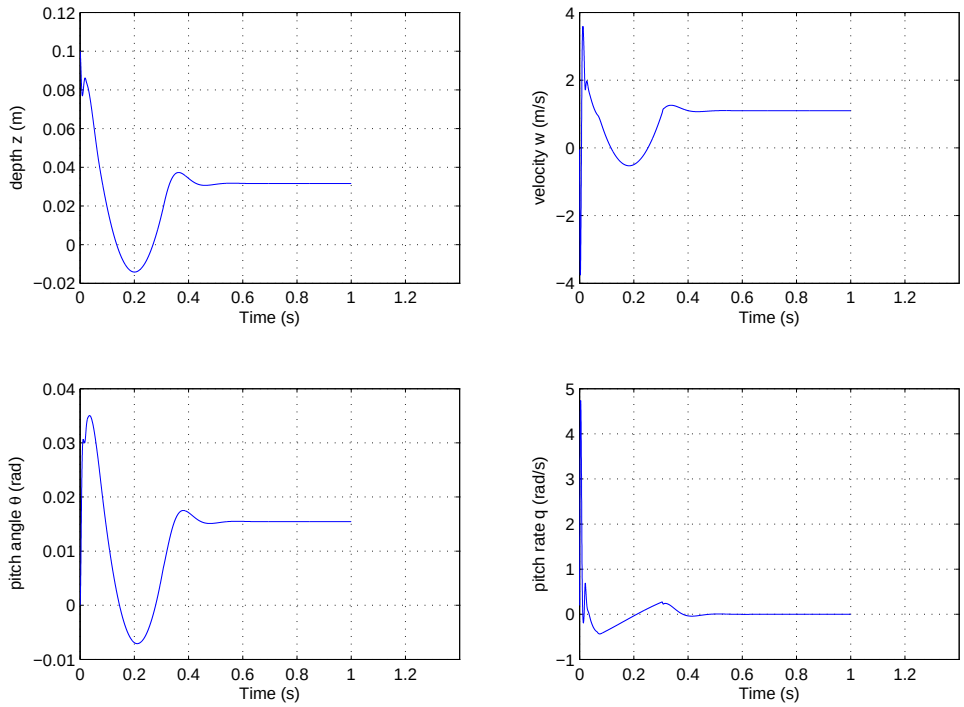

Figure 2.12: Results obtained with cylindrical planing force formulation and double linear feedback in the presence of downwash effects.

2.4.1 Cavity Shift Effect

The difference in system behavior is not only due to the change in nominal cavity radius. With this cavity formulation, the cavity shape is not constant as in previous studies [8, 29, 30]. The effect of the cavity shift can be noted with a stabilized system. By using the previous run parameters, the system can be stabilized, as shown in Figure 2.12, by doubling the values of the control law coefficients given in Eqs. 2.6. However, even with this control, if the cavity shift effect is removed, the system can again be seen to exhibit oscillations.

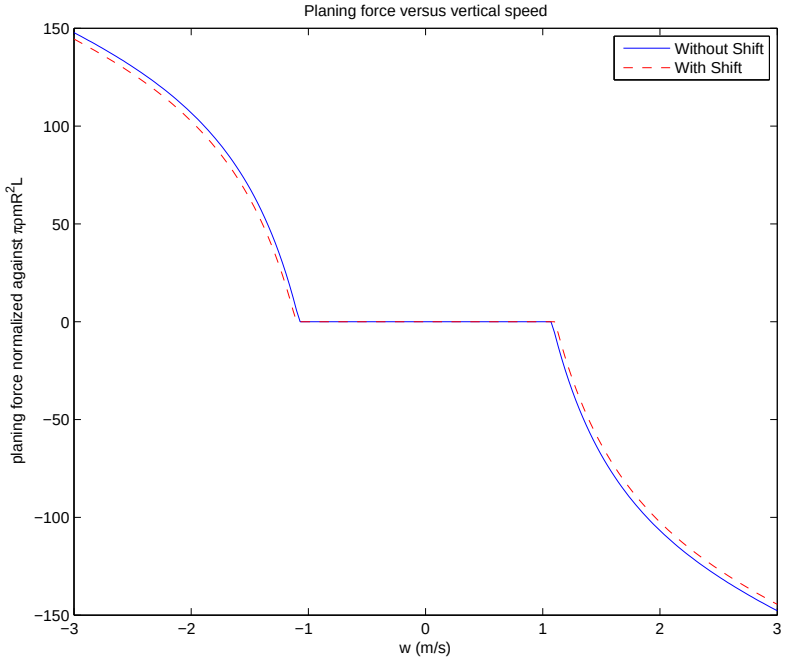

Figure 2.13: Normalized planing force versus vertical speed w, with cavitator actuation neglected, for cylindrical planing force model.

The cavity shift is dependent on the angle of attack of the cavitator with respect to the flow. The cavitator angle of attack is in part due to the vehicle orientation (with respect to the flow). As the vehicle beings to plane, the contribution of the vehicle orientation on the cavitator angle of attack will tend to shift the cavity away from the body. A representation of the normalized planing force versus vertical speed w is shown in Figure 2.13. Here, the planing forces with and without the shift effect are shown. The cavitator actuation angle is fixed at $\delta_c = 0$ to remove contributions due to the actuation angle. As shown, the cavity shift due to body orientation, can be considered as creating a slightly larger cavity radius, which in some cases, may delay the onset of oscillations.

Chapter 3

Vehicle Dynamics with Shifted Non-Cylindrical Cavities

Since the cavity model produces an entire cavity shape, the planing force can be calculated on the basis of the entire profile rather than on the basis of a cylindrical shape assumption, which is fairly inaccurate in determining the planing area, particularly during high immersion. With a cylindrical cavity shape assumption, the wetted area is generally over-predicted as shown in Figure 3.1. The horizontal line represents the assumed cavity shape, with the cylindrical cavity assumption. The curved line represents the actual cavity shape. The error in cavity radius made by using the cylindrical assumption during vehicle system simulations can be quite high [35].

3.1 Non-cylindrical Cavity Planing

To incorporate the non-cylindrical profile, as shown in Figure 3.2, the cavity can be treated as made up of several short cylindrical sections. During each time step, the entire shifted cavity profile is determined. Areas of interference with the vehicle body are then determined. No planing is assumed to occur along the conical forebody. The planing area is then re-meshed by using linear interpolation between the cavity points to refine the region of planing.

The cavity contraction rate must also be considered for the planing force.

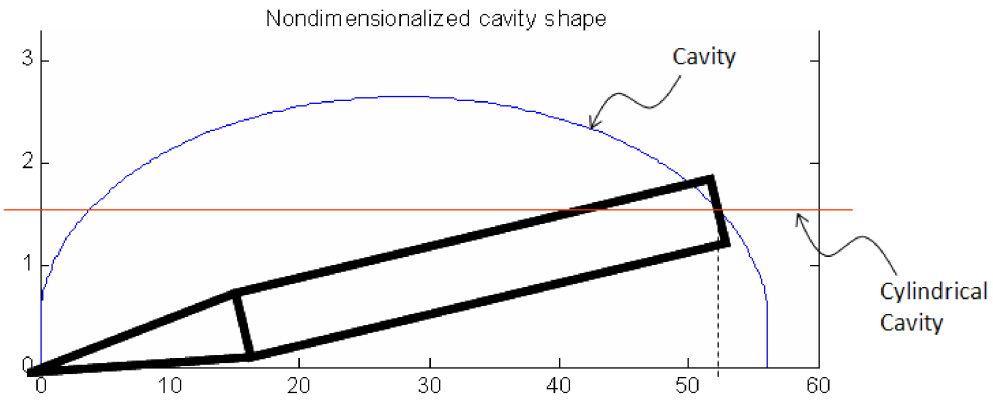

Figure 3.1: Illustration for cylindrical cavity assumption.

In the planing force formulation, only the angle of planing α is used to generate the immersion rate term $\dot{h}$. So for planing forces, the contraction rate can be expressed as an augmentation to α (similar to the role of $\dot{R}_c$ in reference [8]). If independent expansion is assumed, as in the cavity model presented in reference [31], the contraction rate can be determined by the cavity slope and velocity. In the formulation for non-cylindrical planing, the cavity slope and the body slope along each integration section are used to calculate an effective α (see Eq. (3.1)), which generates an appropriate $\dot{h}$ (for each section) that accounts for both the body immersion rate and the cavity contraction. The planing force is then numerically integrated across all sections of interference.

$$\alpha_{corrected}(x) = \alpha + \tan^{-1}(\delta R(x)/\delta(x)) \tag{3.1}$$

In the cylindrical planing formulation, since the cavity shape is assumed, the cavity shift only affects when the vehicle begins to plane and it does not affect

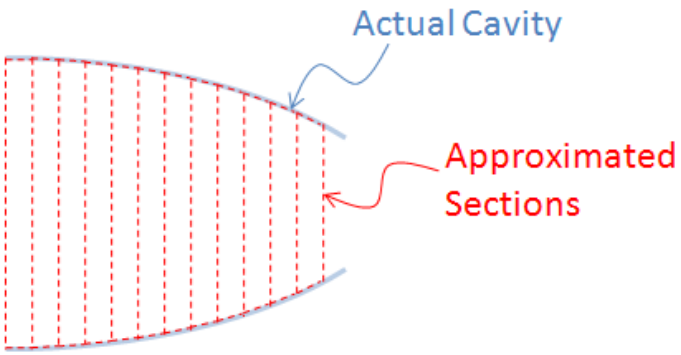

Figure 3.2: Cavity approximated by a series of short cylindrical sections.

the planing force function once planing has been initiated. By contrast, in the non-cylindrical planing force formulation, the shift not only affects when the vehicle begins to plane, but it also changes the profile of the cavity and therefore the planing force function once planing has been initiated. A depiction of the planing force dependence is shown in Figure 3.3. The control as well as the states (which determine body orientation), determine the cavitator angle of attack. This in turn determines the shift and the cavity profile. The profile as well as the body orientation are used in determining whether the body is in contact with the cavity or not. If there is contact, the profile and the body orientation are utilized to integrate the planing force. In previous research [29], wherein cavity shift effects were not considered, the vehicle dynamics could be modeled by using a switching system, with a set of equations governing the system when planing occurs and another set of equations when planing does not occur. In these cases, there are defined state dependent switching boundaries and defined switched dynamics. However, when one considers the cavity shift as well as the non-cylindrical planing, the system has both a state

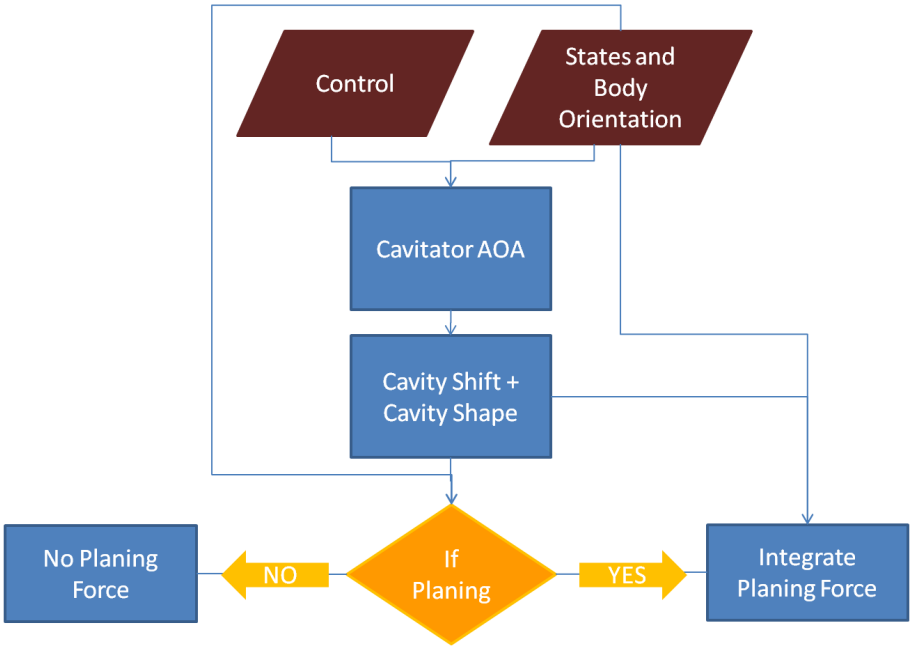

Figure 3.3: Planing force variation for the non-cylindrical planing force model.

and control dependent switching boundary, as well as a state and control dependent switched dynamics.

The planing force function is represented in Figure 3.4. Here, the planing force variation is shown with respect to the vertical speed of the body w, as well as the cavitator actuation angle δ_c. Cavity shift effects are incorporated, the cavity shift being a function of both the body orientation (which for a constant forward speed becomes solely a function of w), and the cavitator actuation angle. The onset of planing in relation to w changes with respect to the actuation angle. Once planing is initiated, the planing force can also be seen to vary with respect to the actuation angle.

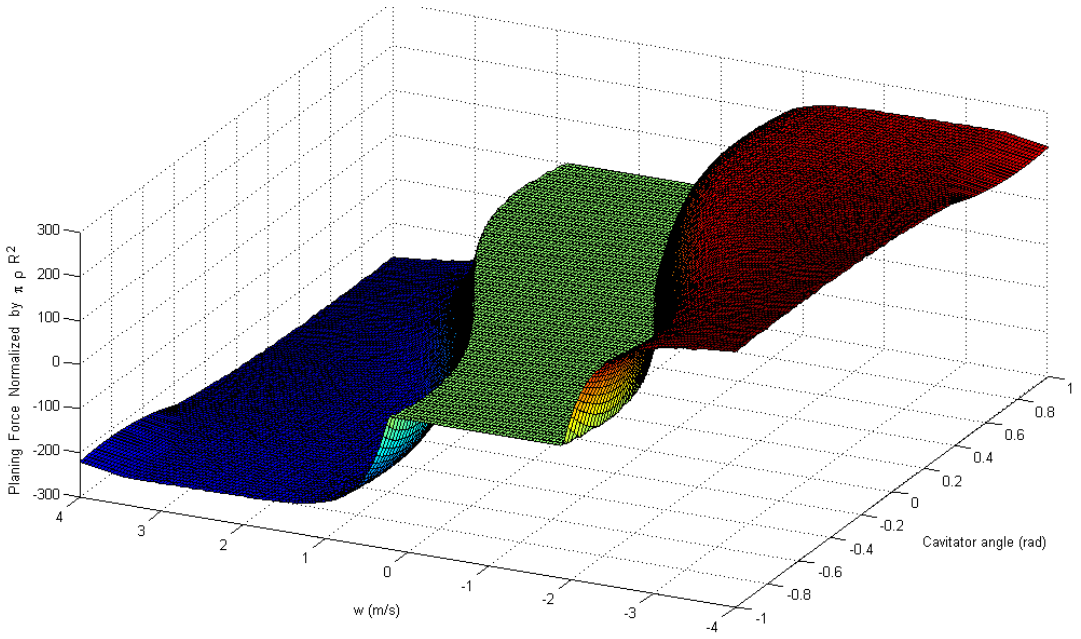

Figure 3.4: Normalized planing force versus vertical speed w, and cavitator actuation angle δ_c, for non-cylindrical planing force model.

3.2 Non-cylindrical Cavity Simulation Results

Results, which were obtained by using the same vehicle parameters as before and the feedback control law given by Eqs. (2.6), are presented in Figure 3.5. Oscillations about a single planing surface are observed. In prior research with cylindrical cavity models [29], it was found that when the cavitation number is lowered from $\sigma = 0.0335$ to $\sigma = 0.025$ (increased speed and larger cavities), the system can demonstrate stable equilibrium solutions. A similar remark can be made about the non-cylindrical planing force case. Results obtained for $\sigma = 0.025$ are shown in Figure 3.6. Here, the system appears to stabilize to an equilibrium solution. Additionally, when the cavitation number is increased from $\sigma = 0.0335$

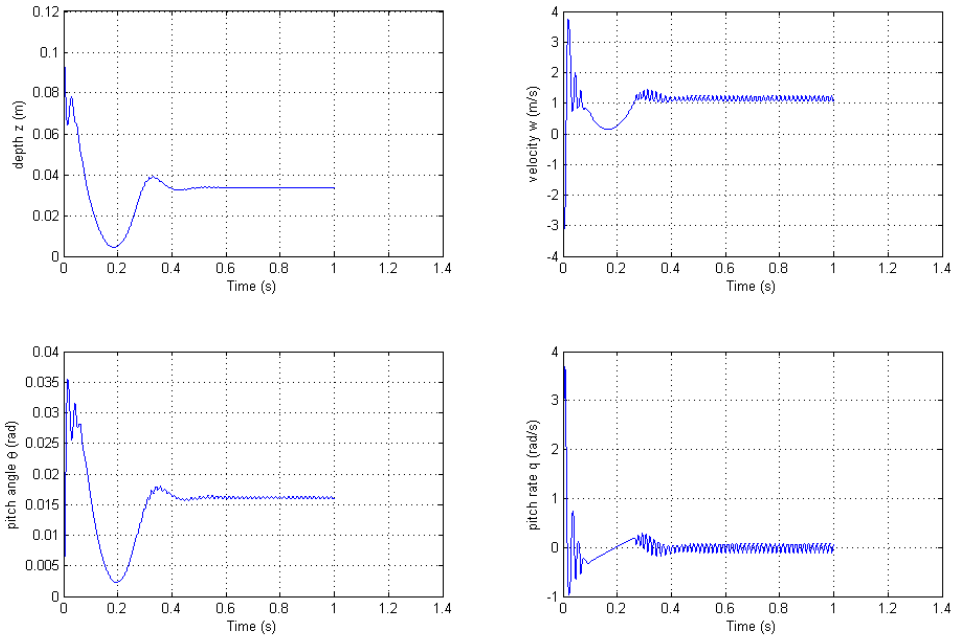

Figure 3.5: System response results obtained with non-cylindrical planing force formulation and linear feedback. Cavitation number is $\sigma = 0.0335$.

to $\sigma = 0.037$ (decreased speed and smaller cavities), the vehicle is seen to exhibit two-sided tailslap motions, as shown in Figure 3.7.

In prior efforts in the group, a Hopf bifurcation of an equilibrium solution and a period-doubling bifurcation were identified [29]. In order to determine whether these bifurcations also occur in the system with non-cylindrical and non-symmetrical cavities, an attempt was made to numerically determine the equilibrium solutions. However, even for cases, where the time domain results suggest the presence of a stable equilibrium solution, these equilibrium solutions could not be found. This is suspected to be due to the discretization of the sections used for the numerical integration along the cavity profile.

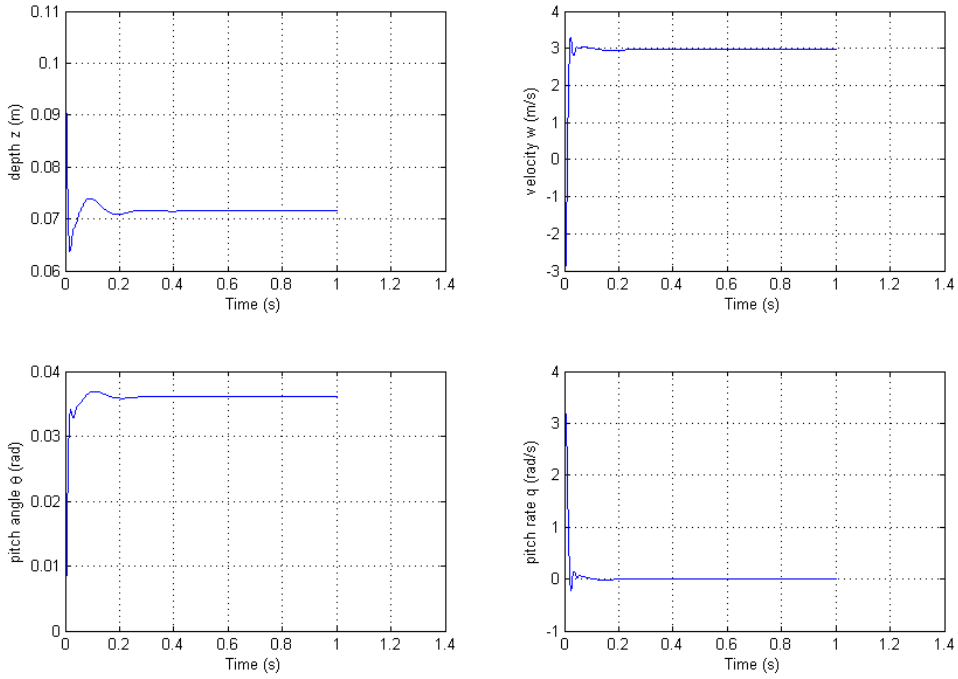

Figure 3.6: System response results obtained with non-cylindrical planing force formulation and linear feedback. Cavitation number is $\sigma = 0.025$.

3.3 Smoothened Non-Cylindrical Cavities and Equilibrium Points

Even with the re-meshed area of planing, as outlined in the previous section, only a discrete estimate of the planing area (and subsequent planing force) is obtained. To improve this computation, a smoothened version of the cavity can be formed by carrying out a cubic spline interpolation of the cavity coordinates generated by the numerical cavity model. This creates a third-order piecewise polynomial representation of the cavity profile. With a continuous expression for the entire cavity, when the body is immersed, the planing area and planing force can be expressed as smooth functions. It should be noted that unlike the smoothing used in reference

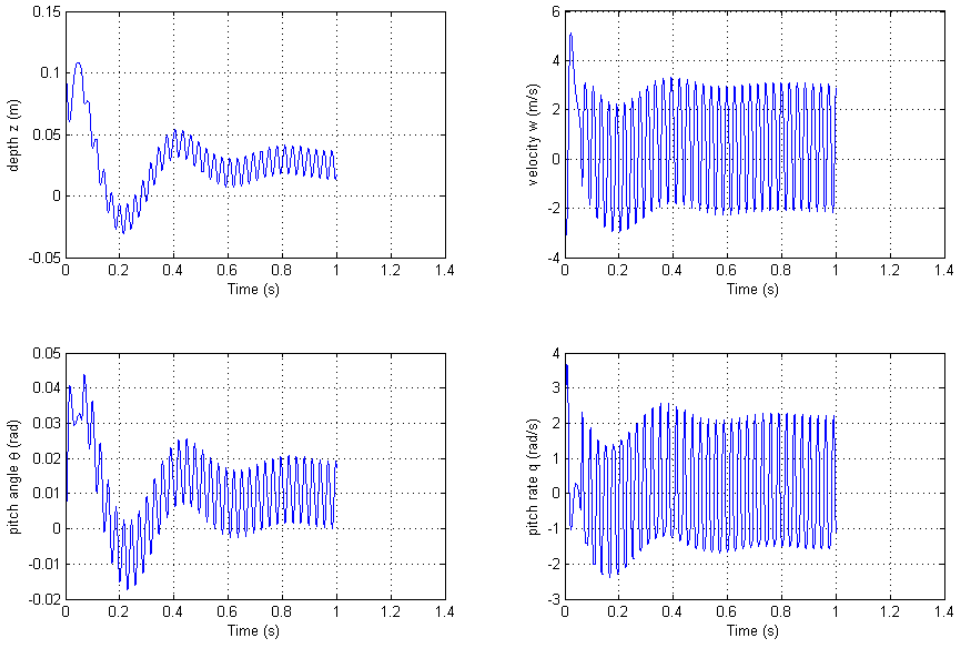

Figure 3.7: System response results obtained with non-cylindrical planing force formulation and linear feedback. Cavitation number is $\sigma = 0.037$.

[28], here, the transition to planing is still non-smooth. Planing forces determined with the smoothened cavity model and the discrete section model are compared in Figure 3.8, for zero cavitator actuation angle; that is, $\delta_c = 0$. There are no discernible differences, with the remark that the chattering type behavior is eliminated with the splined cavity approximation. Similar results were also obtained for other cavitator actuation angles. The time domain results obtained with the splined cavity are also matched with those obtained earlier for the discrete cavity sections.

The main advantage of using a splined cavity profile is that equilibrium solutions can be obtained. A branch of equilibrium points related to stable operations is shown in Figure 3.9. In this figure, the stars represent stable equilibrium points and

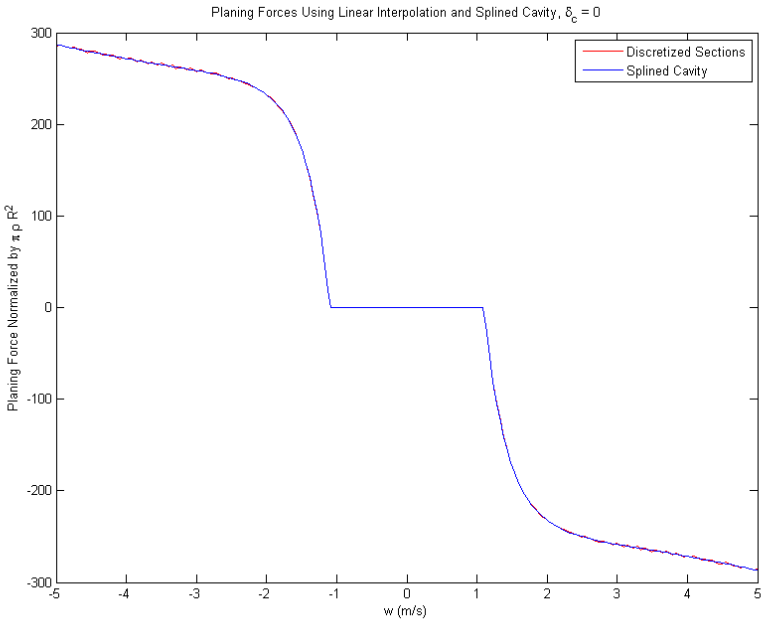

Figure 3.8: Normalized planing force versus vertical speed, w, for both the re-meshed discrete sections and splined cavity shapes, when $\delta_c = 0$.

the circles represent unstable equilibrium points. It can be seen that at a cavitation number between 0.0313 and 0.0315, there is a transition from a stable state to an unstable state on this branch of equilibrium points. Here the equilibrium solutions are plotted as the l^2 norms of the corresponding states. Thus, each solution can be represented as a scalar value, which corresponds to the magnitude of an equilibrium solution; this is done for easier visualization.

Through the time domain results, stable equilibrium and stable limit-cycle behavior are identified. In Figure 3.10, a graph of the projection of the steady-state behavior of the system is shown on the w - q plane with respect to the cavitation number. As expected, the transition from stable to unstable equilibrium points

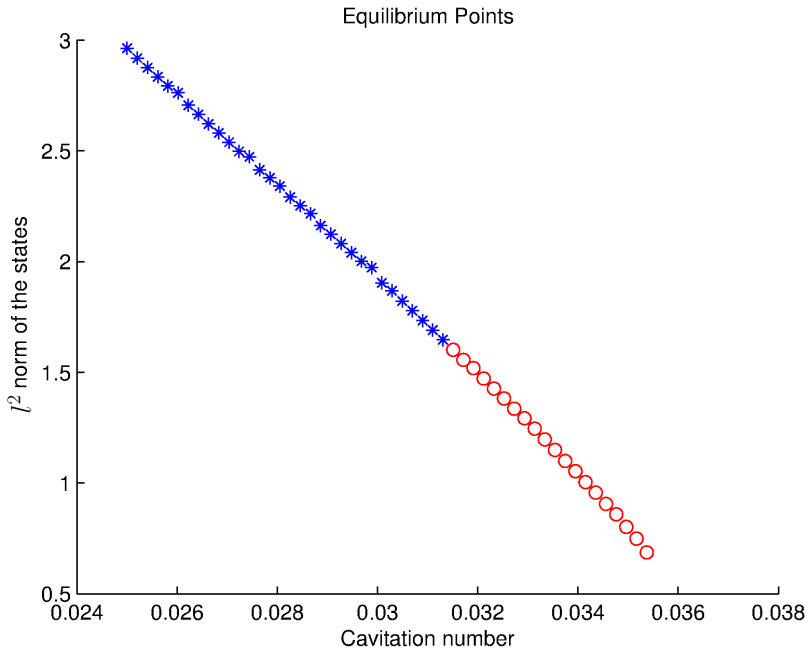

Figure 3.9: l^2 norm of the equilibrium points versus cavitation number.

corresponds to the onset of limit-cycle behavior and therefore suggesting a Hopf bifurcation. By numerically evaluating the eigenvalues of the linearized system about the equilibrium points, the system is seen to satisfy the transversality condition required for a Hopf bifurcation. This finding parallels the Hopf bifurcation found in the prior work with a cylindrical cavity formulation [28, 29]. However, the instability occurs at a different cavitation number in the present case. As the cavitation number is further increased, an abrupt change in the character of the steady-state limit cycles is observed, as shown in Figure 3.11. At a cavitation number between 0.036 and 0.03625, the steady-state limit-cycle motion grows dramatically. From the time domain responses of the vehicle, it is found that this abrupt change corresponds to the case when the limit cycles first begin to plane about both surfaces at steady

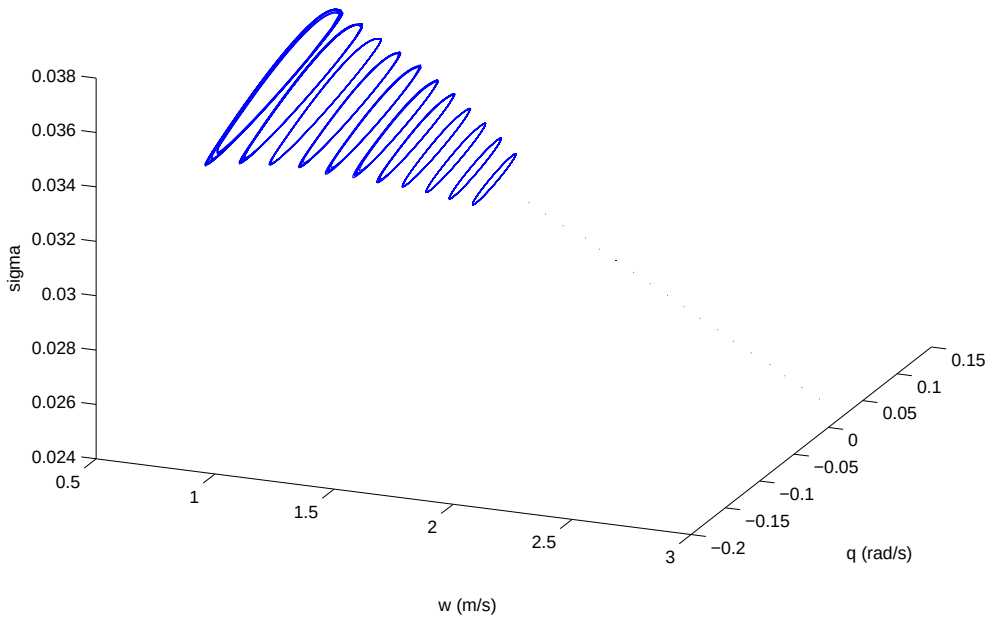

Figure 3.10: Projection of steady-state behavior of system in the w-q plane versus cavitation number σ.

state. It is believed that this additional impact with the second cavity surface is related to the post-Hopf bifurcation behavior discussed in reference [29].

3.3.1 System Dynamics With Washout Filter

In the previous work reported in reference [29], a washout filter was used to delay the onset of the Hopf bifurcation. This approach is desirable since it preserves the equilibrium solutions of the original system. The washout filter generates an additional state variable p whose dynamics are described by Eq. 3.2, where $d > 0$ is a constant between 0 and 1, k_p is the dynamic feedback coefficient, and q is the

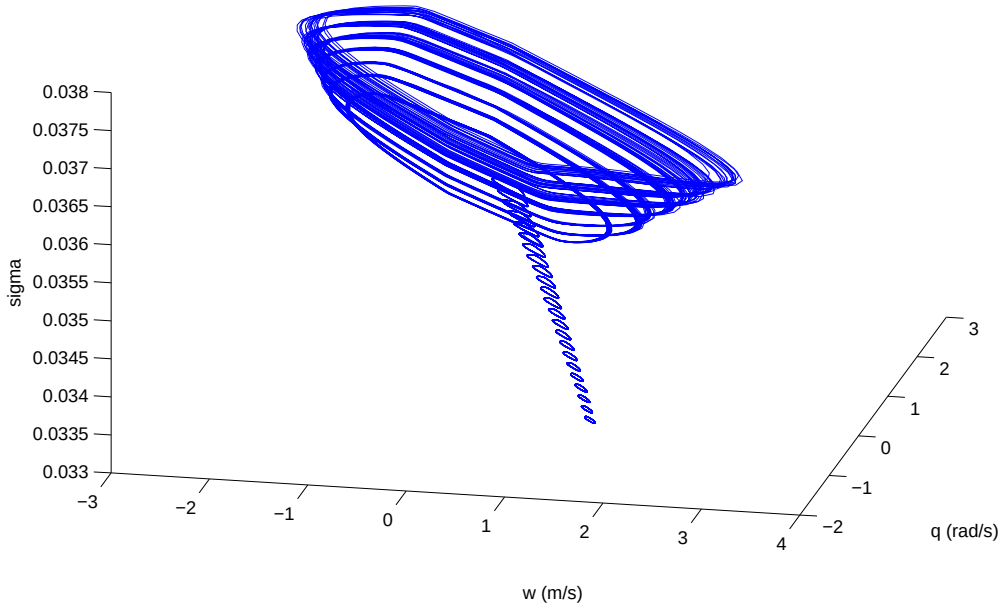

Figure 3.11: Projection of steady-state behavior of system in the w-q plane versus cavitation number σ, showing two-sided tailslap behavior.

pitch rate. The original feedback law given by Eqs. (2.6) is then augmented by adding δ_{c2}, as given in Eq. (3.3).

$$\dot{p} = q - dp \tag{3.2}$$

$$\delta_{c2} = k_p(q - dp) \tag{3.3}$$

For an equilibrium solution $q - dp = 0$ and the system simplifies back to the original system without the filter. Equilibrium solutions obtained for $d = 0.5$ and $k_p = -3$, are shown in Figure 3.12. These equilibrium solutions are the same as those obtained in the original system and shown in Figure 3.9, but here, these equilibrium

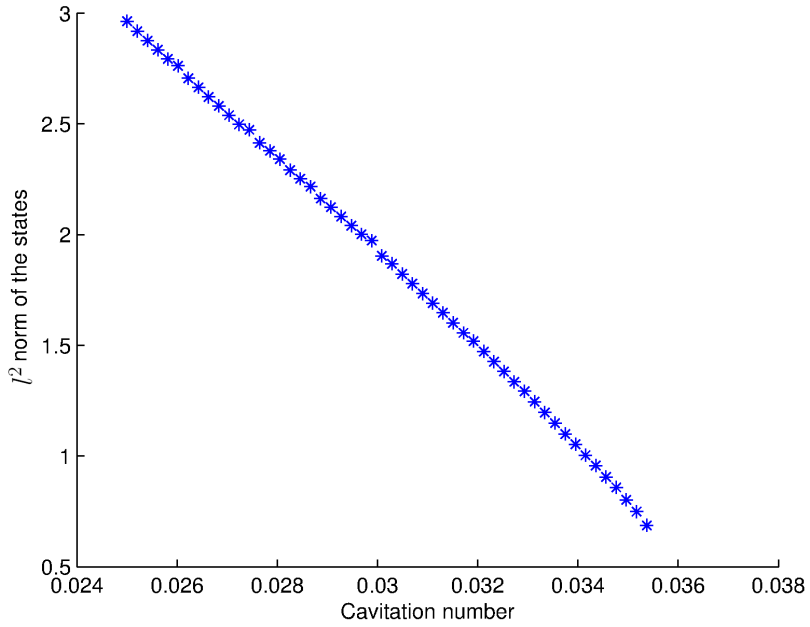

Figure 3.12: l^2 norm of the equilibrium points versus cavitation number with washout filter.

points remain stable and there are no limit-cycle motions within the considered range of the cavitation number. A time domain response of the system with the washout filter obtained at $\sigma = 0.034$ is shown in Figure 3.13. The steady state here corresponds to a stable equilibrium position, while in the original system, this cavitation number is associated with limit-cycle motions in the post-Hopf bifurcation regime.

3.3.2 Fin Input Based Stabilization Inside Cavity

Stabilization inside the cavity may also be beneficial for straight line flight. Since there are no planing forces while the vehicle is completely inside the cavity,

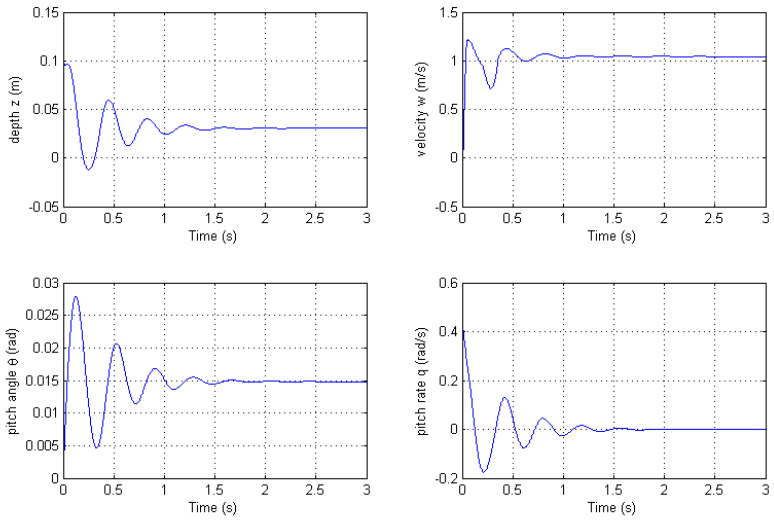

Figure 3.13: Results obtained with non-cylindrical planing force formulation and washout filter. Cavitation number is $\sigma = 0.034$.

the fins need to be utilized to stabilize the rear of the vehicle. Through the previous simulations, it can be seen that a fin deflection of $\delta_e = 0$ is not enough to support the rear of vehicle. Instead, a passive fin deflection of $\delta_e = 0.1$ is utilized along with the cavitator control input described by Eqs. 2.6. The fin deflection angle was chosen by determining the fin force, under static conditions, that is required to support the rear of the vehicle. The vehicle system is found to have stable equilibrium solutions inside the cavity. The equilibrium points are plotted in Figure 3.14. Stable equilibrium points exist past the region where Hopf bifurcation occurs in the original system.

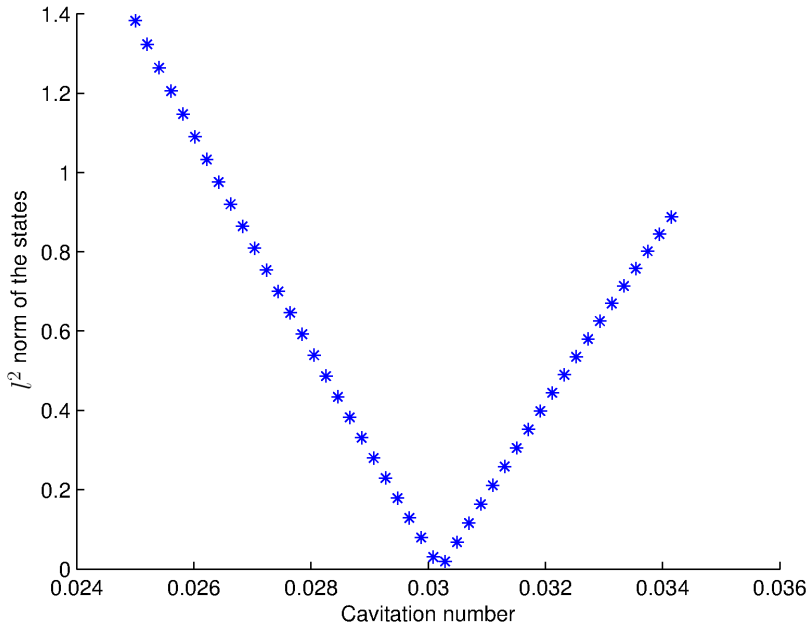

Figure 3.14: l^2 norm of the equilibrium points versus cavitation number by using linear feedback and constant fin input.

3.4 Logvinovich Cavity and Related Dynamics

A similar analysis was also performed by using a second cavity model. A semi-empirical closed-form solution for cavity shape is presented in reference [31]. A diagram of the cavity is shown in Figure 3.15. For this representation, the cavity radius is expressed as in Eq. (3.4). Here, L_k and R_k occur at the maximum radius of the cavity. The terms x_1 and R_1 refer to an arbitrary point along the cavity, and χ is a correction factor. The cavity contour is defined as passing through the point where $R = R_1$ at time $t = 0$. An additional derived relationship between R_k and R_n is shown in Eq. (3.5). In this expression, $c_{x0} = 0.82$ and the constant k is approximately unity (for the cavitations numbers of interest); both of these values

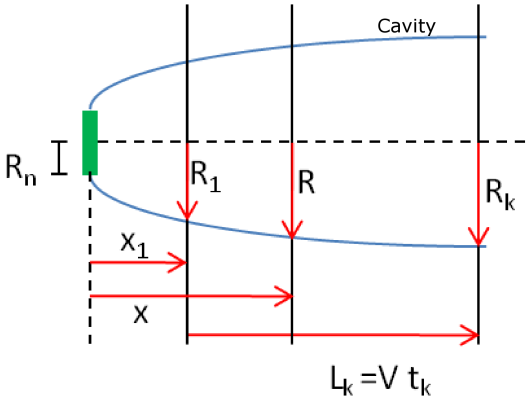

Figure 3.15: Diagram for the Logvinovich Cavity Model

can be determined experimentally. Additionally, if x_1 is chosen as $x_1 = 2R_n$, R_1 can be expressed as in Eq. (3.6). Furthermore from Figure 3.15, $t_k = L_k/V$, and t can be expressed in terms of the distance x as $t = (x - x_1)/V$. The term L_k can in turn also be approximated by using an experimentally derived relationship as in Eq. (3.7).

$$R = R_k\sqrt{1 - \left(1 - \frac{R_1^2}{R_k^2}\right)\left|1 - \frac{t}{t_k}\right|^{2/\chi}} \tag{3.4}$$

$$\left(\frac{R_k}{R_n}\right)^2 = \frac{c_{x0}(1+\sigma)}{k\sigma} \tag{3.5}$$

$$R_1 = 1.92R_n \tag{3.6}$$

$$L_k = R_n\left(\frac{1.92}{\sigma} - 3\right) \tag{3.7}$$

With a correction factor of $\chi = 0.85$ (chosen to match experimental data), the expression for cavity radius can be written as Eq. (A.14), where the d terms represent the associated diameters.

$$d_{max} = d_c\sqrt{0.82(1+\sigma)/\sigma}$$

$$l_m = d_c/2(1.92/\sigma - 3)$$

$$k_1 = 1.92(.82(1+\sigma)/\sigma)^{-\frac{1}{2}}$$

$$k_2 = (x \cdot d_c - d_c)/l_m$$

$$R_c(x) = d_{max}/2\sqrt{1-(1-k_1^2)|1-k_2|^{2/.85}} \tag{3.8}$$

A comparison of cavity models is presented in Figure 3.16. Here, three cavity models are presented, the Logvinovich model described in this section, the numeric cavity model, and the Dzielski cavity representation presented in reference [8] (only used for approximating of cavity radius at the rear of the vehicle). For the vehicle length considered in this work ($L = 1.8$m), the Logvinovich and numeric cavity models produce similar results at the tail end of the vehicle.

The Logvinovich cavity formulation was implemented into the non-cylindrical planing models by sampling points along the cavity length. The simulations provided qualitatively similar results as those obtained with the numeric cavity model. The system exhibits stable equilibrium behavior at low cavitation numbers (high-speed) and transitions into limit-cycle motion as the cavitation number increases and the cavities tighten. A diagram of the equilibrium solutions is presented in Figure 3.17. The system is also similarly stabilized by using a washout filter or fin input. A full write-up on the simulation results using the Logvinovich cavity is presented in reference [34].

The main advantage of the Logvinovich cavity representation is that it is a

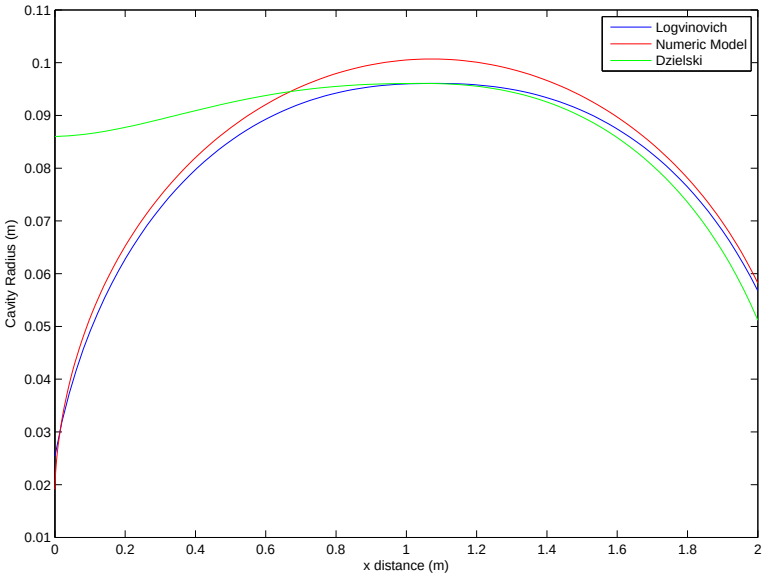

Figure 3.16: Cavity model comparison for $\sigma = 0.0335$.

closed-form solution, and cavity shapes can be easily and rapidly calculated. This aspect is not as important for constant speed simulations (as presented in the previous sections), but becomes important for variable speed maneuvering which will be presented in a subsequent chapter.

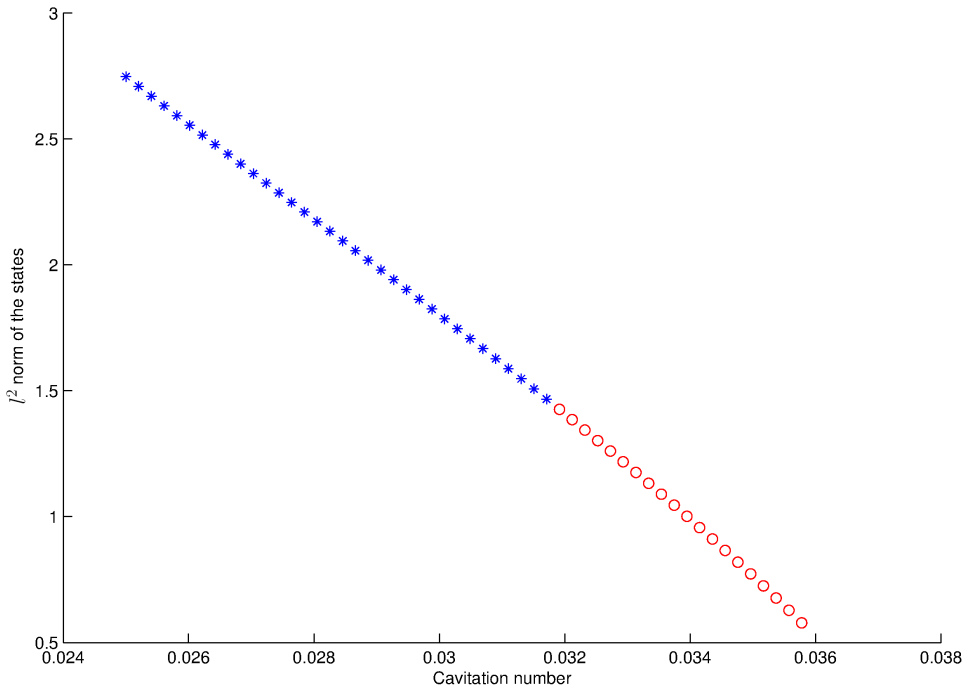

Figure 3.17: l^2 norm of the equilibrium points versus cavitation number by using the Logvinovich cavity formulation.

Chapter 4

Extensions to Vehicle Dynamics Models and Related Dynamics

In this chapter, some additional model considerations are presented for the supercavitating vehicle system. The modifications and the physical basis behind the modifications are discussed, along with an examination of the resulting dynamics.

4.1 Partial Cavitation

Being able to model dynamics for partially cavitating vehicles is an important step towards being capable of modeling full vehicle missions. Partial cavitation occurs when operating at speeds where the cavitation bubble does not entirely envelop the vehicle, as illustrated in Figure 4.1. When operating in these ranges, a portion of the vehicle (from the rear forward) is fully wetted. Along the wetted portions, the vehicle experiences buoyancy forces, and added mass effects (caused by accelerating the body in the fluid). The planing no longer occurs at the rear, but occurs where the cavity is formed.

For the partial cavitation case, a more general forebody is considered, as shown in Figure 4.2. A truncated cone with an initial radius of R_1 is considered. This modification was made because the numeric cavity models used to predict body-in-flow partial cavities were made with these truncated cone forebodies.

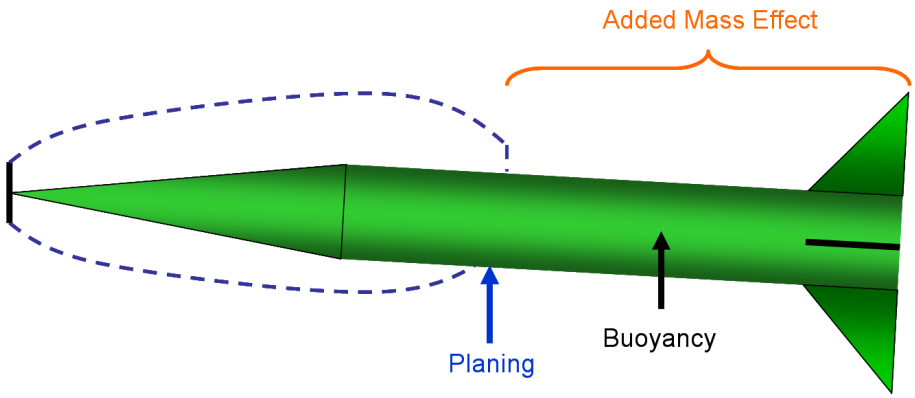

Figure 4.1: Diagram of a partially cavitating vehicle.

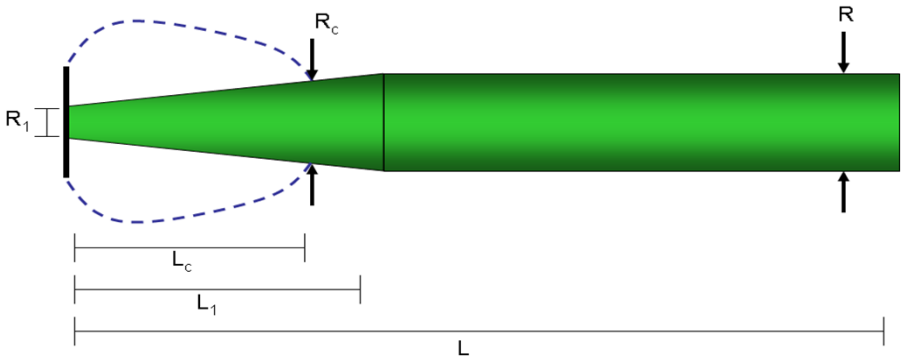

Figure 4.2: Vehicle and cavity length parameters.

4.1.1 Buoyancy and Added Mass Effects

If the dimensions are as shown in Figure 4.2, the buoyancy force can be determined as shown in Eq. (4.1), where $r_c = \frac{R-r_1}{L_1} L_c + r_1$. The resulting buoyancy moments can be expressed as given in Eqs. (4.2)-(4.4).

$$F_{buoy} = \begin{cases} \rho g \pi R^2 (L - L_c) & \text{if } L_c \geq L_1 \\ \rho g \pi \left(R^2 (L - L_1) + \frac{1}{3}(L_1 - L_c) \frac{R^3 - r_c^3}{R - r_c} \right) & \text{otherwise} \end{cases} \tag{4.1}$$

$$F_{buoy} = \begin{cases} M_{buoy1} & \text{if } L_c \geq L_1 \\ M_{buoy2} & \text{otherwise} \end{cases} \tag{4.2}$$

$$M_{buoy1} = \frac{1}{2}\rho g\pi R^2(L^2 - L_c^2) \tag{4.3}$$

$$M_{buoy2} = \rho g\pi\Big[\frac{1}{4}\frac{(R-r_1)^2(L_1^4 - L_c^4)}{L_1^2} + \frac{2}{3}\frac{r_1(R-r_1)(L_1^3 - L_c^3)}{L1} + \frac{1}{2}r_1^2(-L_c^2 + L_1^2) + \frac{1}{2}R^2(L^2 - L_1^2)\Big] \tag{4.4}$$

The added mass terms are approximated as the added mass of a 2-D cylinder moving through fluid. A similar approach has been presented in reference [31]. The obtained force and moments due to the added mass effects are shown in Eqs. (4.5)-(4.6). The added mass terms are defined according to Eqs. (4.7)-(4.9), and the force and moment conventions remain the same as with the previous systems with the reference being the nose of the vehicle.

$$F_{am} = \lambda_{22}\dot{w} + \lambda_{26}\dot{q} \tag{4.5}$$

$$M_{am} = \lambda_{26}\dot{w} + \lambda_{66}\dot{q} \tag{4.6}$$

$$\lambda_{22} = \int \pi\rho R^2 dx$$

$$= \begin{cases} \rho\pi R^2(L - Lc) & \text{if } L_c \geq L_1 \\ \rho\pi(R^2(L - L_1) + \frac{1}{3}(L_1 - L_c)\frac{R^3 - Rc^3}{R - Rc}) & \text{otherwise} \end{cases} \tag{4.7}$$

$$\lambda_{26} = \int x\pi\rho R^2 dx$$

$$= \begin{cases} \frac{1}{2}\rho\pi R^2(L^2 - L_c^2) & \text{if } L_c \geq L_1 \\ \rho[\frac{1}{4}\frac{\pi(R-r_1)^2(L_1^4-L_c^4)}{L_1^2} + \frac{2}{3}\frac{\pi r_1(R-r_1)(L_1^3-L_c^3)}{L_1} & \text{otherwise} \\ \quad +\frac{1}{2}\pi r_1^2(L_1^2 - L_c^2) + \frac{1}{2}\pi R^2(L^2 - L_1^2)] & \end{cases} \tag{4.8}$$

$$\lambda_{66} = \int x^2 \pi\rho R^2 dx$$

$$= \begin{cases} \frac{1}{3}\pi\rho R^2(L^3 - L_c^3) & \text{if } L_c \geq L_1 \\ \rho[\frac{1}{5}\frac{\pi(R-r_1)^2(L_1^5-Lc^5)}{L_1^2} + \frac{1}{2}\frac{\pi r_1(R-r_1)(L_1^4-L_c^4)}{L_1} & \text{otherwise} \\ \quad +\frac{1}{3}\pi r_1^2(L_1^3 - L_c^3) + \frac{1}{3}\pi R^2(L^3 - L_1^3)] & \end{cases} \tag{4.9}$$

4.1.2 Cavity Model

For partial cavitation, the cavity prediction model must now account for the vehicle body which is now within the flow. Here, a partial cavitating numeric cavity model provided in reference [44] is utilized. This numeric model can be used to solve for the steady-state cavities that close along a body for an axi-symmetric flow, as shown in Figure 4.3.

The cavity model is an iterative potential flow solver similar to the supercavitating numeric cavity model. Cavity shift effects due to cavitator angle of attack are again approximated by using the method shown in the previous chapter. A limitation of this model is that it is only able to converge for small cavities (high cavitation numbers). So only cavities that close on the front portions of the body can be considered in this fashion. As shown in Figure 4.1, planing occurs along the length of the cavity, and where the vehicle is wetted, added mass and buoyancy

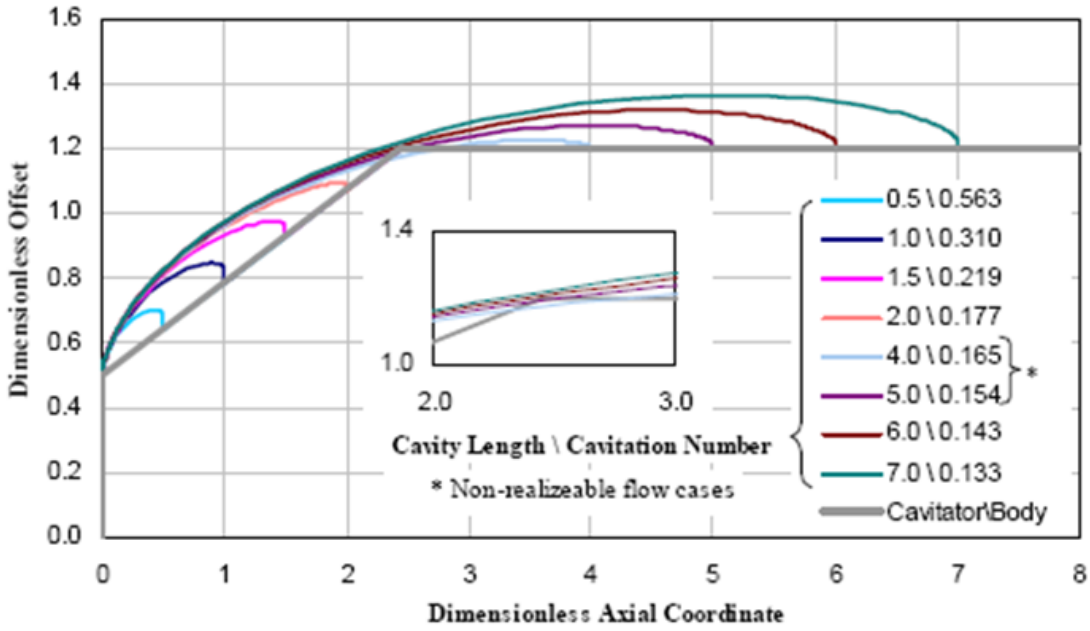

Figure 4.3: System response results from numeric partial cavity model presented in reference [44].

forces are introduced into the system dynamics.

4.1.3 Simulation Results

The partially cavitating vehicle system was run by using the same simulation parameters as used in the previous studies, with $g = 9.81\ m/s^2$, $m = 2\ kg$, $R_n = 0.0191\ m$, $R = 0.0508\ m$, $L = 1.8\ m$, $n = 0.5$, and $C_{x0} = 0.82$. Working near the largest cavity limit of the partial cavity model (for the given vehicle and cavitator parameters), a cavitation number of $\sigma = 0.066925$ is considered. This generates a cavity of approximately $0.7640\ m$. The liner feedback configuration used in the supercavitating systems is again utilized here (Eqs. (2.6)). Simulation results are

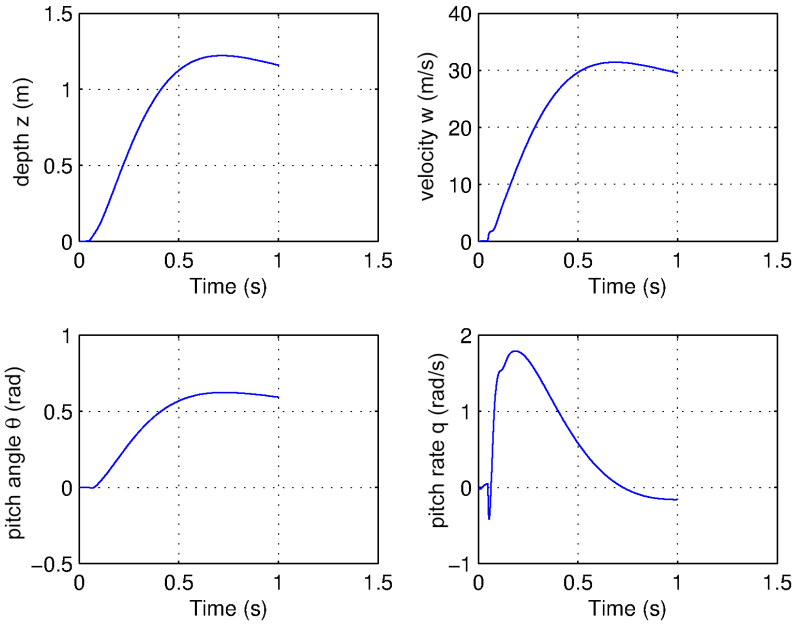

Figure 4.4: Simulation results for partial cavity model with $\sigma = 0.066925$.

presented in Figure 4.4. Since there is no planing along the rear of the vehicle, it is unable to support itself at the rear (by using this particular control), and the rear sinks generating a high pitch angle and a high sideslip angle (as shown by the values for the transverse velocity w).

Since this is the largest cavity that can be converged upon by using the partial cavity numeric model, larger partial cavities are approximated by using the supercavitating numeric model. This approach may not produce an accurate cavity shape since it does not consider the vehicle body in the flow. But, cavities generated using this approach can be used as representative partial cavity shapes to illustrate potential partially cavitating vehicle dynamics. The supercavitating numeric cavity model is run at low speeds (compared to the supercavitating vehicle simulations),

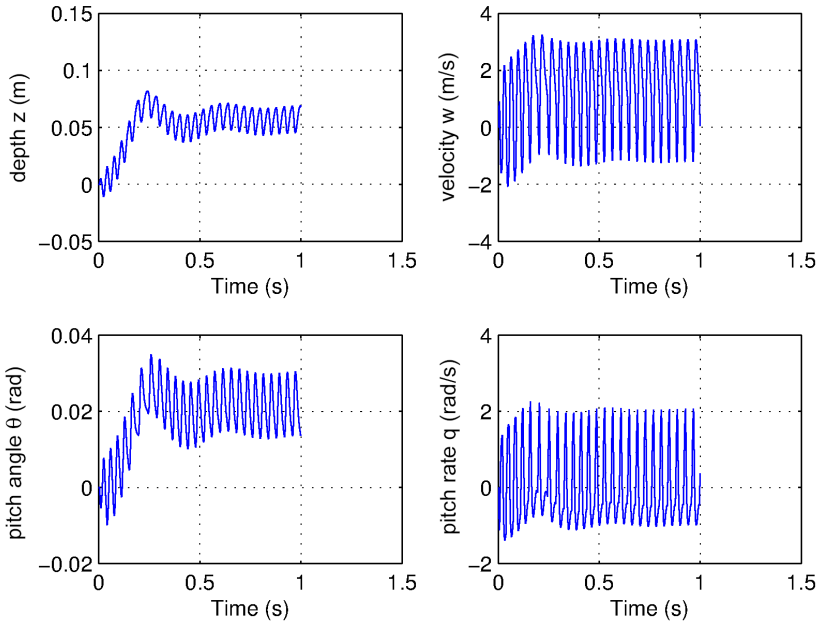

Figure 4.5: Simulation results obtained by using numeric supercavitating model to estimate partial cavity shape at $\sigma = 0.043$.

which will mean the generation of generate small cavities. The small cavities are then truncated to only sections where the cavity radius is larger then the vehicle body. The truncated supercavity, is then treated as an estimate of a partial cavity. Results of a simulation obtained for $\sigma = 0.043$ is shown in Figure 4.5. This corresponds to a cavity length of 1.5106 m (close to the length of the vehicle at $L = 1.8$ m). Here, limit-cycle motion is observed.

By running the simulation with a slightly smaller cavity, at $\sigma = 0.046$, with 1.3930 m of the vehicle unwetted, the rear of the vehicle is again unable to be supported by the planing (see Figure 4.6).

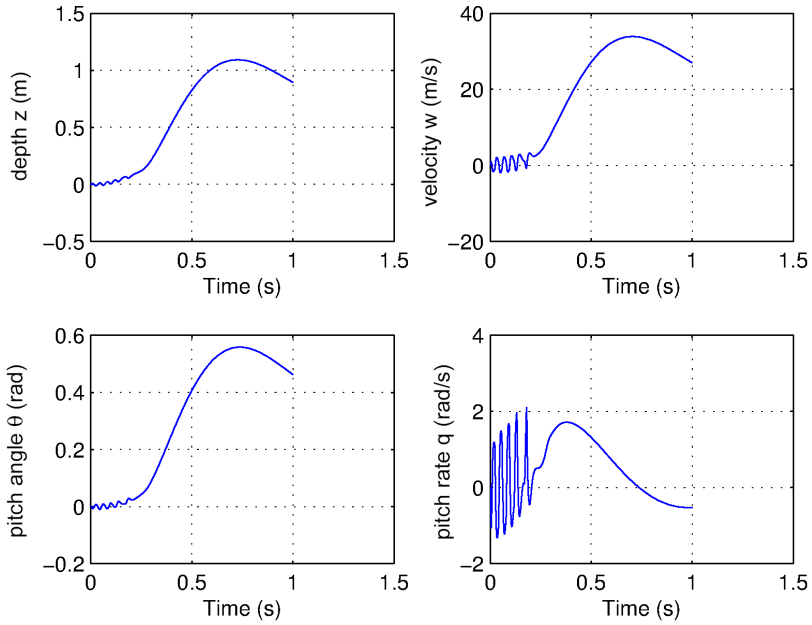

Figure 4.6: Simulation results obtained by using numeric supercavitating model to estimate partial cavity shape at $\sigma = 0.046$.

4.1.4 Fin Feedback

For the partially cavitating vehicles, the planing forces are not rearward enough to support the vehicle. A simulation run with a passive fin input of $\delta_e = 0.1\ rad$, is considered (with the same the linear cavitator feedback control). As mentioned in the previous chapter, this is approximately the fin angle required to statically support the rear of a supercavitating vehicle. The simulation results are presented in Figure 4.7. For the supercavitating system, the vehicle was able to eventually stabilize inside the cavity using this passive fin input (no planing support required). However, for the partially cavitating system, even with the buoyancy forces helping to support the vehicle (as compared to the supercavitating case), the vehicle is still

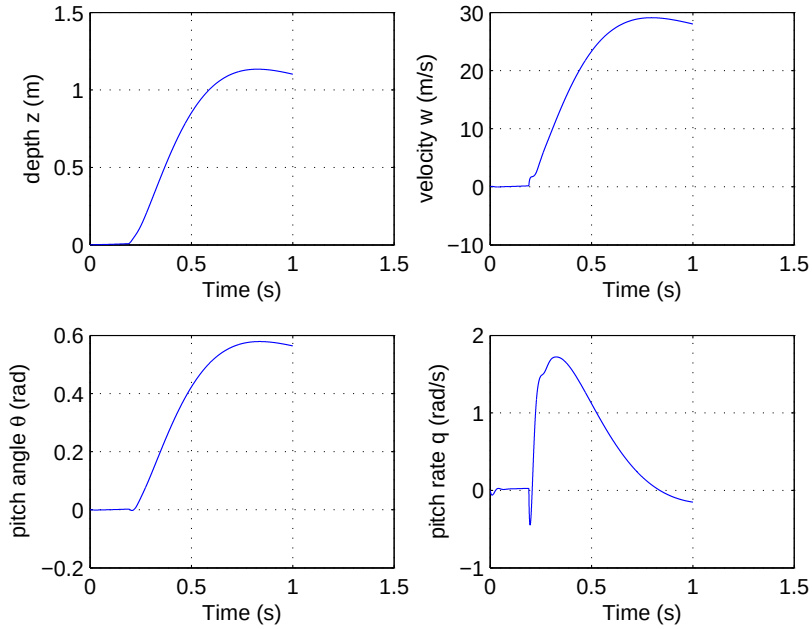

Figure 4.7: Simulation results obtained for the partial cavity model $\sigma = 0.066925$, with passive fin input of $\delta_e = 0.1\ rad$.

unable to support itself. This may be attributed to the fact that for the partially cavitating system, the planing forces and moments are insufficient to resist transient motions, whereas with the supercavitating system, planing is able to reject high pitch rates and vehicle sideslip angles before the vehicle stabilizes inside the cavity.

A modified linear fin feedback in addiition to the linear cavitator feedback is considered next. A simulation conducted using the control actuation given by Eq. (4.10) is shown in Figure 4.8. Similar to the reasoning used for the choice of feedback states in Eqs. (2.6), the fin feedback is based on a practically measurable state (as opposed to vehicle side slip w). Here, the vehicle clearly stabilizes with very small sideslip angle (moving predominantly forward with respect to the vehicle axis).

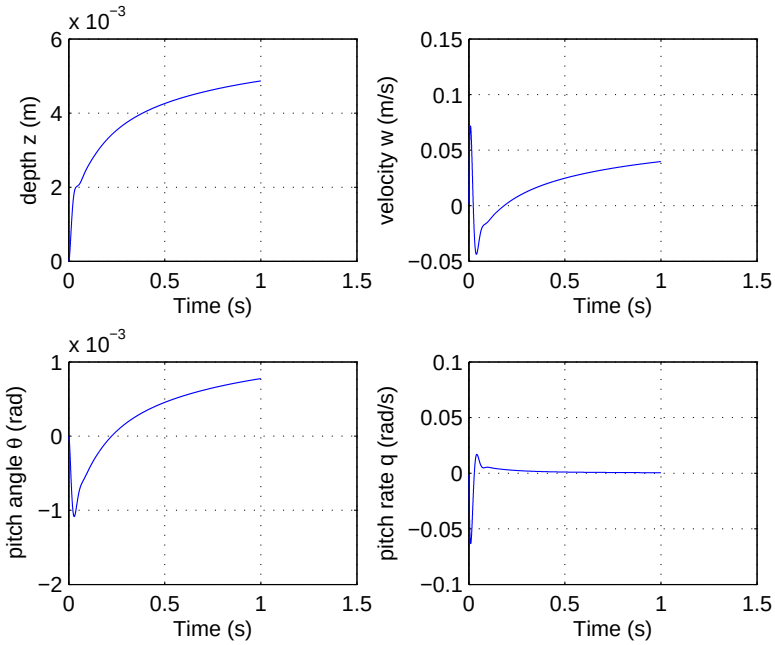

Figure 4.8: Simulation results obtained for the partial cavity model with $\sigma = 0.066925$, using cavitator and fin linear feedback.

$$\begin{aligned} \delta_e &= .12 + .3q \\ \delta_c &= 15z - 30\theta - .3q \end{aligned} \tag{4.10}$$

The Matlab code used for the partially cavitating vehicle dynamics model is included in Appendix B.

4.1.5 Summary

The partial cavitating vehicle dynamics model was generated to explore vehicle motions present during this type of operation. A numeric partial cavity model is used, but this model only provides solutions for limited length cavities. Longer

partial cavities are estimated by using truncated versions of supercavity solutions. Vehicles operating under partially cavitating conditions are modeled here by adding buoyancy forces and simplified added mass expressions. Because the cavity closes further forward on the body, compared to the supercavitating systems, planing does not provide sufficient resistance (for smaller partial cavities) to high vehicle sideslip angles without the aid of feedback fin control. A future goal would be the capability of simulating full vehicle missions, from fully wetted, to cavity growth (partial cavitation), to full supercavitation (and potentially transitioning between the different operating conditions). Unfortunately at the time of this work, there are no unsteady partial cavity models. The work presented here provides an initial step towards modeling full vehicle missions that include cavity growth (and collapse).

4.2 Delayed Cavity with Non-Steady Planing Forces

In much of the previous research (and in all of the aforementioned models), the planing force modeling is based on the assumption that steady planing is neeeded to simplify the planing force calculations. With this assumption, vehicle motions into or out of the cavity are ignored. The simplification pertains to the immersion rate term $\dot{h}$. For steady planing, the immersion rate at any section of planing can be represented as $\dot{h} = V_t \cdot sin(\alpha)$, where α is the angle between the body and the cavity, and V_t in this expression represents the total vehicle speed (Figure 4.9). This immersion rate accounts for the fact that the body is moving along the cavity axis at an angle but does not include any radial motions of the body into the fluid. With

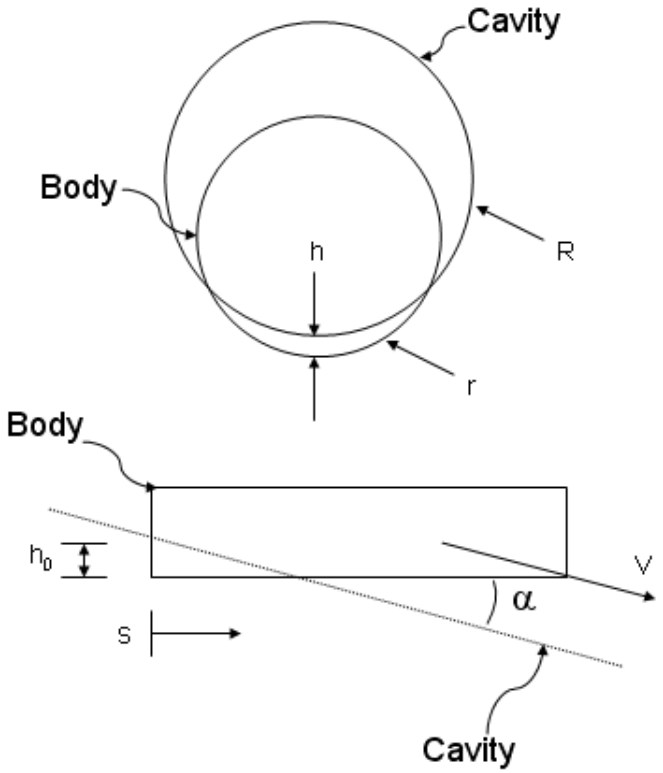

Figure 4.9: Diagram of a cylinder planing on a cylindrical surface.

the steady planing assumption, the planing force becomes only a function of the body's position with respect to the cavity, and therefore it can be considered as having no damping relationship in terms of the vehicle's motion.

As demonstrated in the previous models, cavity shape and location predictions can have a significant effect on the resulting dynamics. Two methods of modeling cavity position and orientation (with respect to the vehicle body) are shown in Figure 4.10. The instantaneous approach is utilized in all of the previous models. With this approach, the cavity position and orientation are calculated based on the current cavitator position and velocity direction. In this approach, one approximates

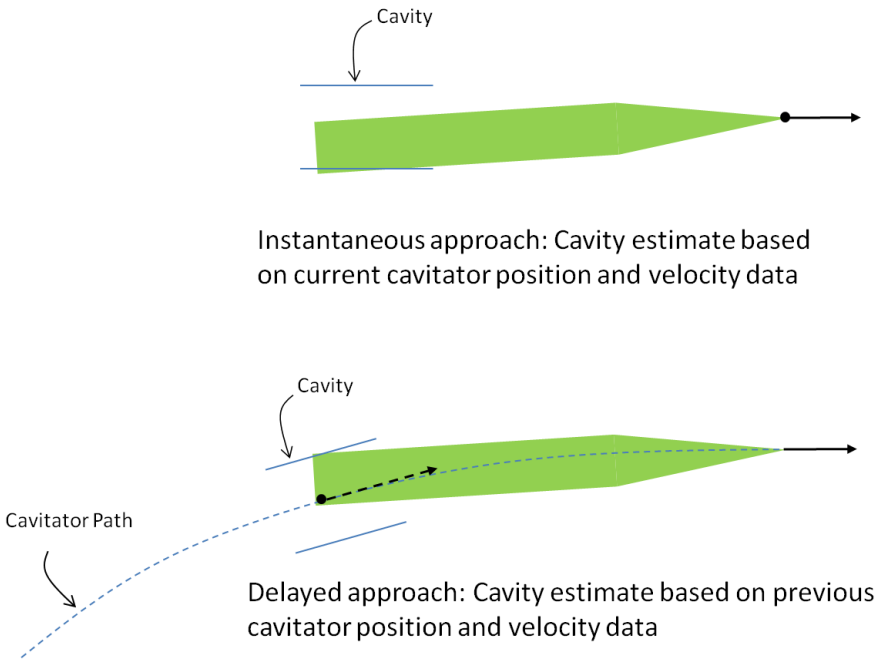

Figure 4.10: Two methods of modeling cavity position and orientation.

the cavity at the rear of the vehicle (where planing occurs) as a cavity that would have been generated if the cavitator had been moving along it's current velocity direction up to it's current position. This approximation works well at capturing the dynamics of the system when the vehicle speeds are high. However, the cavity at the rear of the vehicle is actually generated by previous motions of the cavitator through the fluid (which may not coincide with the current position and orientation of the cavitator). As such, a more appropriate method of representing the cavity for planing is to model the cavity centerline and orientation based on a previous cavitator position and velocity information. This is shown as the delayed approach in Figure 4.10.

In this section, a model is presented which uses both a delayed cavity approach

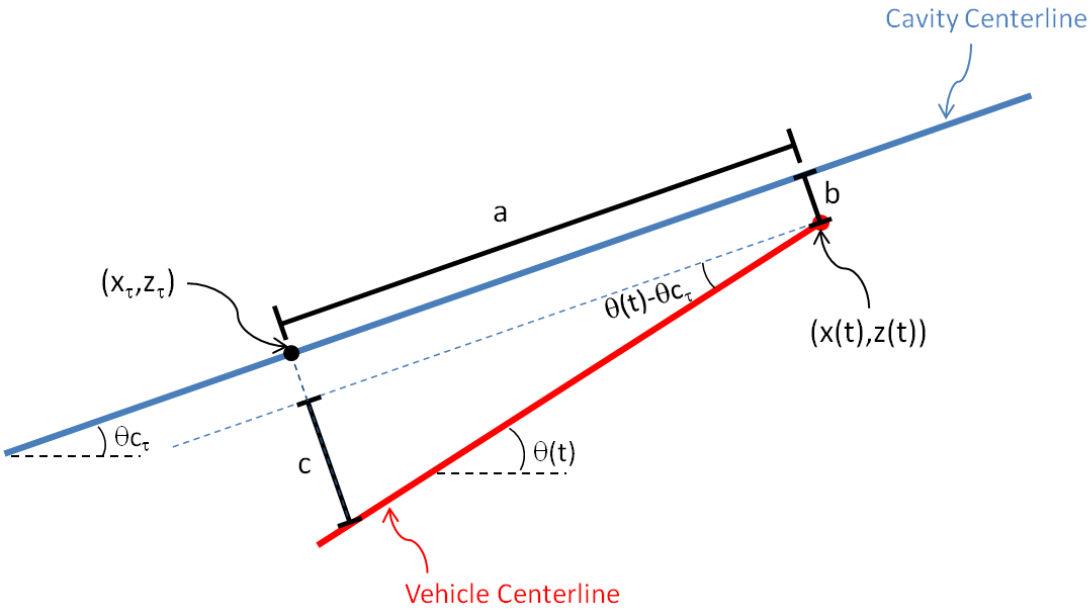

Figure 4.11: Cavity and vehicle centerlines for the delayed case.

to generate cavity location and orientation for planing, as well as a planing force formulation that includes vehicle motions into and out of the fluid. For simplification and computational purposes, only cylindrical cavities are considered. However, the approach may be extended to account for non-cylindrical cavity planing.

4.2.1 Description of Immersion Terms

A depiction of the cavity and vehicle centerlines for an arbitrary vehicle position is shown in Figure 4.11. The portion of the cavity that interacts with the vehicle is generated by previous positions and orientations of the cavitator. When using a cylindrical cavity approximation, the cavity radius and location can be calculated by using a single previous cavitator position and orientation (a single delay). The delay is taken as τ seconds, which corresponds to the amount of time it took for

the cavitator to move from the position of interest (where the planing is occurring at the back of the vehicle) to where it is currently. In the figure, the cavity center is located at the previous nose position (x_τ, z_τ). The cavity expands in a radial direction perpendicular to the velocity direction at the previous time, making the cavity axis parallel to the delayed velocity direction. The cavity angle with respect to horizontal is denoted as θc_τ and can be expressed as shown in Eq. (4.11). In this expression, θ_τ represents the delayed body orientation with respect to horizontal, and $tan^{-1}(w_\tau/V)$ represents the delayed velocity orientation with respect to the body.

$$\theta c_\tau = \theta_\tau - tan^{-1}(w_\tau/V) \tag{4.11}$$

The relative position of the rear of the body with respect to the cavity centerline is a function of both a translation and a body rotation. The translation of the current position of the nose with respect to the cavity centerline is expressed as b. The relative angle between the current body centerline and the cavity centerline can be expressed as $\theta(t) - \theta c_\tau$, where $\theta(t)$ is the current body orientation with respect to horizontal. The displacement due to body rotation, c, can be expressed as $c = a \cdot tan(\theta(t) - \theta c_\tau)$. The radial displacement of the body centerline at the rear with respect to the cavity at (x_τ, z_τ), is simply $b + c$.

The immersion depth h can then be described as given in Eq. (4.12), where $\Delta = Rc - R$; this is a simplified expression for immersion only along one surface. The immersion rate can then be generated by differentiating Eq. (4.12) which yields

Eq. (4.13). The delay terms are treated as having no dependence on time. They relate only to a specific instance in time which is used to generate an instantaneous cavity orientation in space for use in the calculation of the planing forces. With the exception of expansion and contraction along the cavity radial direction, this instantaneous cavity does not move or change. This corresponds to the physical understanding that the cavity is not moving in space once created; that is it is simply expanding or contracting.

$$h = a \cdot tan(\theta(t) - \theta c_\tau) + b - \Delta \tag{4.12}$$

$$\dot{h} = a \cdot sec^2(\theta(t) - \theta c_\tau) \cdot q(t) + \dot{a} \cdot tan(\theta(t) - \theta c_\tau) + \dot{b} - \dot{R}c \tag{4.13}$$

The terms $\dot{a}$ and $\dot{b}$ represent the motion of the vehicle nose relative to the fixed cavity. These terms are the axial and radial (with respect to the cavity axis) components of the nose velocity. Going back to the immersion rate expression in Eq. (4.13), the first term relates to the rotation of the body into the cavity, the second term relates to the fact that the body is moving through the cavity with a relative angle, the third term relates to the rigid body motion of the vehicle into the fluid, and the last term relates to the cavity radial growth rate.

The parameters a and b can be solved by using geometry. In Figure 4.12, the orientation of a and b, along with (x_τ, z_τ) and $(x(t), z(t))$, are shown. The line segment that joins (x_τ, z_τ), and $(x(t), z(t))$, creates an angle of $\theta_x = tan^{-1}\left(\frac{z_\tau - z(t)}{x(t) - x_\tau}\right)$ with the horizontal; the term is $z_\tau - z(t)$ since z is positive in the downward direction.

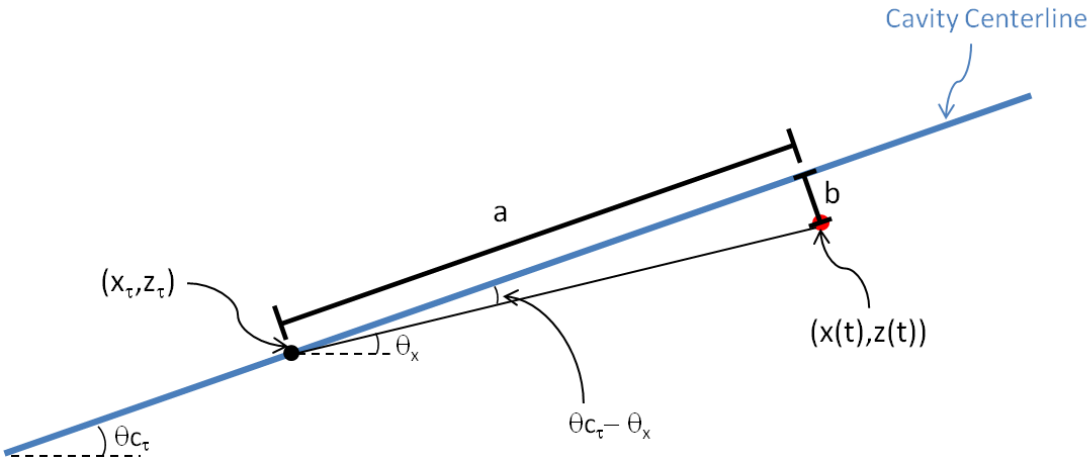

Figure 4.12: Parameters a and b in relation to cavity centerline.

The relative angle that this segment creates with the cavity axis is simply $\theta c_\tau - \theta_x$. The parameters a and b can then be expressed as in Eqs. (4.14)-(4.15). By expanding the *sin* and *cos* terms, the expressions can be simplified to Eqs. (4.16)-(4.17). The rate of change can then be expressed as given in Eqs. (4.18)-(4.19). As described earlier, these terms can also be considered as the axial and radial components (with respect to the cavity axis) of the vehicle velocity at the nose.

$$a = \sqrt{(z_\tau - z(t))^2 + (x(t) - x_\tau)^2} \cdot cos\left(\theta c_\tau - tan^{-1}\left(\frac{z_\tau - z(t)}{x(t) - x_\tau}\right)\right) \tag{4.14}$$

$$b = \sqrt{(z_\tau - z(t))^2 + (x(t) - x_\tau)^2} \cdot sin\left(\theta c_\tau - tan^{-1}\left(\frac{z_\tau - z(t)}{x(t) - x_\tau}\right)\right) \tag{4.15}$$

$$a = cos(\theta c_\tau)(x(t) - x_\tau) + sin(\theta c_\tau)(z_\tau - z(t)) \tag{4.16}$$

$$b = sin(\theta c_\tau)(x(t) - x_\tau) - cos(\theta c_\tau)(z_\tau - z(t)) \tag{4.17}$$

$$\dot{a} = \dot{x} \cdot cos(\theta c_\tau) - \dot{z} \cdot sin(\theta c_\tau) \tag{4.18}$$

$$\dot{b} = \dot{x} \cdot sin(\theta c_\tau) + \dot{z} \cdot cos(\theta c_\tau) \tag{4.19}$$

As an aside, the impacting planing force expressions can be solved for the non-delayed case. In the case with no delay, the cavity is directly related to the current conditions at the nose, and the axis of the cavity is oriented along the current velocity direction. For no delay, $\theta_\tau = \theta(t)$, $w_\tau = w(t)$, $z_\tau = z(t)$, and $b = \dot{b} = 0$. The expression for the immersion depth becomes $h_{non\_delay} = a \cdot w/V - \Delta$ where V is the forward vehicle speed (as used in the dynamics modeling). The immersion rate simplifies to $\dot{h}_{non\_delay} = a \cdot sec^2(tan^{-1}(w/V)) \cdot q + \dot{a} \cdot w/V - \dot{R}c$, where $\dot{a}$ is total vehicle speed.

4.2.2 Integration into Dynamics Model

In order to incorporate the delay, the overall vehicle path needs to be accurately tracked in the inertial frame. The small angle assumptions can be removed from the propagation of the depth state z and an additional state for the x position can be added to the equations of motion represented by Eqs. (2.1) and (2.2). The expressions for $\dot{z}$ and $\dot{x}$ are shown as follows.

$$\dot{z} = w \cdot cos(\theta) - V \cdot sin(\theta) \tag{4.20}$$

$$\dot{x} = V \cdot cos(\theta) + w \cdot sin(\theta) \tag{4.21}$$

The planing force is calculated from the Paryshev representation [37], which is solved for the cylinder on cylinder case. The resulting planing force can then be

represented as shown in Eq. (4.22), where $\Delta = R_c - r$, and h_0 is the immersion depth at the aft of the vehicle, as shown in Figure 4.9.

$$F_P = \pi \rho r^2 \dot{h}^2 \frac{1}{tan(\alpha)} \left(1 - \frac{\Delta^2}{(h_0 + \Delta)^2}\right) \tag{4.22}$$

4.2.3 Simulation Results

For the simulation runs, the vehicle parameters were chosen to match those used in the previous runs with $m = 2$, $R_n = 0.0191\ m$, $R = 0.0508\ m$, $L = 1.8\ m$, $n = 0.5$, and $C_{x0} = 0.82$. Feedback control is again described by Eqs. (2.6) where the fins are assumed to be passive, while the cavitator utilizes linear state feedback. The nominal value for the delay simulations is chosen as $\tau = L/V$, the approximate amount of time it takes for the vehicle nose to travel one body length. For low cavitation numbers (high speeds), the system shows a stable equilibrium response. Similar to the other dynamics models with the same feedback formulation, this system exhibits oscillations as the cavitation number is increased (speed is decreased) and the cavity to body clearance tightens.

A simulation run conducted for $\sigma = 0.0241$ ($V = 83.68\ m/s$) is shown for the delayed system in Figure 4.13. This particular value of σ is chosen to be just below the critical cavitation number where limit-cycle motion is observed.

A simulation run for the non-delayed system at the same cavitation number $\sigma = 0.0241$ is shown in Figure 4.14. Here the non-delayed system exhibits limit cycles. It should be noted that for high speeds (low cavitation numbers), the non-

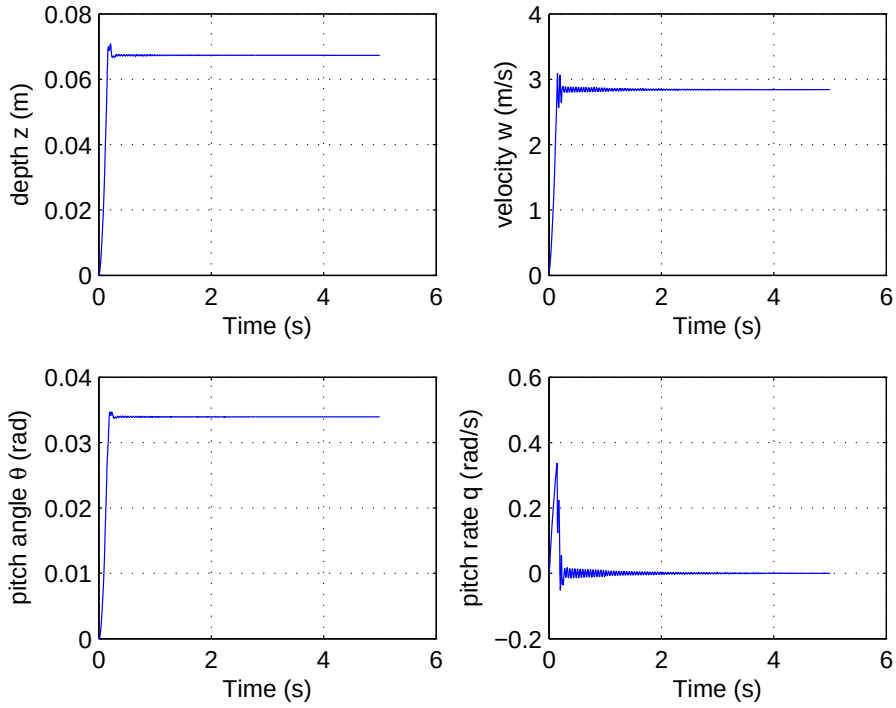

Figure 4.13: System response results for $\sigma = 0.0241$ and delayed system.

delayed system does demonstrate stable behavior. So when starting from sufficiently high speeds, as the cavitation number is increased, both the delayed and non-delayed system transition from stable to limit-cycle motions. However, the transition for the non-delayed system occurs slightly earlier. It is within this window of cavitation numbers, where the equilibrium position of the delayed system is stable and the non-delayed system is unstable, that the delay can be considered stabilizing. This is in contrast to previous findings where the delay can be shown to destabilize the system

If the delay is taken as a parameter, and the forward velocity is held constant at $V = 83.68\ m/s$, the steady-state behavior of the system follows the plots shown

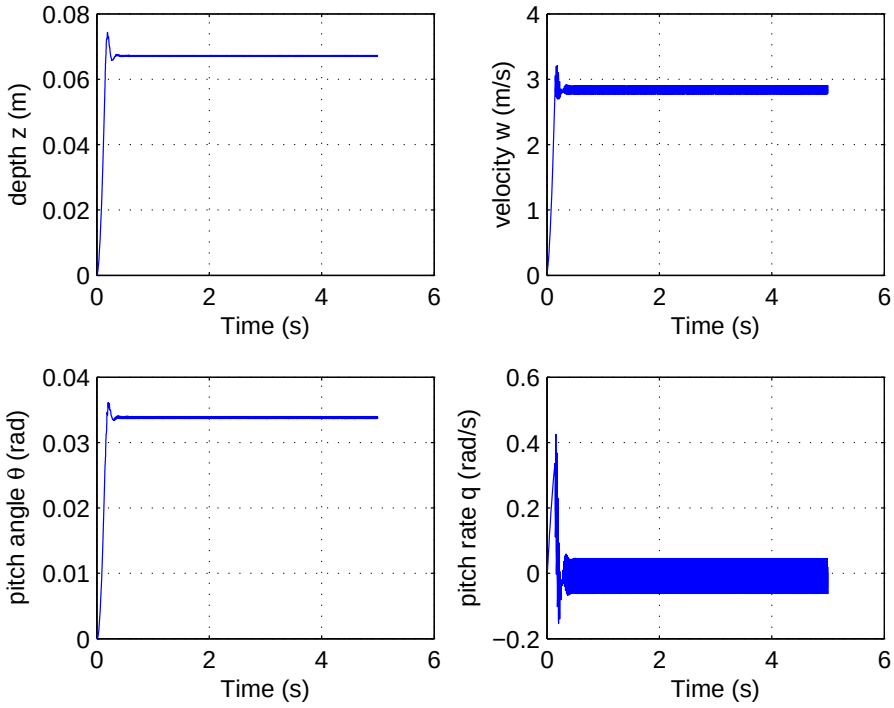

Figure 4.14: System response results for $\sigma = 0.0241$ and non-delayed system.

in Figure 4.15. Here, the delay is varied from close to 0 s (no delay) to 0.01936 s (approximately 90% of the nominal delay value of L/V). The system can be shown to transition from limit-cycle motion to asymptotic stability as the delay is increased. By varying the delay with a fine timestep of less then 0.00001 s, the critical value of $\tau = 0.01930$ s can be found, where limit cycles exist for $\tau < 0.01930$ s.

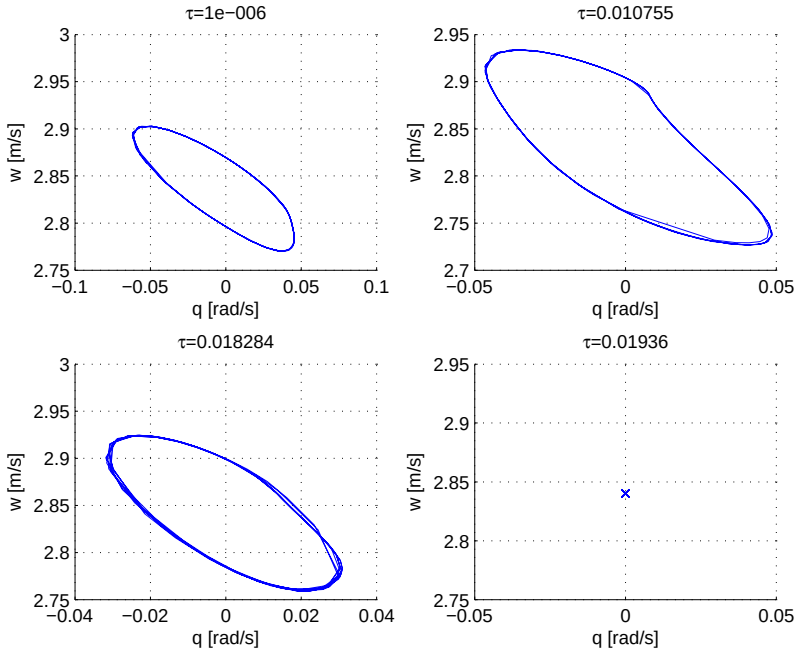

Figure 4.15: Effect of delay on steady-state system response.

Chapter 5

Vehicle Maneuvering Using Numeric Optimal Control Approach

In this chapter, a framework is provided for analyzing maneuvering of non-smooth vehicle systems. Maneuverability, for nonlinear and particularly for non-smooth vehicle systems, can be difficult to characterize since "all out" or fully saturated control inputs do not necessarily define the envelope of vehicle motion capabilities. For example, in the case of supercavitating vehicles, a fully saturated control input will push the system into tailslap which negatively affects the position control of the vehicle. In this work, a numeric, direct optimal control approach has been used for generating optimal control inputs for defined vehicle maneuvers. This approach is applied to the supercavitating vehicle systems presented in the previous chapters. The supercavitating systems are complex examples of non-smooth dynamic systems, they serve as good candidates for numerical approaches.

5.1 General Approach

Due to the complexity, and non-differentiable nature of non-smooth systems, the direct method for optimal control was chosen. In this method, controller inputs are determined numerically. The control inputs for discrete segments of time, or parameters that are used to define a control input function, are treated as variables in an optimization scheme. The system dynamics can be directly integrated by

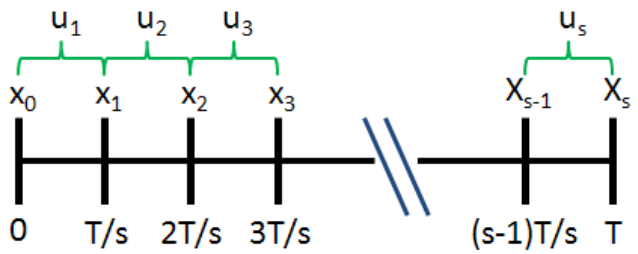

Figure 5.1: Diagram of discretization method for the optimization strategy used to generate controller input.

using the governing equations of motion. The maneuver itself can be treated as a constraint on the optimization formulation, constraining the dynamics to perform a desired task. The control input(s) can then be optimized for total time (which can also be treated as a variable), or ending state, depending on the type of maneuver considered.

A simple example of an application would be a maneuver subject to optimization for total time of maneuver T, which has end point constraints (such as final position and orientation constraints). The maneuver can then be discretized into s equal length time segments where the control input is constant over each time segment, as shown in Figure 5.1. The values for the control u_i for $i = 1 \ldots s$ as well as the final time T are considered as variables in the optimization scheme. The dynamics can then be directly integrated from a given initial state x_0 and with the final position x_s, subject to the constraints determined by the type of maneuver being considered. This type of maneuver is illustrated in Figure 5.2.

The optimization formulation can be described as follows. The objective func-

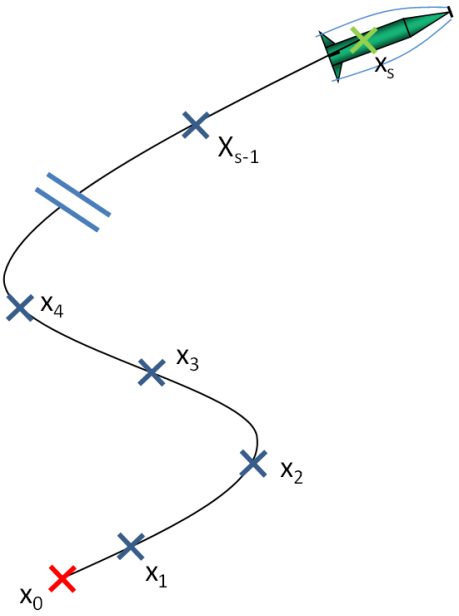

Figure 5.2: Diagram of trajectory generated by using the constant control inputs over discretized time segments.

tion can be expressed as given in Eq. (5.1). This function is subject to the constraint shown in Eq. (5.2), where s is the number of time intervals and x_f is defined by the maneuver. The state values at end of each of the time intervals can be expressed as shown in Eq. (5.3), for $i = 1...s$ and x_0 a given. Additional constraints can also be applied to bound the control inputs and/or states.

$$min_{u_1,u_2,...,u_s,T}(T) \tag{5.1}$$

$$x_s = x_f \tag{5.2}$$

$$x_i = \int_{t=(i-1)T/s,x_{i-1}}^{t=iT/s} F(t,x,u_i)dt \tag{5.3}$$

An important consideration in this formulation is that this formulation in-

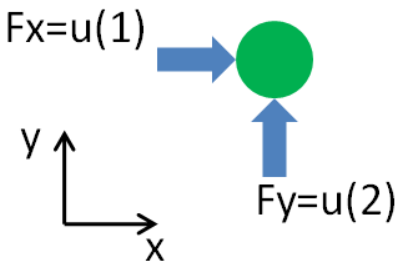

Figure 5.3: Simple point mass controlled system.

herently only considers trajectories that the system is capable of achieving (since the dynamics are directly integrated). This eliminates the need to determine a set of achievable trajectories as done with some path planing methods. However, end conditions must be chosen with care, since an un-achievable end condition means that there is an empty feasible set of variables for the optimization formulation.

5.1.1 Application to Simple System

To better illustrate the optimal control method, it is applied to a planar point mass system. The system is shown in Figure 5.3, wherein the inputs are F_x and F_y. They represent the forces along the x and y directions respectively. The equations of motion are given by Eq. (5.4), where the state vector is given by $(x, y, \dot{x}, \dot{y})$.

$$\frac{d}{dt}\begin{Bmatrix} x \\ y \\ \dot{x} \\ \dot{y} \end{Bmatrix} = \begin{Bmatrix} \dot{x} \\ \dot{y} \\ \ddot{x} \\ \ddot{y} \end{Bmatrix} = \begin{Bmatrix} \dot{x} \\ \dot{y} \\ u(1) \\ u(2) \end{Bmatrix} \tag{5.4}$$

$t\ (s)$	$x\ (m)$	$y\ (m)$	$\dot{x}\ (m/s)$	$\dot{y}\ (m/s)$	$F_x\ (N)$	$F_y\ (N)$
0.5	0.5	0.5	2.2	2.2	5.0	5.0
0.9	2.0	2.0	4.5	4.5	5.0	5.0

Table 5.1: Optimal solution for point mass system for starting point $(0.0m, 0.0m, 0.0m/s, 0.0m/s)$ and end condition $(2.0m, 2.0m, \_, \_)$ and $s = 2$.

The control forces are bounded to $[-5N, 5N]$. The control inputs are calculated by using the constrained optimizer in Matlab, *fmincon*. Simple maneuvers are considered first, with $s = 2$ and an initial condition of $x_0 = (0.0m, 0.0m, 0.0m/s, 0.0m/s)$ (which corresponds to an initial position at the origin, with zero speed). A solution for a maneuver that is only defined by a final position is shown in Table 5.1, where $(x_f, y_f) = (2.0m, 2.0m)$ (any velocity at final position allowed). The optimal solution for a fastest time maneuver is a "full-on", $u = 5.0$, style control. A second maneuver that defines both the final position and final velocity is shown in Table 5.2. Here, the maneuver is defined with the end point $(x_f, y_f, \dot{x_f}, \dot{y_f}) = (2.0m, 2.0m, 0.0m/s, 0.0m/s)$, which can be thought of as a move-to and stop. The optimal control inputs for this maneuver are a "full-on" $(u = 5.0)$ time segment, followed by a"full-stop" $(u = -5.0)$ control. The solution for these symmetric position and velocity end conditions are not surprising, and they can easily be determined by inspection. The optimal control process discussed here can be applied to more complicated maneuvers.

The optimal time solution for a maneuver to the end point $(x_f, y_f, \dot{x_f}, \dot{y_f}) =$

$t\ (s)$	$x\ (m)$	$y\ (m)$	$\dot{x}\ (m/s)$	$\dot{y}\ (m/s)$	$F_x\ (N)$	$F_y\ (N)$
0.3	0.3	0.3	1.6	1.6	5.0	5.0
0.6	1.0	1.0	3.1	3.1	5.0	5.0
.09	1.8	1.8	1.6	1.6	-5.0	-5.0
1.3	2.0	2.0	0.0	0.0	-5.0	-5.0

Table 5.2: Optimal solution for point mass system for startint point $(0.0m, 0.0m, 0.0m/s, 0.0m/s)$ and end condition $(2.0m, 2.0m, 0.0m/s, 0.0m/s)$ and $s = 2$.

$(1.0m, 7.0m, -1.0m/s, 2.0m/s)$ is less intuitive, and the best result found from the optimization process is shown in Table 5.3. The trajectory as well as the time histories of the sates are also shown in Figure 5.4. The resulting motion can be seen to move around in the x direction; this is due to the fact that the limiting factor for fastest time maneuver was the motion in the y direction. Although the solution here is more difficult to ascertain via inspection, simple systems are only useful to validate the numeric optimal control approach. This type of approach is intended for more complex systems.

5.2 Maneuvering with Cylindrical Dive-Plane Models

The optimal control approach is applied to a supercavitating vehicle system. The first system considered is based on the original cylindrical cavity, dive-plane

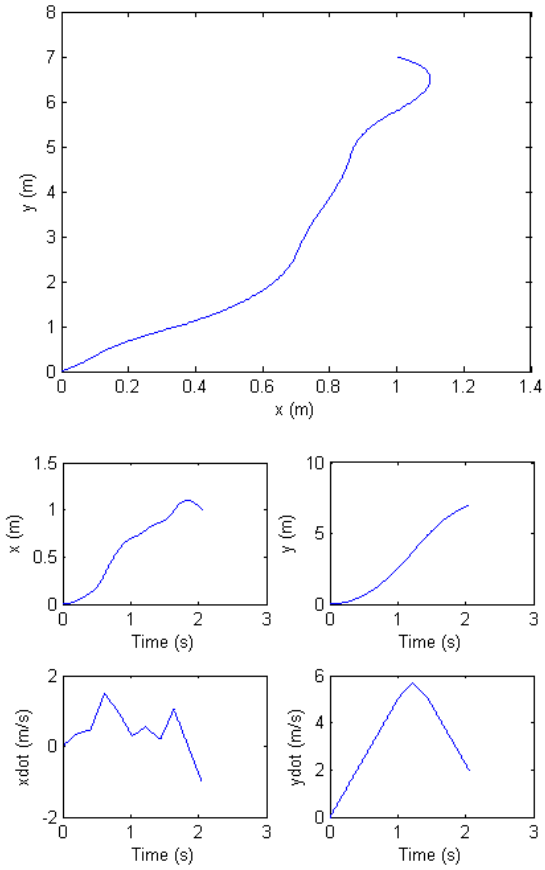

Figure 5.4: Best solution for point mass system for starting point $(0.0m, 0.0m, 0.0m/s, 0.0m/s)$ and end condition $(1.0m, 7.0m, -1.0m/s, 2.0m/s)$ and $s = 10$.

$step:$	1	2	3	4	5	6	7	8	9	10
$F_x\ (N)$	5.0	4.5	-3.4	-5.0	-5.0	5.0	1.1	2.8	-5.0	-5.0
$F_y\ (N)$	5.0	5.0	5.0	5.0	5.0	4.8	-5.0	-5.0	-5.0	-5.0
										$T = 2.0$

Table 5.3: Best solution for point mass system for starting point $(0.0m, 0.0m, 0.0m/s, 0.0m/s)$ and end condition $(1.0m, 7.0m, -1.0m/s, 2.0m/s)$ and $s = 10$.

model, which utilizes the Hassan planing force model (as used in reference [8]). This model was chosen to implement first because of it's simplicity (compared to the subsequent modified models), while the system still exhibited behavior such as limit-cycle motions, and unstable responses.

Similar to the delayed system, maneuvering considerations require accurate tracking of the inertial position. An additional state for the x coordinate is added, and the expression for the propagation of z is adjusted to remove the small angle assumptions. The state space representation of the inertial states, x and z, are shown in Eqs. (5.5)-(5.6).

$$\dot{x} = V \cdot cos(\theta) + w \cdot sin(\theta) \tag{5.5}$$

$$\dot{z} = w \cdot cos(\theta) - V \cdot sin(\theta) \tag{5.6}$$

Additional constraints are applied to the supercavitating vehicle system. Actuation angles for both the fin and cavitator control surfaces are bounded, and

these can be applied as direct bounds on the optimization variables. Additionally, since the planing force model is only valid for small immersions, state limits on the transverse speed, $|w| < 6\ m/s$, are applied. The constraint equations can then be specified as shown in Eq. (5.7) and Eq. (5.8); $c_{eq} = 0$ constrains the end condition, and $c_i \leq 0$ is used to apply bounds on the transverse velocity at the end of each time interval. Unless otherwise specified, for these runs, $\sigma = 0.03$, which corresponds to a velocity (cavity size) where the system experiences limit-cycle motions and unstable behavior. All runs start with an initial condition of straight and level flight originating from $(z_0, x_0, w_0, q_0) = (0.0m, 0.0m, 0.0m/s, 0.0rad/s)$. The optimization (unless otherwise specified) was carried out by using an off the shelf constrained optimizer, *fmincon*, in Matlab (and specifically the interior point algorithm for this function).

$$c_{eq} = x_f - x_s \tag{5.7}$$

$$c_i = |w_i| - 6 \qquad \forall i = 1 \ldots s \tag{5.8}$$

If the optimal control approach is applied without the aid of feedback control, certain solutions can be found. An example of a slight dive maneuver is shown in Figure 5.5. This is a maneuver to $z_f = 2.0\ m$ and $w_f = 0.0\ m/s$, which corresponds to a dive-to-depth, and an alignment of the body with the total velocity direction. For this run $s = 8$ and an initial guess of zero cavitator input and zero fin input is applied. In this situation, the optimizer was capable of finding a solution with a feasible end condition. However, if the discretization was increased to $s = 16$, a feasible

solution by using the same starting condition could not be found. This finding was surprising, since the solution for $s = 8$ is clearly feasible for $s = 16$. Additionally, feasible solutions for other similarly simple maneuvers (including straight and level flight) could not be found, even with good initial conditions. The issue relates to the fact that the system without feedback control is inherently unstable (as shown in the previous work and in Chapter 2). As the optimizer searches for solutions that satisfy the end conditions, the system can easily transition into instability. When no feedback control is utilized, the optimal control method is tasked with generating a controller that stabilizes the system, while maneuvering it to the proper end condition. However, with the exception of some specific cases, the coarseness of the discretization used for the optimal control approach was found to be incapable of rejecting planing instabilities.

5.2.1 Inner-Loop and Outer-Loop Control Schemes

A feedback controller can be added to the system. The feedback controller can be considered as an "inner-loop" controller that is used to help reject fast timescale instabilities (such as with the planing force), while the control inputs generated by the optimization can be considered as "outer-loop" control that guides the vehicle through the desired maneuver to the proper end condition. A diagram of how the two controllers are integrated is shown in Figure 5.6. Here, the optimization formulation plays the role of the motion planner.

By utilizing the liner feedback law shown in Eqs. (2.6), the system is stabilized

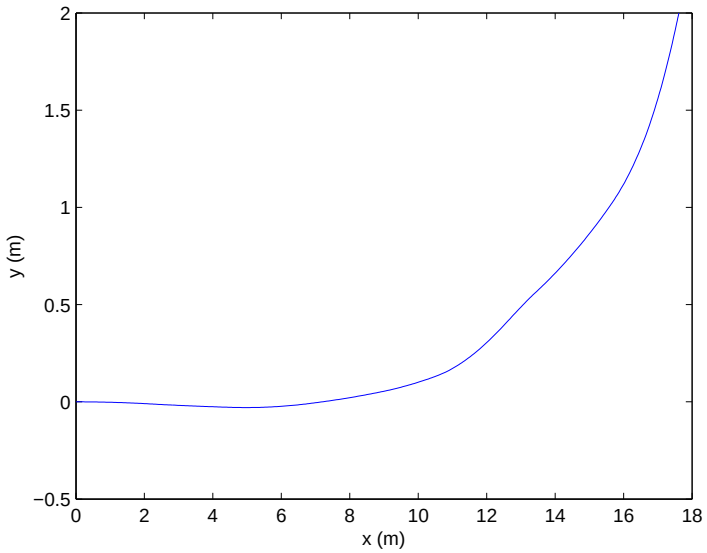

Figure 5.5: Trajectory for dive maneuver to $z_f = 2.0\ m$ and $w_f = 0.0\ m/s$ with no feedback control and $s = 8$.

to stable limit cycles. The response time histories for a solution using this feedback law for straight and level flight is shown in Figure 5.7, along with the determined controller inputs in Figure 5.8. Here, the maneuver requires an end condition of $(x_f, z_f, w_f) = (40.0m, 0.0m, 0.0m/s)$ with all other final states unconstrained. By using an initial guess of constant fin input of $\delta_f = 0.1\ rad$ (approximately what is

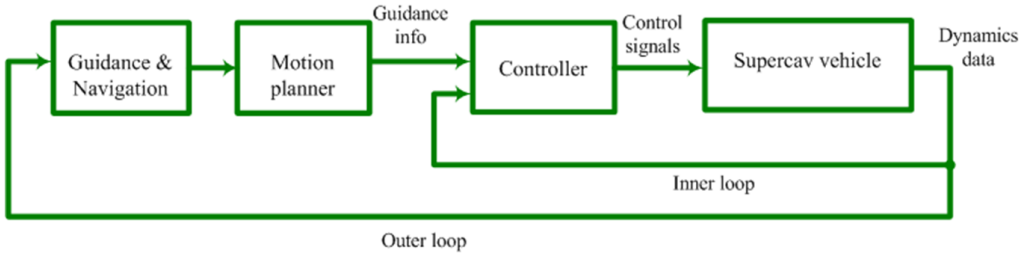

Figure 5.6: Depiction of inner-loop and outer-loop controllers.

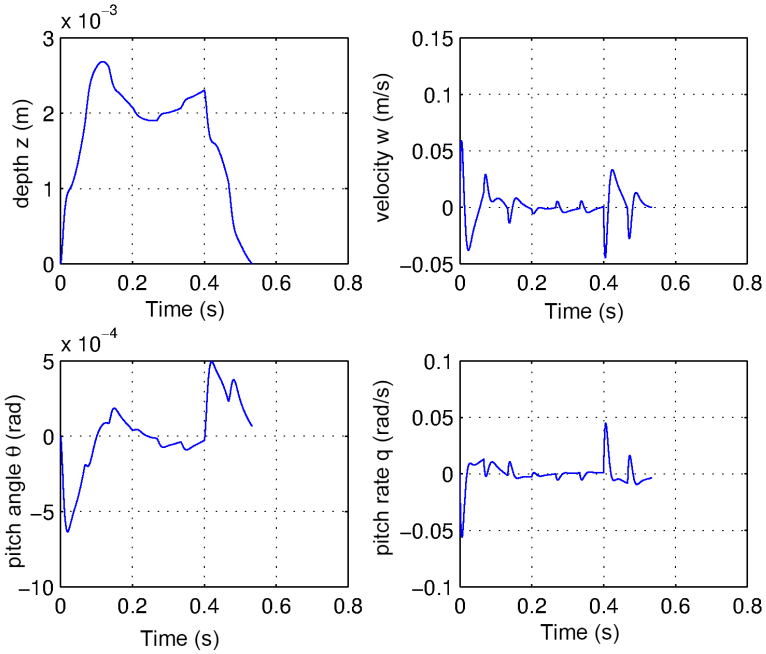

Figure 5.7: Time histories for maneuver to $(x_f, z_f, w_f) = (40.0m, 0.0m, 0.0m/s)$ with feedback control according to Eqs. (2.6) and $s = 8$.

required to support the rear of the vehicle), the optimization scheme was easily able to find a good set of control inputs.

One issue with this particular form of feedback is that it directly involves the inertial states z and θ. Unfortunately, this greatly limits the ability to perform maneuvers aside from straight and level flight. Instead, the inertial terms can be dropped and an inner-loop control of the form as shown in Eq. (5.9) can be utilized. This type of controller still aids in stabilizing the system (using measurable states), while allowing for motions in space.

$$\delta_{c\_inner} = k_{inner} q \tag{5.9}$$

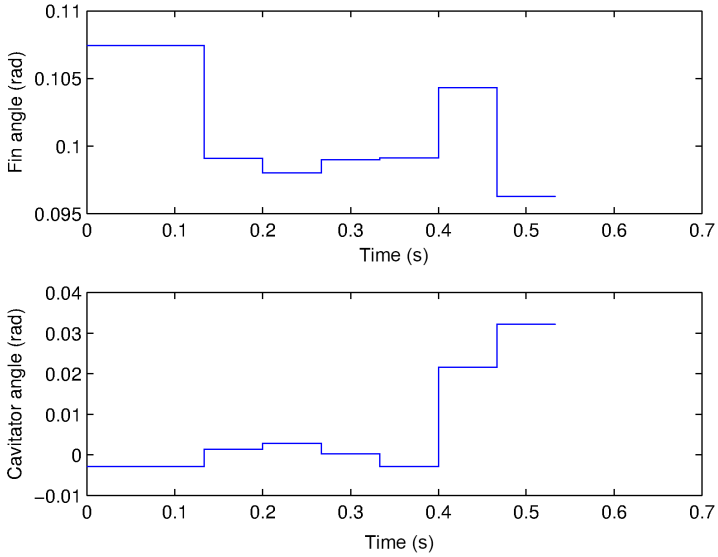

Figure 5.8: Outer-loop control inputs for maneuver to $(x_f, z_f, w_f) = (40.0m, 0.0m, 0.0m/s)$ with feedback control according to Eqs. (2.6) and $s = 8$.

By using $k_{inner} = -0.9$, a dive maneuver to $z_f = 2\ m$ and $w_f = 0\ m/s$ is considered (all other final states being unconstrained). The resulting state and outer-loop control histories for the best solution are shown in Figures 5.9 and 5.10. An initial guess of zero cavitator or fin control angles is utilized here with $s = 8$. Also, unlike the case with no inner-loop control, control inputs for similar simple maneuvers can be easily solved. Deeper dive maneuvers can be solved relatively quickly by seeding the optimization scheme with previous solutions for shallower maneuvers. Trajectories for dive maneuvers to $z_f = 4.0$, 8.0 and 20.0 m, are shown in Figure 5.11 (again with $w_f = 0$).

With the inner-loop stabilization, more complicated maneuvers can also be considered. A dive followed by a level-off maneuver can be described with $z_f = 20.0$

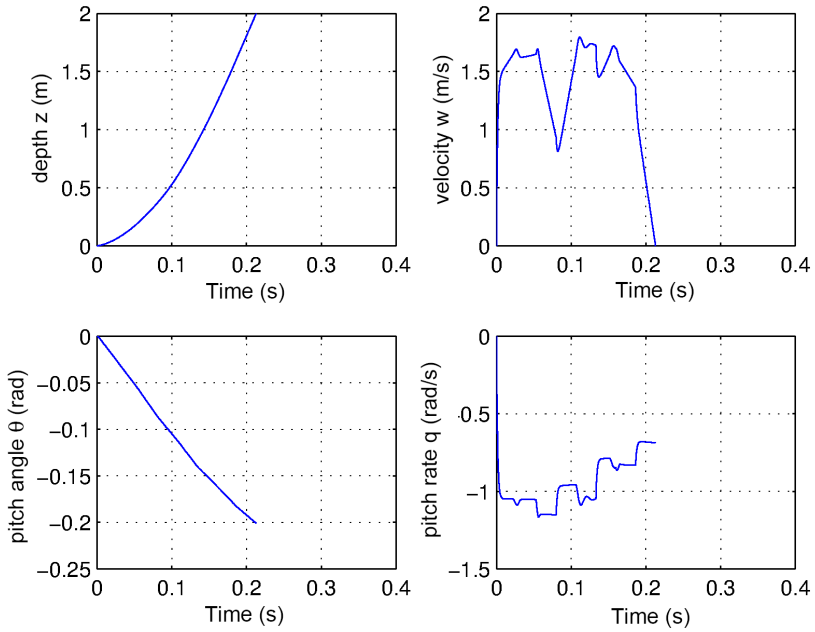

Figure 5.9: Time histories for maneuver to $(z_f, w_f) = (2.0m, 0.0m/s)$ with modified feedback control according to Eq. (5.9), $k_{inner} = -0.9$, and $s = 8$.

m and $\theta_f = 0.0\ rad$. This maneuver is solved with $s = 14$ and $k_{innner} = -0.9$, and the resulting trajectory and outer-loop control solution are shown in Figures 5.12 and 5.13, respectively.

5.2.2 Homing maneuvers

Move-to-point maneuvers are also of interest for maneuvering. These types of maneuvers can be characterized by specifying the final position (z_f, x_f). By using the results from the previous dive maneuvers, an obtainable move to point marker was chosen at $(z_f, x_f) = (20.0m, 80.0m)$. The resulting control solutions with $s = 14$ and $k_{inner} = -0.7$ are shown in Figures 5.14 and 5.15. Included in the trajectory plot

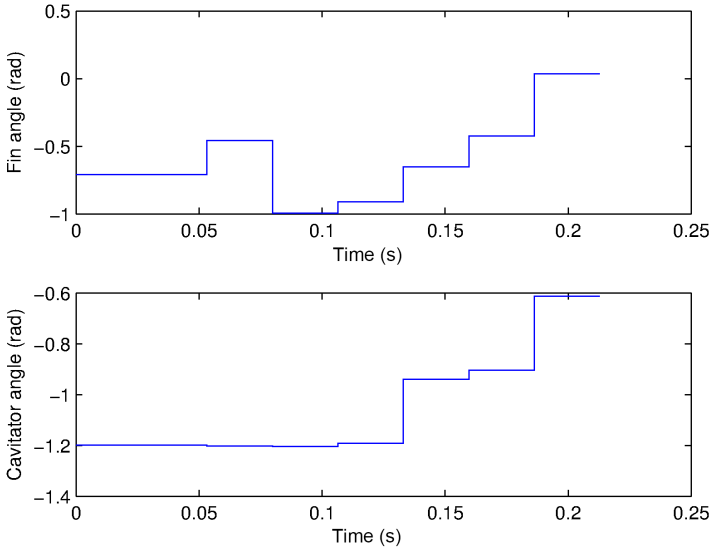

Figure 5.10: Outer-loop control inputs for maneuver to $(z_f, w_f) = (2.0m, 0.0m/s)$ with modified feedback control according to Eq. (5.9), $k_{inner} = -0.9$, and $s = 8$.

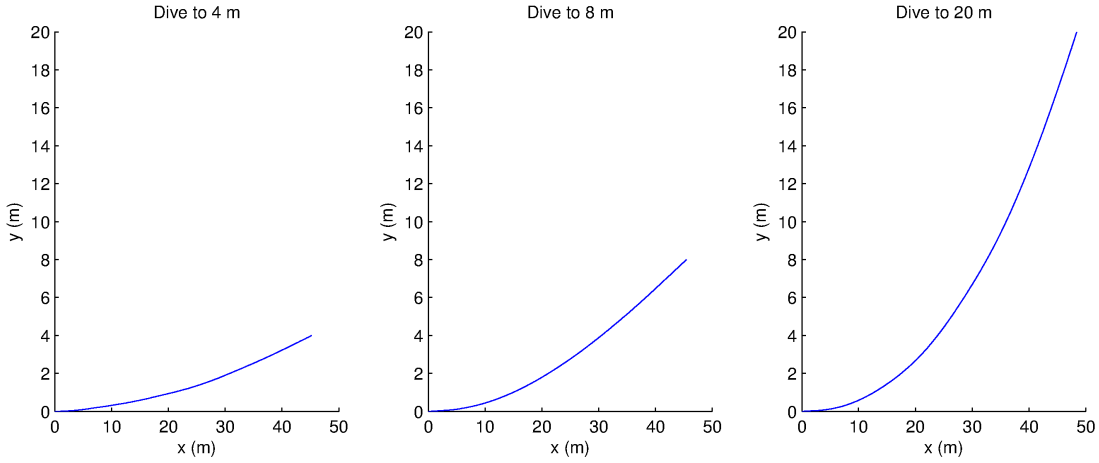

Figure 5.11: Trajectories for dive maneuvers to $(z_f, w_f) = (4.0m, 0.0m/s)$, $(z_f, w_f) = (8.0m, 0.0m/s)$, and $(z_f, w_f) = (20.0m, 0.0m/s)$, with modified feedback control according to Eq. (5.9), $k_{inner} = -0.9$, and $s = 8$.

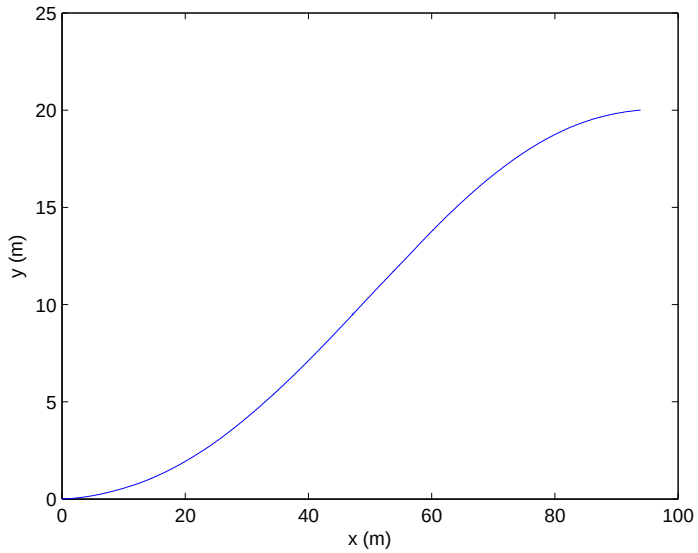

Figure 5.12: Trajectory for $(z_f, \theta_f) = (20.0m, 0.0rad)$ with modified feedback control according to Eq. (5.9), $k_{inner} = -0.9$, and $s = 14$.

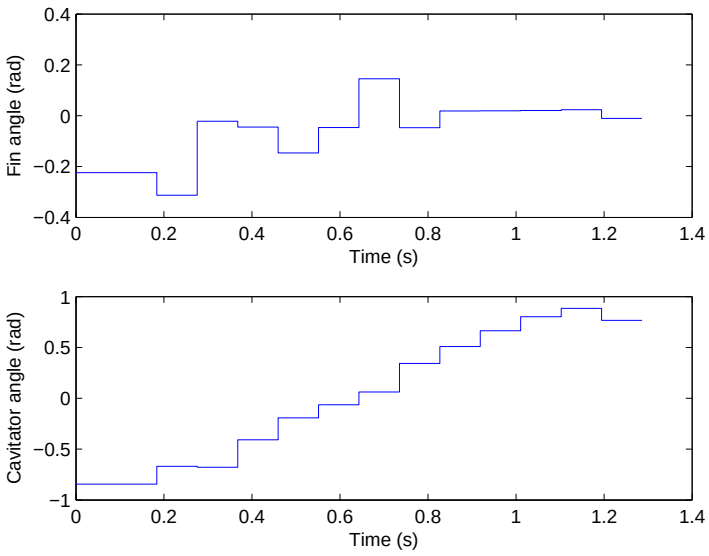

Figure 5.13: Outer-loop control inputs for maneuver to $(z_f, \theta_f) = (20.0m, 0.0rad)$ with modified feedback control according to Eq. (5.9), $k_{inner} = -0.9$, and $s = 14$.

of Figure 5.14, is a trajectory showing the vehicle path with inner-loop control only, as well as vehicle orientation and cylindrical cavity plots at specific points along the actual trajectory (exaggerated in size to show detail). It is clear that the vehicle is planing during the maneuver. The control history plot in Figure 5.15 also includes a total cavitator actuation angle plot showing the combination of the inner-loop and outer-loop control. Similar move to point maneuvers can also be solved. The resulting best solved trajectory for a climb maneuver to $(x_f, z_f) = (80.0m, -20.0m)$ is shown in Figure 5.16

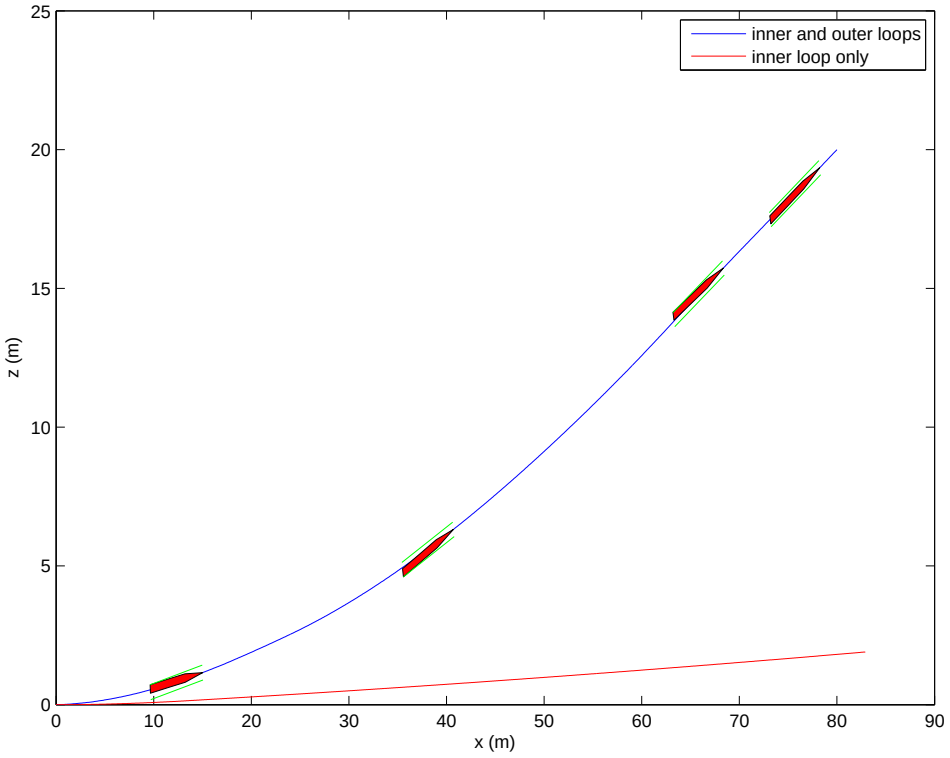

Figure 5.14: Trajectory for $(z_f, x_f) = (20.0m, 80.0m)$ with modified feedback control according to Eq. (5.9), $k_{inner} = -0.7$, and $s = 14$.

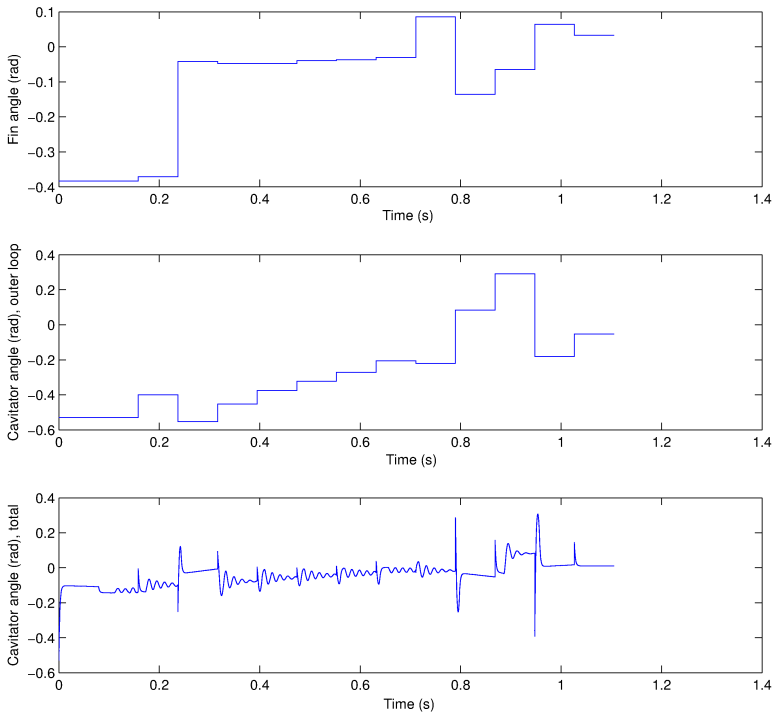

Figure 5.15: Control inputs for maneuver to $(z_f, x_f) = (20.0m, 80.0m)$ with modified feedback control according to Eq. (5.9), $k_{inner} = -0.7$, and $s = 14$.

Homing maneuvers with a circular obstacle or "no-fly" area are considered next. If the obstacle is centered at (x_{obst}, z_{obst}) with radius r_{obst}, the obstacle can be modeled as a single constraint that specifies a minimum distance from the obstacle center to the closest point along the trajectory. The constraint relationship can be expressed as in Eq. (5.10); the right-hand side expresses the closest distance to the obstacle center over the entire trajectory (determined by the integration of the equations of motion), and the radius of the obstacle r_{obst} specifies the minimum allowable distance.

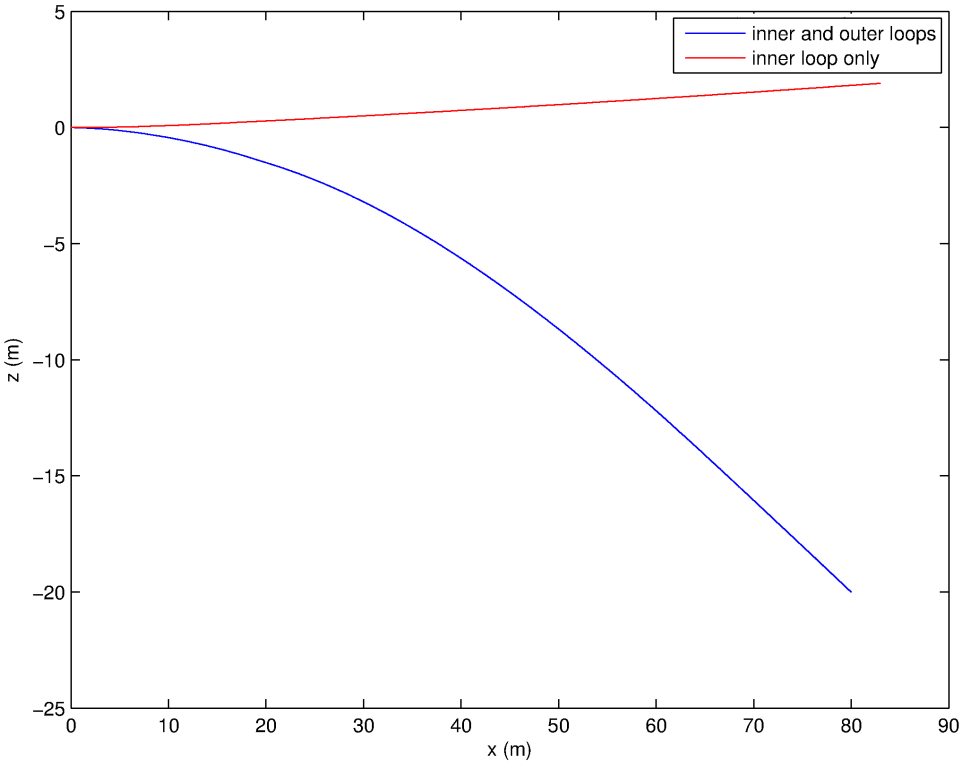

Figure 5.16: Trajectory for $(z_f, x_f) = (-20.0m, 80.0m)$ with modified feedback control according to Eq. (5.9), $k_{inner} = -0.7$, and $s = 14$.

$$r_{obst} \geq \min_t \sqrt{(x(t) - x_{obst})^2 + (z(t) - z_{obst})^2} \tag{5.10}$$

A climb maneuver to $(z_f, x_f) = (-20.0m, 80.0m)$ with an obstacle is centered at $(z_{obst}, x_{obst}) = (-5.0m, 40.0m)$ with a radius, $r_{obst} = 10.0\ m$ is then considered. The position is chosen so that the obstacle is located in the best found move-to-point trajectory, which has been generated for the obstacle-free case (as shown in Figure 5.16). The resulting trajectory is shown in Figure 5.17. The inner-loop only trajectory is also shown along with the vehicle-cavity orientation plots (exaggerated

in size). As expected, the best discovered trajectory has the vehicle operating under extreme maneuvering conditions (as shown by the high cavity immersion), and positions the path very close to the obstacle boundary. The response histories are plotted in Figure 5.18, and the control histories are shown in Figure 5.19.

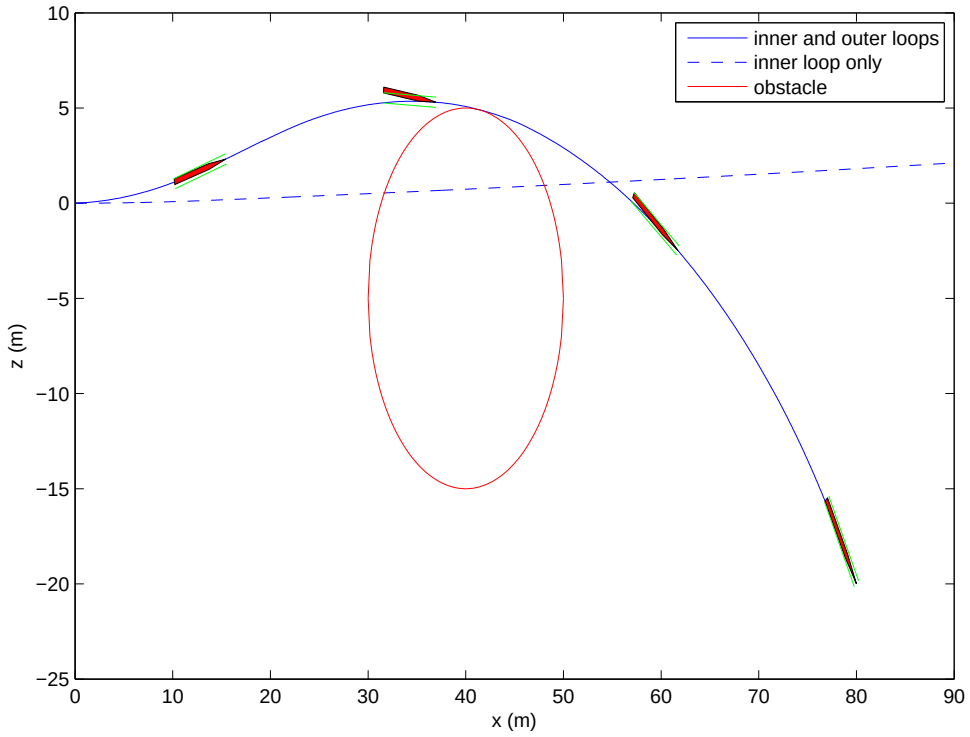

Figure 5.17: Trajectory for $(z_f, x_f) = (-20.0m, 80.0m)$, obstacle at $(z_{obst}, x_{obst}) = (-5.0m, 40.0m)$, $r_{obst} = 10.0\ m$. With modified feedback control according to Eq. (5.9), $k_{inner} = -0.7$, and $s = 14$.

Additional obstacles can be also be accommodated by using additional constraints. A run to a further point of $(z_f, x_f) = (-50.0m, 200.0m)$ is shown, with two obstacles at $(z_{obst}, x_{obst})_1 = (-5.0m, 40.0m)$, and $(z_{obst}, x_{obst})_2 = (-10.0m, 175.0m)$,

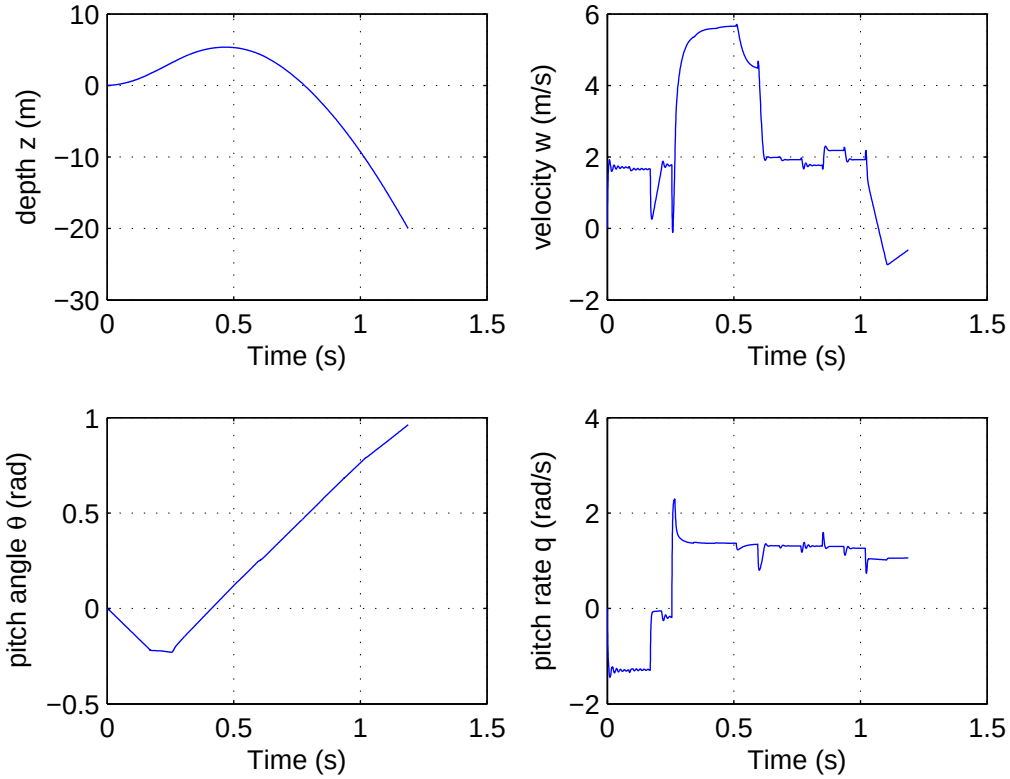

Figure 5.18: Time histories for $(z_f, x_f) = (-20.0m, 80.0m)$, obstacle at $(z_{obst}, x_{obst}) = (-5.0m, 40.0m)$, $r_{obst} = 10.0\ m$. With modified feedback control according to Eq. (5.9), $k_{inner} = -0.7$, and $s = 14$.

both with radius $r_{obst} = 15.0\ m$, is shown in Figure 5.20. The first obstacle was chosen to be in the path of the obstacle-free best discovered solution, and the second obstacle was chosen to be in the path of the single obstacle best discovered solution.

Moving end points can also be considered, and they are of interest since the vehicle motion does not occur instantaneously. A moving end point can be added by using an expression for the final end point constraint in terms of the final time T. An example is generated by setting $(x_f, z_f) = (80 + 10T, -20 - 10T)\ m$, letting

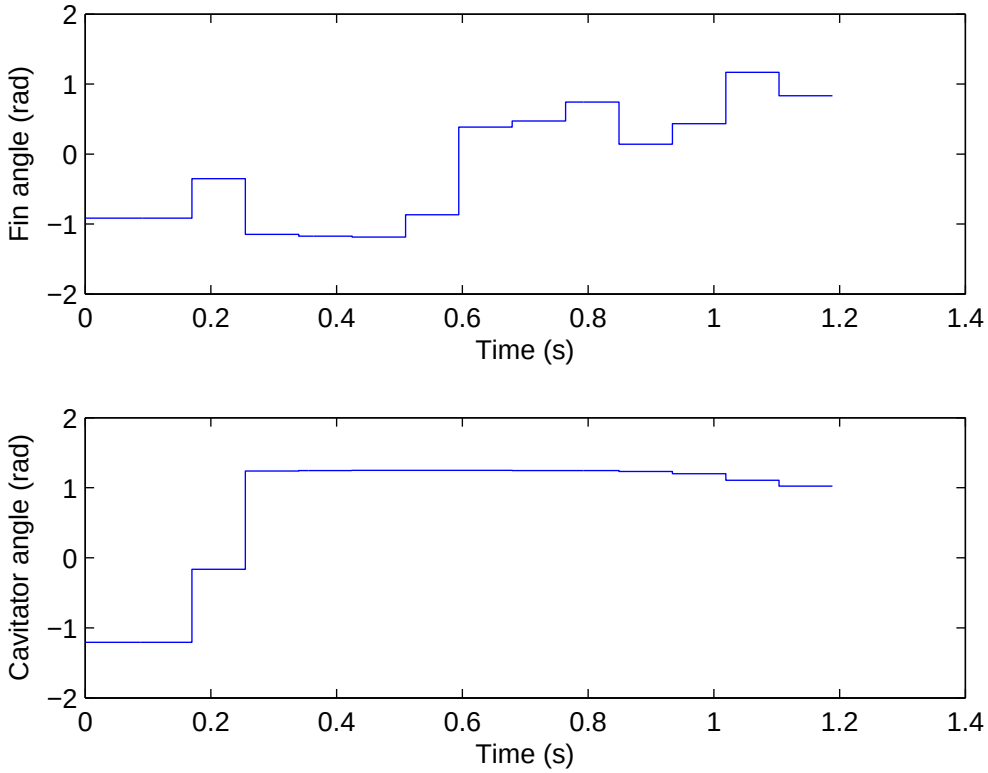

Figure 5.19: Outer-loop control inputs for $(z_f, x_f) = (-20.0m, 80.0m)$, obstacle at $(z_{obst}, x_{obst}) = (-5.0m, 40.0m)$, $r_{obst} = 10.0\ m$. With modified feedback control according to Eq. (5.9), $k_{inner} = -0.7$, and $s = 14$.

the desired end point start at $(x_f, z_f) = (80.0m, -20.0m)$, and giving a velocity of 10 m/s in both the x and z directions, away from the initial position of the vehicle. The plot of the resulting trajectory is shown in Figure 5.21.

5.3 Maneuvering with Non-Cylindrical Dive-Plane Models

The optimal control method was then applied to the non-cylindrical dive-plane models. As presented in Chapter 3, the non-smooth dynamics is complicated due to

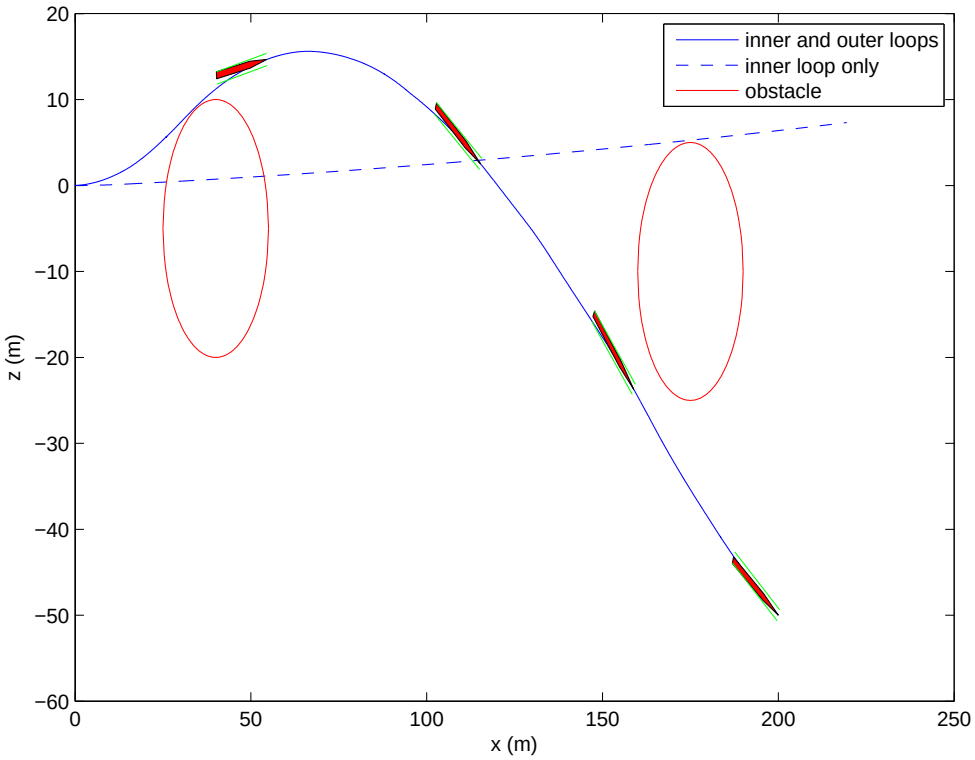

Figure 5.20: Trajectory for $(z_f, x_f) = (-50.0m, 200.0m)$, obstacles at $(z_{obst}, x_{obst})_1 = (-5.0m, 40.0m)$, and $(z_{obst}, x_{obst})_2 = (-10.0m, 175.0m)$, both with $r_{obst} = 15.0\ m$. With modified feedback control according to Eq. (5.9), $k_{inner} = -0.7$, and $s = 34$.

non-constant cavity boundaries (due to the cavity shift) and a varying planing force function (due to the cavity shape change). A homing maneuver is considered first by using the splined cavity model (to ensure accurate planing area predictions). A solution for dive maneuver to $x_f = 20.0\ m$, $z_f = 80.0\ m$ with $\sigma = 0.0335$, is shown in Figure 5.22. The vehicle orientation and non-cylindrical cavity plots at specific points along the trajectory are also shown, and are exaggerated in size to show detail. With the non-splined cavity model, the computational time was significantly

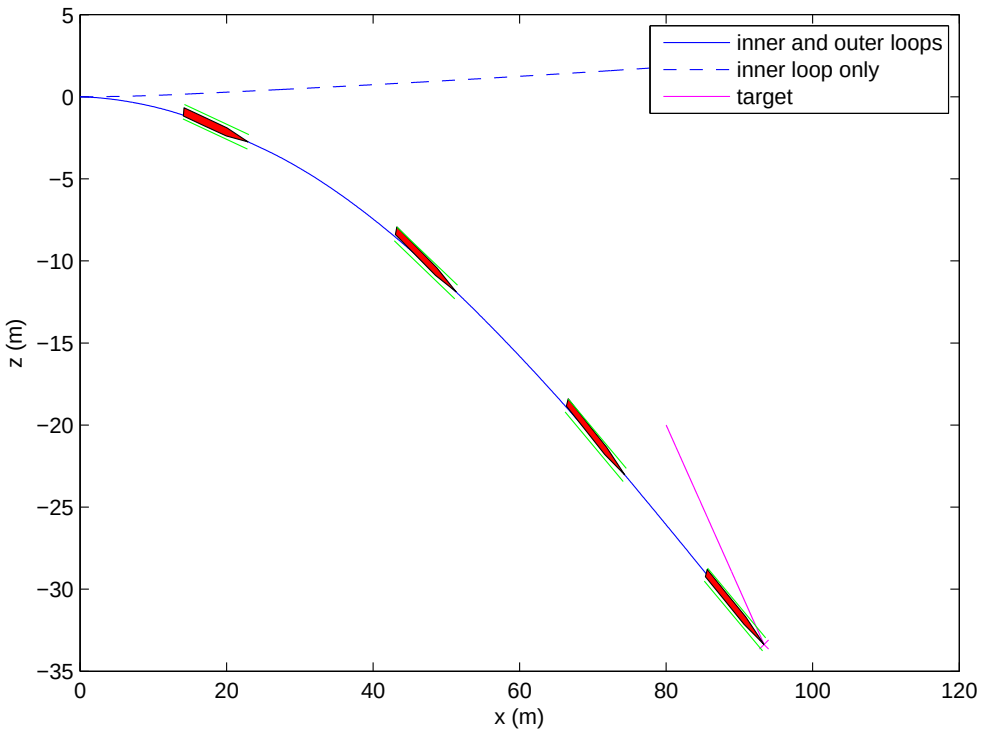

Figure 5.21: Trajectory for $(x_f, z_f) = (80 + 10T, -20 - 10T)$ m with modified feedback control according to Eq. (5.9), $k_{inner} = -0.7$, and $s = 14$.

reduced, but larger tolerances on the end condition were required.

Incorporating aggressive maneuvering with the non-cylindrical models becomes more difficult. Several attempts at solving the single obstacle case (similar to the cylindrical case shown in Figure 5.17) yielded no feasible solutions. One example where the constrained optimizer failed to find a feasible solution is shown in Figure 5.23. Although both cylindrical and non-cylindrical models produced similar bifurcation behavior; however, the parameter values at which the bifurcations occur are different, which may lead to significantly different maneuvering capabilities when

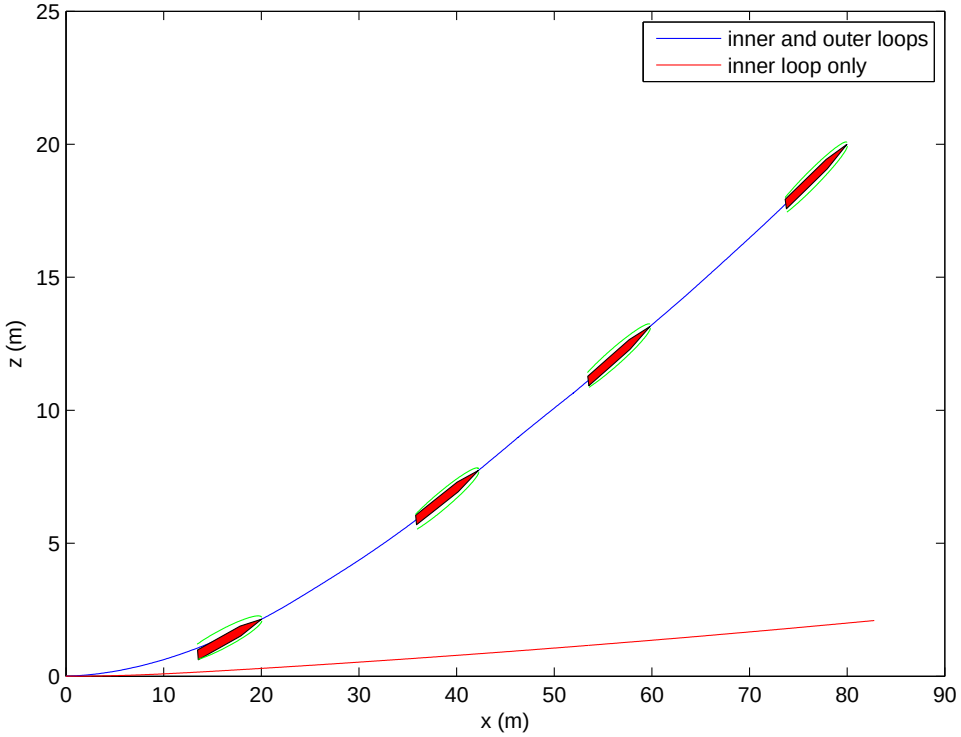

Figure 5.22: Non-cylindrical planing with splined cavity model, trajectory for $(x_f, z_f) = (80.0m, -20.0m)$ with feedback control according to Eq. (5.9), $\sigma = 0.0335$, $k_{inner} = -0.9$, and $s = 14$.

run at similar parameter values.

5.3.1 Optimization using Penalty Methods and Simple Search Algorithms

In order to investigate the maneuvering capability difference between the non-cylindrical and cylindrical models, maximum turn maneuvers are considered. A maneuver that maximizes (or minimizes) θ_f over a set time T, originating from

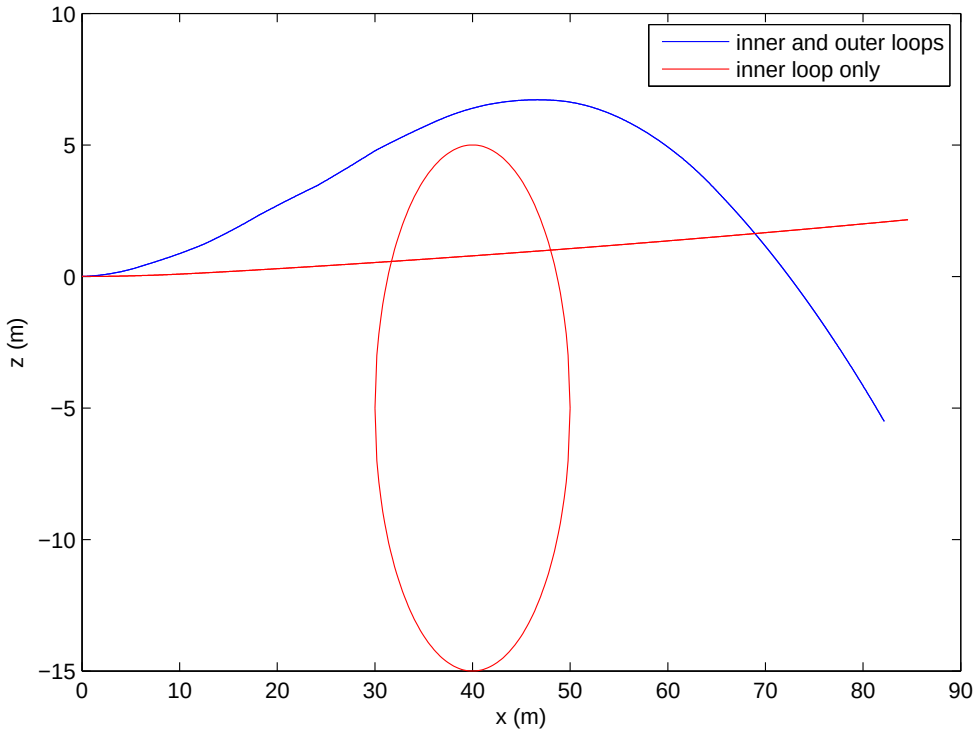

Figure 5.23: Non-cylindrical planing with splined cavity model; failed run for $(z_f, x_f) = (-20.0m, 80.0m)$, obstacle at $(z_{obst}, x_{obst}) = (-5.0m, 40.0m)$, and $r_{obst} = 10.0\ m$.

some initial condition (such as $(z_0, x_0, w_0, q_0) = (0.0m, 0.0m, 0.0m/s, 0.0rad/s)$) can be considered. The built in Matlab function *fmincon* is capable of solving this type of maneuver for the cylindrical case; however, this direct constrained approach has difficulty improving upon initial guesses for the non-cylindrical models. For the non-cylindrical planing system, the maneuver was solved by using a non-gradient based optimization algorithm with the function *fminsearch*. Although these types of maneuvers are only considering one specific capability measure, the differences between the results for the non-cylindrical and cylindrical models were not significant.

This finding may mean that the incapability of the constrained optimizer to find a feasible solution for the single obstacle maneuver with non-cylindrical planing, may be more related to the complexity of the feasible domain rather then the incapability of the vehicle to maneuver.

The family of control inputs that generate trajectories that satisfy the maneuver conditions define the feasible domain, and this domain may include unconnected sets. Optimizing in this domain can be difficult and the complexity of the feasible domain increases as the dynamics get complex. The direct constrained optimization can instead be replaced by a penalty type objective function. Here, the constraints, rather then being directly enforced, are treated as penalties on the objective function in an unconstrained optimization scheme. The optimizer progresses simultaneously towards feasible and optimal solutions.

For the example of the supercavitating vehicle system, the objective function can be re-written as Eq. (5.11). The values c_i represent the inequality constraints (as used for the bounds on the states and control), and the values ceq_j represent the equality constraints (as used for the end condition for the maneuver). For the supercavitating vehicle system, the penalty multipliers, P_{ineq} and P_{eq} are positive, and these multipliers multiply all equality constraints by the same factor, and all inequality constraints by the same factor; in the general case, these may be non-linear and can be independent for each constraint.

$$F(u_1, u_2, \ldots, u_s, T) = T + P_{ineq} \sum_{c_i > 0} |c_i| + P_{eq} \sum_{j} |ceq_j| \tag{5.11}$$

Coupled to the penalty method is an unconstrained optimizer. Simple search algorithms worked best for these complicated systems, with the simplest built in Matlab function *patternsearch* providing the best results in the fastest time. This observation is not surprising, since the gradient based methods can be expected to face difficulties due to the non-smooth dynamics, and the overall complexity of the optimization function. Additionally, these gradients are not readily available due to the numeric nature of the dynamics integration and the cavity (planing force) calculations. Overall, all algorithms using the penalty method provided better improvement on initial guesses then the constrained approach with *fmincon*.

By using the penalty approach, the obstacle scenarios similar to the cylindrical case shown in Figure 5.17, can be considered for the non-cylindrical case. The maneuver consisted of an end condition of $(z_f, x_f) = (-20.0m, 80.0m)$ with an obstacle centered at $(z_{obst}, x_{obst}) = (-5.0m, 40.0m)$. Medium radius obstacles are solved initially, and these solutions are used to seed optimization runs for progressively larger radius obstacles until no feasible solution could be found. A feasible solution for the non-cylindrical single obstacle case is shown in Figure 5.24 for an obstacle radius $r_{obst} = 7.0\ m$. In this plot, the vehicle and cavity orientation plots are exaggerated in size. When compared to the cylindrical case, the non-cylindrical case was also found to be capable of maneuvering around similarly sized obstacles.

The Matlab code for carrying out the optimal control with the non-cylindrical planing model is presented in Appendix B. This is included to demonstrate the general method for how the optimization using *patternsearch* with the penalty method is coded, along with the specific code for the non-cylindrical planing dynamics.

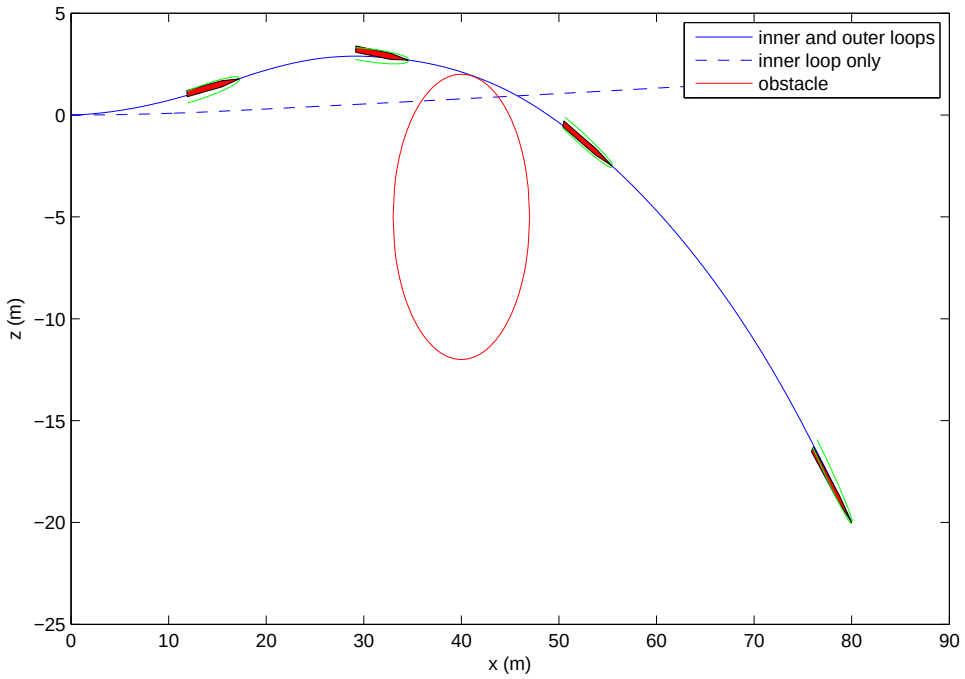

Figure 5.24: Non-cylindrical planing model, run for $(z_f, x_f) = (-20.0m, 80.0m)$, obstacle at $(z_{obst}, x_{obst}) = (-5.0m, 40.0m)$, and $r_{obst} = 7.0\ m$.

5.3.2 Bootstrapping Techniques Using Simple Integration

The use of simple integration schemes and bootstrapping techniques are common for numeric optimal control solutions. Simple integration schemes, such as midpoint integration shown in Eq. (5.12), help speed up the integration of the dynamics, which in turn dramatically increases the speed of the optimization. Bootstrapping is based on building solutions from previous solutions. A common approach for solving a complicated optimal control problem is to first solve the maneuver by using a coarse discretization using a simple integration scheme. Since the discretization is coarse, and the integration method is simple, this initial problem is not difficult

to solve. This solution can then be applied to a finer discretization and solved again. This can be carried out for several iterations, and as the time discretization becomes finer, the solution becomes better, and the integration becomes more accurate. Although the optimizer has to solve a series of progressively more complicated problems, it is given a series of progressively better starting guesses.

$$x_{i+1} - x_i = \int_{t_i}^{t_{i+1}} f(t, x(t))dt \approx f(\frac{t_i + t_{i+1}}{2}, \frac{x_i + x_{i+1}}{2})(t_{i+1} - t_i) \tag{5.12}$$

This technique has been applied to supercavitating vehicle systems before [39, 1]; however, the solutions for the maneuvers considered are all within the cavity. For the maneuvering studies in this work, and the parameter values and speeds considered, planing or cavity contact is abundant during maneuvering (operation in ranges where unstable and limit-cycle behavior is observed with the uncontrolled and feedback controlled systems). Bootstrapping schemes and mid-point integration were attempted for both the set end time and floating end time maneuvers. The system dynamics for non-smooth systems can very greatly depending on the region of operation. The supercavitating system is an example of this; when planing, the system dynamics are dramatically different, with much higher forces present. Since planing is prevalent, mid-point integration for any coarse discretization becomes highly inaccurate. Feasible solutions for coarse discretizations where planing is present become extremely difficult to resolve. Even when feasible solutions can be solved, the dynamics are so dependent on the region of operation that different solutions "bootstrapped" to finer discretizations are not necessarily feasible, let

alone good seeds. Because of this, for the supercavitating vehicle systems, direct integration methods are required for accuracy. This of course, comes at the expense of lengthy computational time for the optimization process.

5.4 Maneuvering for Delayed Model without Steady Planing Assumption

The penalty approach was also applied to the delayed model presented in the previous chapter. This model includes the forces due to the motion of the body, instead of the use of the steady planing assumption. Due to the delay, the equations of motion must be integrated by using a delay differential equation (DDE) solver that requires the state history along with an initial condition. In the previous examples, the equations of motion are integrated over each individual section of piecewise constant control. This becomes difficult to implement with the DDE solver, since each individual section will require a state history.

To get around this difficulty, a smooth control scheme is implemented by using a splined interpretation. In this formulation, the optimization variables become inputs to a spline interpolation that is used as the control input function; the optimization variables in this case can be though of as parameters in a describing function that defines the controller input. Now, the control input function for the duration of the maneuver is known completely within the integration function. An additional advantage in this approach is that, the controller input is now a continuous and differentiable function which is practical to implement. Additionally,

control contributions to the system dynamics will be less abrupt. It should be noted that the previous systems can be also solved in a similar manner, but in these cases, the piecewise-constant control is sufficient to demonstrate results.

Results for a move-to-point maneuver to $(z_f, x_f) = (-20.0m, 80.0m)$ and the delayed model with non-steady planing are shown in Figure 5.25. The smooth outer-loop control inputs are shown in Figure 5.26. Obstacle avoidance maneuvers are then considered starting with maneuvers with small obstacles and progressing to larger obstacles until no feasible solutions can be found. The ending largest feasible obstacle radius of $r_{obst} = 5.0\ m$ for a maneuver to $(z_f, x_f) = (-20.0m, 80.0m)$ with the obstacle centered at $(z_{obst}, x_{obst}) = (-5.0m, 40.0m)$ is a smaller radius obstacle as compared to similar runs for the cylindrical and non-cylindrical models with steady planing and without time delay. The best solved trajectory is shown in Figure 5.27. Here, it can be seen that the trajectory moves under the obstacle (in terms of positive z), as opposed to over as with the steady planing, non-delayed cylindrical and non-cylindrical models.

The influence of the initial guess on the ending solution can be seen by considering a larger obstacle (infeasible ending trajectory). A run using the best discovered trajectory at $r_{obst} = 5.0\ m$ as an initial guess for the optimization to do a maneuver with an obstacle radius $r_{obst} = 6.0\ m$ is shown in Figure 5.28. Here, the optimization scheme considers trajectories under (with respect to positive z) the obstacle, which is the case for the trajectory that seeded the optimization. If instead zero outer-loop control input is used as the initial guess, the optimization considers trajectories over the obstacle (see Figure 5.29). Although the results of either seeding in this case

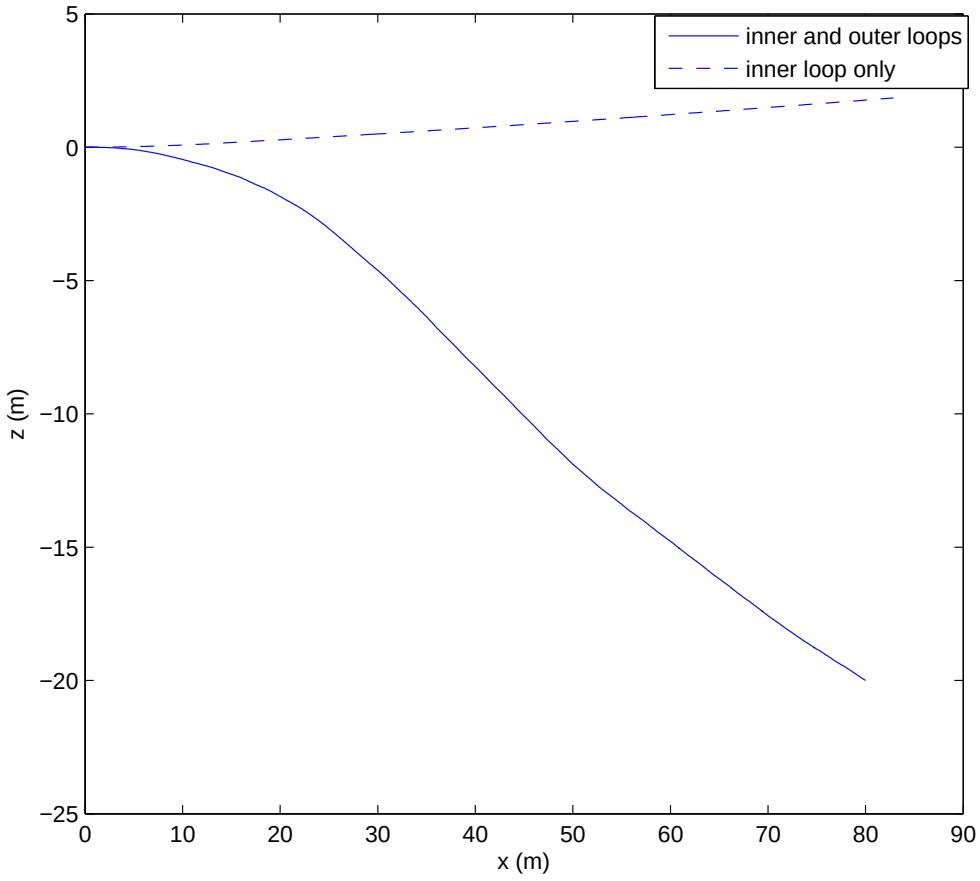

Figure 5.25: Delayed model without steady planing assumption and run to $(z_f, x_f) = (-20.0m, 80.0m)$.

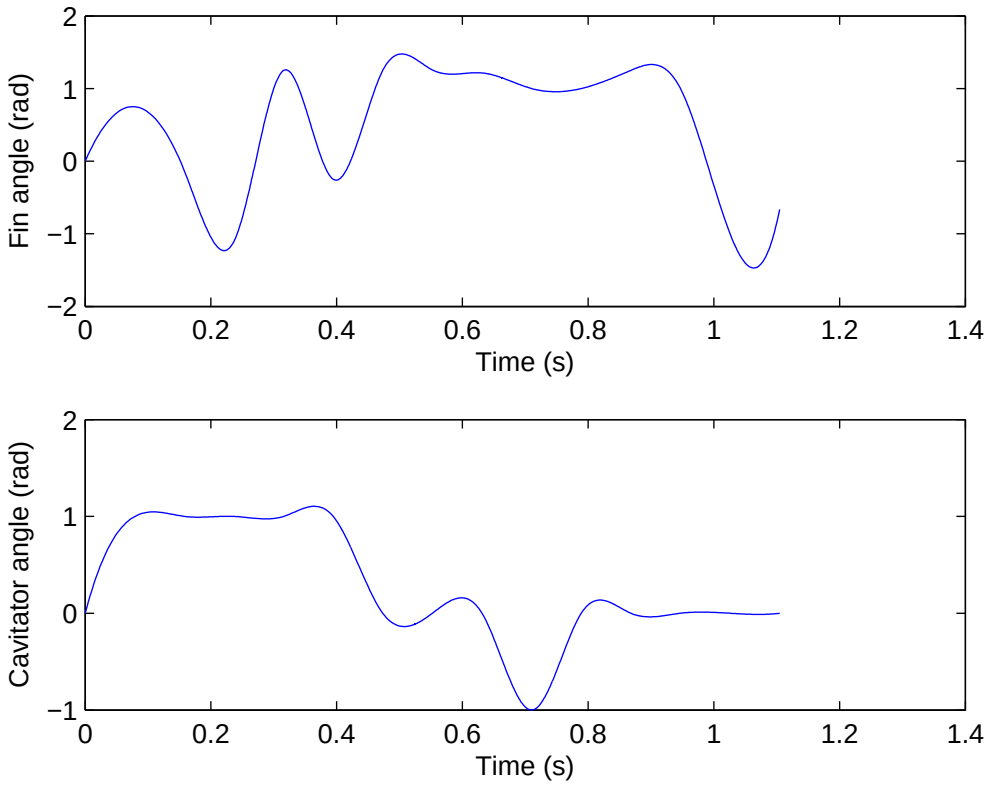

Figure 5.26: Outer-loop control inputs for delayed model without steady planing assumption and run to $(z_f, x_f) = (-20.0m, 80.0m)$.

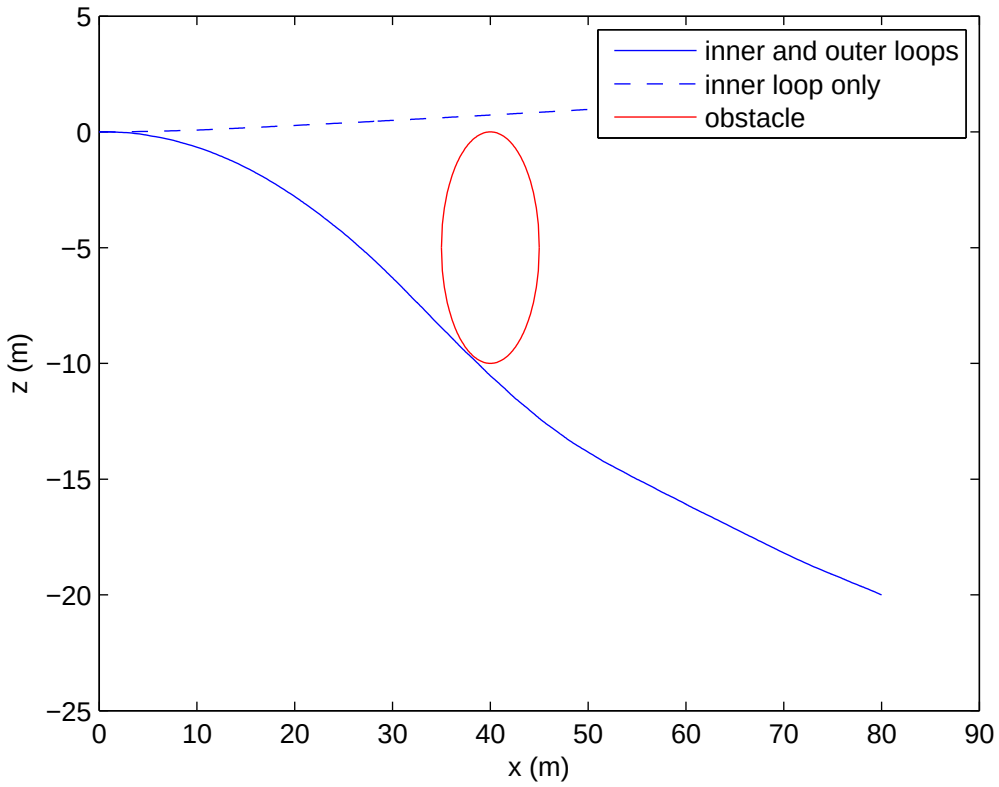

Figure 5.27: Delayed model without steady planing assumption, run for $(z_f, x_f) = (-20.0m, 80.0m)$, obstacle at $(z_{obst}, x_{obst}) = (-5.0m, 40.0m)$, and $r_{obst} = 5.0\ m$.

are infeasible, the difference in the types of trajectories considered demonstrate the influence of the initial guess.

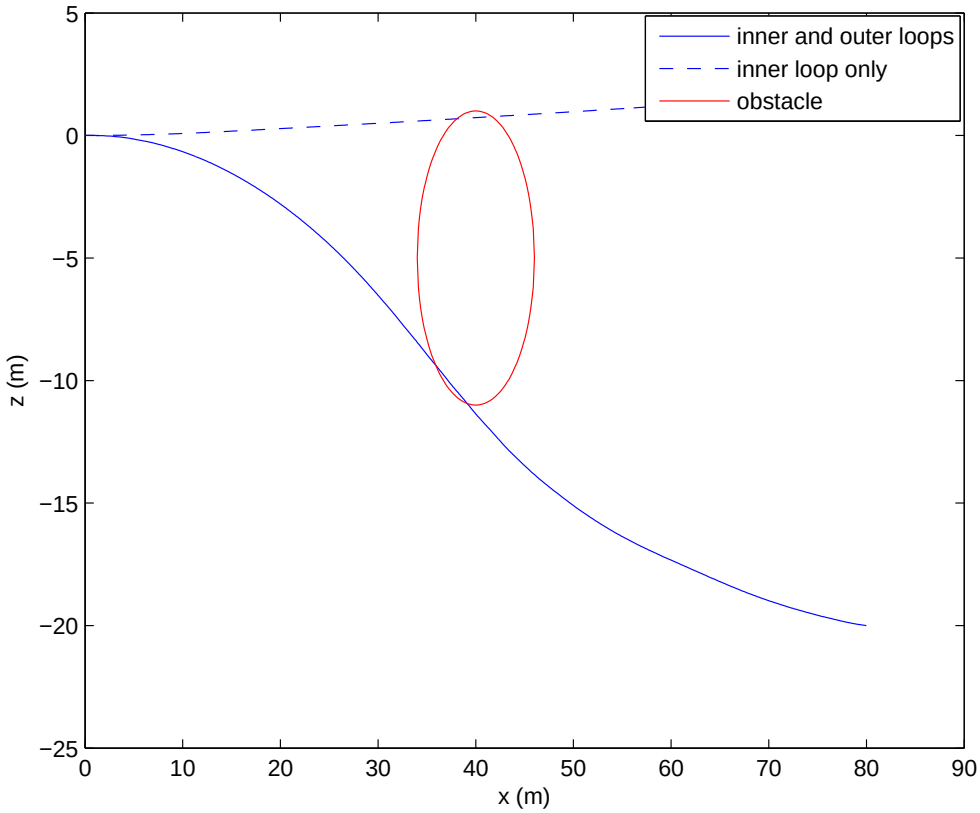

Figure 5.28: Delayed model without steady planing assumption, run for $(z_f, x_f) = (-20.0m, 80.0m)$, obstacle at $(z_{obst}, x_{obst}) = (-5.0m, 40.0m)$, and $r_{obst} = 6.0\ m$. The best found control input solved for a smaller obstacle run is used as an initial guess. Infeasible ending trajectory.

The Matlab code for carrying out the optimal control with the delayed model is presented in Appendix B. This is included to demonstrate the general method for how the optimization using the smooth inputs is coded, along with the specific code

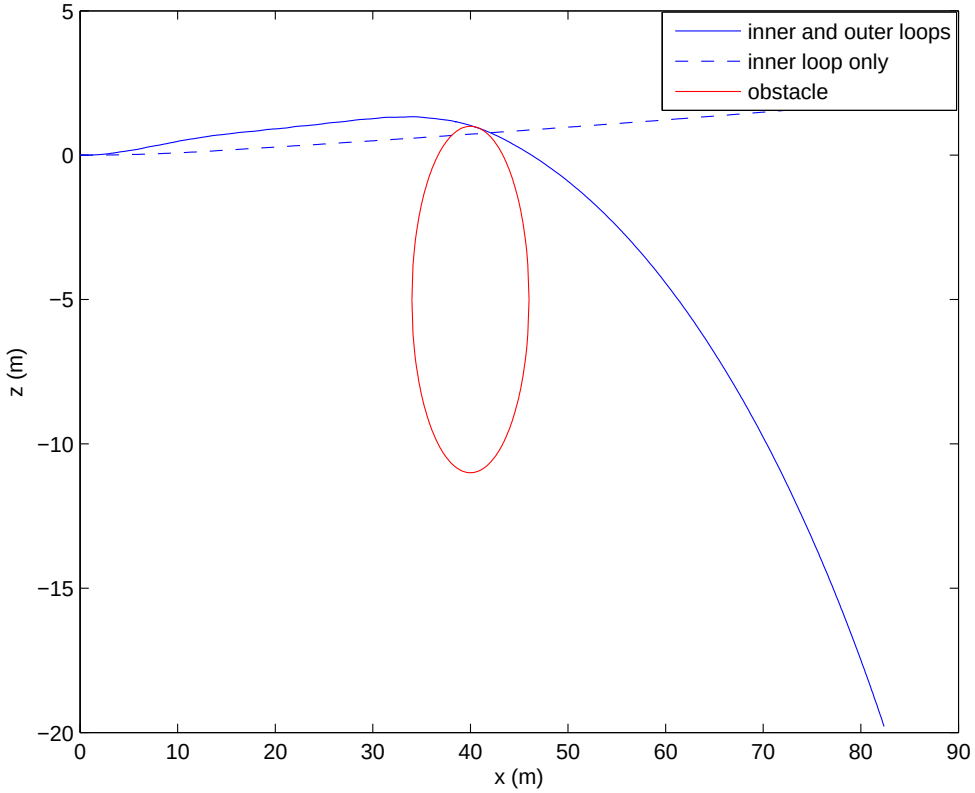

Figure 5.29: Delayed model without steady planing assumption, run for $(z_f, x_f) = (-20.0m, 80.0m)$, obstacle at $(z_{obst}, x_{obst}) = (-5.0m, 40.0m)$, and $r_{obst} = 6.0\ m$. Trivial outer-loop control is used as an initial guess. Infeasible ending trajectory.

for the impacting and delayed dynamics.

5.5 Maneuvering with Six DOF Model

The optimal control solution method is also applied to a six degree-of-freedom model. The model is used to consider more general flight motions in three dimensions, and the details are presented in Appendix A. This model does not include small angle assumptions for the vehicle motions, although there are assumptions for the forces generated by the control elements. Initially, only dive-plane maneuvers are considered to test the approach. When considering a fixed end time maneuver, the system was found to suffer from several local minima. By using a constrained optimizer, it was found that for a maximum angle dive or climb maneuvers (maximizing or minimizing θ_f), the optimization would not progress far from an initial guesses before becoming stuck in a local minimum. More difficult maneuvers such as move to point were difficult to solve, even when given a near feasible starting guess. Again, a penalty method based on the pattern search algorithm was applied instead and was found to worked well. A solution for a move to point maneuver with $(z_f, x_f, y_f) = (-50.0m, 120.0m, 0.0m)$ is shown in Figure 5.30. Feedback control of the form shown in Eq. (5.9) is utilized to stabilize vehicle motions in the vertical plane, with $k_{inner} = 0.7$. The vehicle parameters remained consistent with the previous simulations with $g = 9.81\ m/s^2$, $m = 22.7005\ kg$, $R_n = 0.0191\ m$, $R = 0.0508\ m$, $L = 1.8\ m$, and $C_{x0} = 0.82$. The propulsive force is set as constant, with $F_{prop} = 2200\ N$. The initial conditions are for a straight and level flight with

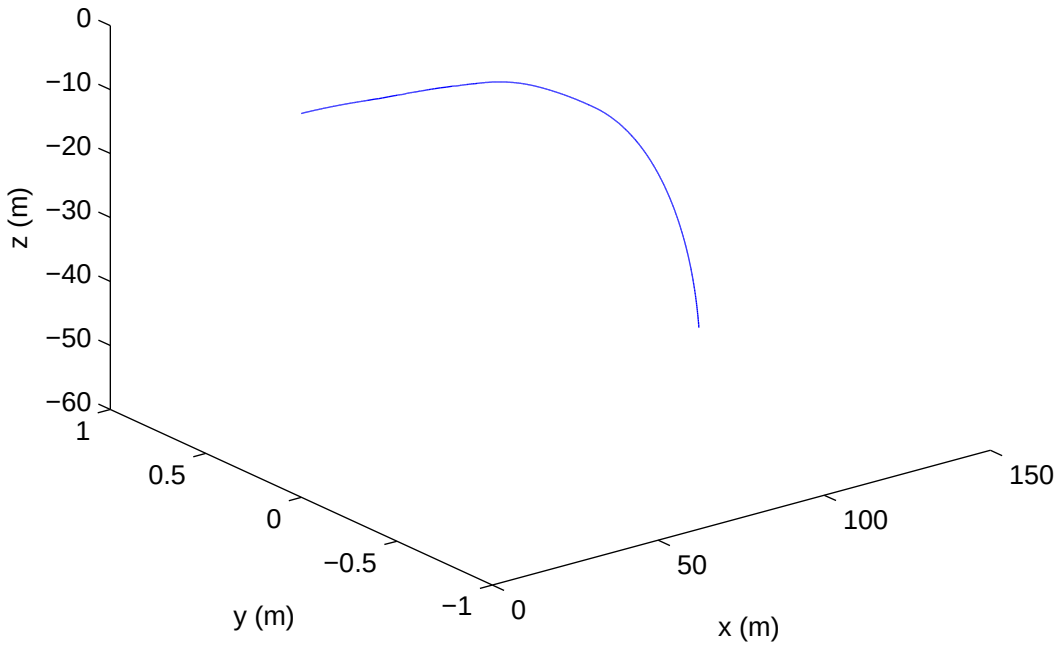

Figure 5.30: Six degree-of-freedom model, run for $(z_f, x_f, y_f) = (-50m, 120m, 0m)$.

a forward velocity of $u = 75\ m/s$.

With the six degree-of-freedom model, motions outside of the vertical plane can also be considered. To allow for motion in the horizontal plane, the optimizer is allowed three control inputs, the cavitator actuation angle, the elevator actuation angle, and the rudder actuation angle. Both elevators and both rudders are assumed to move together with the same actuation angle. A move-to-point maneuver for $(z_f, x_f, y_f) = (-50.0m, 120.0m, 5.0m)$ is shown in Figure 5.31. The resulting best solution, is not as expected with an abrupt maneuver in the horizontal plane only within the last time segment of the optimization discretization. This observation

is confirmed by looking at the resulting control input, shown in Figure 5.32, where the rudder input is only applied during the last time segment. The result can be traced to the fact that the inner-loop controller is only stabilizing planing motions in the vertical plane. This is in part due to the orientation of the cavitator actuation angle that is set to be vertical (with respect to the body orientation). With this, the cavitator angle control actuation of an un-rolled vehicle cannot be expected to produce contributions in the horizontal plane. The vehicle motions in the horizontal plane are in fact quite unstable, with significant planing forces being generated during the quick motion at the end of the maneuver, which is required to achieve desired horizontal displacement. If the vehicle were to generate horizontal motions early in the maneuver, the high planing forces and instabilities would greatly reduce the ability of the vehicle to reach the desired end point.

The maneuvering studies for the six degree-of-freedom model are very preliminary. More work needs to be done such as allowing greater control authority over vehicle roll, by giving independent control over each set of rudders and elevators. Better control of vehicle roll may allow for inner-loop feedback stabilization in multiple planes with a single axis cavitator. Additionally, a two axis cavitator could also be considered, with separate feedback control along each direction.

5.6 Discussion

Maneuvering of non-smooth vehicle systems is considered in this chapter with the primary example of supercavitating vehicle systems. Maneuvers were solved for

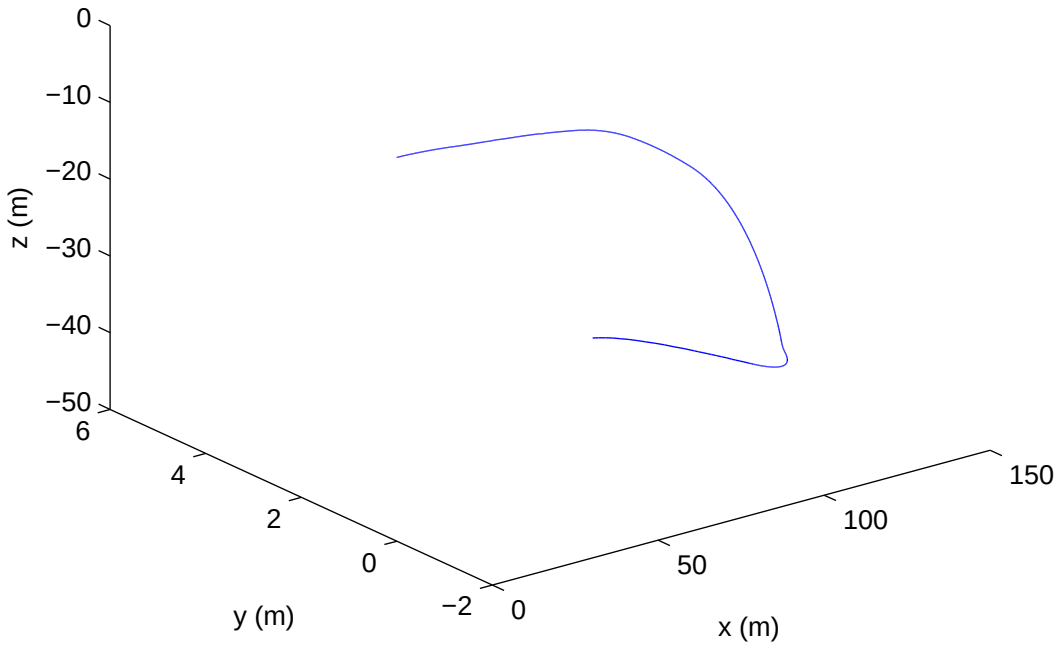

Figure 5.31: Six degree-of-freedom model, run for $(z_f, x_f, y_f) = (-50.0m, 120.0m, 5.0m)$.

the cylindrical, non-cylindrical, six degree-of-freedom, and the delayed non-steady planing models described in the previous chapters.

In this work, the speeds and parameter values for the maneuvers considered for the supercavitating vehicle systems are within the range where unstable as well as limit-cycle behavior exists in the un-controlled and feedback systems. Within these parameter ranges, the non-smoothness of the planing must be addressed in the optimal control solution procedure, and planing is apparent in the best calculated maneuvers. As such, the need for an inner-loop feedback controller is required.

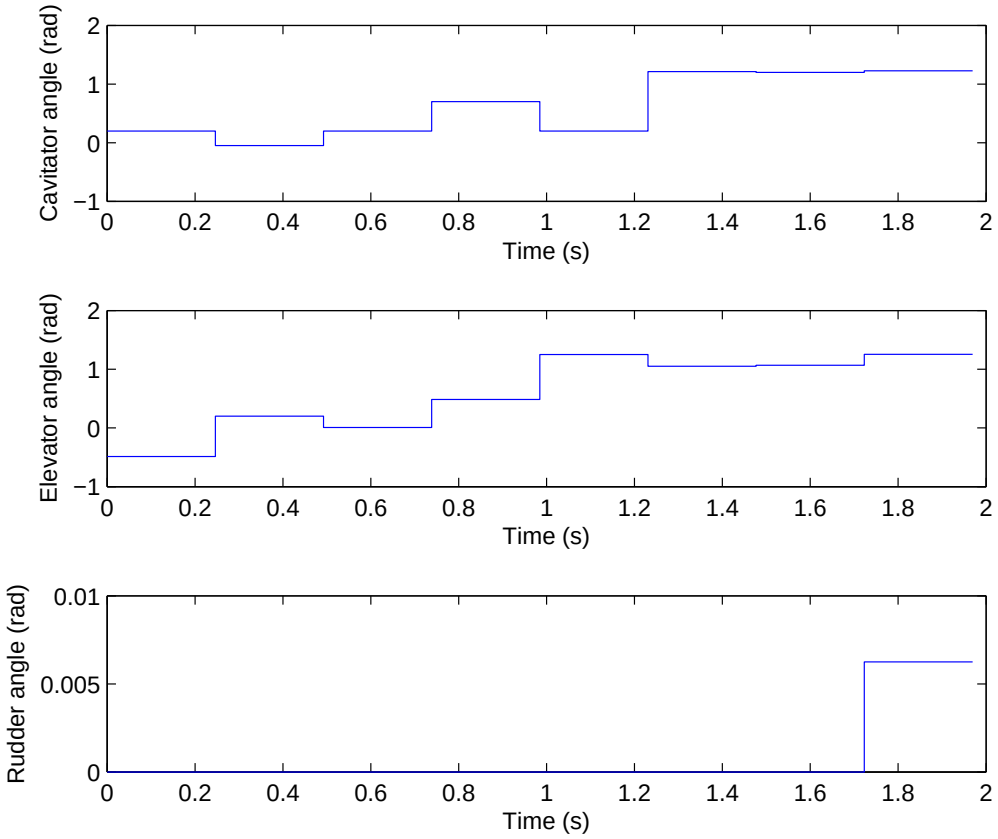

Figure 5.32: Outer-loop control inputs for six degree-of-freedom model, run for $(z_f, x_f, y_f) = (-50.0m, 120.0m, 5.0m)$.

This fast acting stabilizing inner-loop controller is used in conjunction with a coarser outer-loop control that guides the vehicle through the desired maneuver. Additionally, since the vehicle moves across regions with dramatically different dynamics, simple integration techniques with coarse time discretizations do not accurately estimate vehicle motions. Therefore methods of bootstrapping (in terms of using simple integration techniques and moving from coarse to finer time discretizations) are not viable for solving maneuvers for these types of systems.

For systems with complicated dynamics, constrained optimizers can face difficulties searching for feasible optimal solutions. Penalty methods open up the feasible domain and allow for simultaneous progression towards better and more feasible solutions. The penalty approach combined with a simple unconstrained search algorithms (such as *patternsearch*) where shown to provide a means to solve difficult maneuvers for systems with complicated non-smooth dynamics (where the constrained optimizers failed). Seeding algorithms such as those for solving progressively more aggressive maneuvers (iterating towards larger obstacles) using previous solutions as initial guesses can help to speed up the optimization process. However, the influence of the initial guess must also be considered when using these approaches, as they may limit the types of trajectories considered. It may be beneficial to use different initial guesses once the iterations terminate with infeasible solutions.

Chapter 6

Summary and Recommendations for Future Work

6.1 Summary

This dissertation work is centered around supercavitating vehicle systems with "soft" non-smooth interactions between the cavities surrounding the vehicles and the vehicles. Here, the modeled cavity interactions generate a system that is characterized by non-constant switching boundaries and non-constant switched dynamics. Since, the vehicle motions vary greatly depending on the region of interaction, this creates a very complex system given that the boundaries, and the forces within each region, are state and control dependent.

Much of the above mentioned complexity is due to the inclusion of realistic physical effects such as the planing associated with shifted non-cylindrical cavities, an aspect unique to this dissertation work. By using these shifted non-cylindrical cavities, similar qualitative changes were found as in previous supercavitating vehicle studies. Similar stabilization techniques were also successful for inclusion in the systems considered here. However, the values of equilibrium solutions and the parameter values at which qualitative changes experienced by them occur, differ for the non-cylindrical cavity case. Hence, the inherent vehicle motions when including these effects can be distinctly different.

Additional observations have been made by generating a preliminary vehicle

motion model for partially cavitating vehicles. This model is meant to be the first step towards modeling full vehicle missions that include cavity growth and collapse. For small cavities, it has been found that the planing is insufficient to support the rear of the vehicle. Furthermore, the use of passive fin input which supports the vehicle for the supercavitating case, is not necessarily capable of rejecting transient motions that move the vehicle away from a straight and level flight. Linear fin feedback is shown to work well in conjunction with the linear cavitator feedback, and active fin inputs may be necessary for sustaining partial cavity flight.

A full representation of the derivation of the immersion depth, and immersion rate terms used in the planing force calculation have also been given in this work. These terms have been presented in a somewhat arbitrary manner in much of the previous research. This full derivation provides a basis for properly accounting for the effects of vehicle motions and body velocities into the cavity, creating damping-like contributions in the planing force formulation. This is a departure from the previous steady planing assumption based studies, which form a vast majority of the previous literature; in them, one only considers planing forces due to the relative vehicle-cavity positions. The complete representation of the immersion terms also allows for a proper handling of the cavity time-delay effect (in this case for cylindrical cavities). In this work, the delay is found to have a stabilizing effect for particular values of cavitation numbers.

A combined inner-loop and outer-loop control scheme is applied with success for the maneuvering studies. Here, fast acting instabilities are rejected by a feedback inner-loop while a numeric optimal control derived outer-loop guides the

vehicle through a desired maneuver. For complicated supercavitating vehicle system maneuvers, the best results are provided by utilizing a penalty method (to account for the constraints) along with a simple unconstrained search algorithm. This is due to the highly complicated feasible domain generated by dynamic constraints. Direct integration techniques, rather then boot-strapping techniques are required, since the system dynamics differed greatly depending on operating conditions. Maneuvers are generated for cylindrical, shifted non-cylindrical, six degree-of-freedom systems, and impacting models. All maneuvers have been performed at speeds where there were tight cavity-body clearances, and planing is dominant during the motion. Much of this work can be extended for use with other non-smooth systems.

6.2 Recommendations for Future Work

There are many direct extensions possible from this body of work. Full mission simulation by using the partial cavitation model is still an open avenue. The main limitation for this line of work is the availability of accurate partial cavitation models, which in particular should include non-steady cavity growth and collapse. The numeric optimal control approach outlined for maneuvering should work well for developing optimal outer-loop commands for these full mission simulations. The six degree-of-freedom model is also another direction for expansion. Out of plane maneuvers with multiple axis cavitator actuation can be considered. The non-cylindrical cavities accounting for delay affects have also not been considered. This may greatly complicate the computation, since multiple delays accounting for cav-

ity positions all along the planing area must be tracked. Additional physical effects such as gravity effects on the cavity should also be considered, since as shown, the cavity shape can play a significant role in determining the system dynamics. The approach used to determine the non-cylindrical planing forces in this work is generalizable to other cavity models that are to account for realistic physical effects. Actuator dynamics, specifically actuator rate limitations, has not been included in this work, but can be incorporated into the numeric optimal control approach. The maneuvering studies can also be extended to a broad range of non-smooth vehicle systems, including hypersonic flight vehicles.

Appendix A

Six Degree-of-Freedom Model

A six degree-of-freedom (DOF) model is generated to consider general flight dynamics modeling. In this model, all small angle assumptions related to the dynamics are removed, and the vehicle speed is no longer considered to be constant. For supercavitating vehicle systems, as with many flight systems, the force definitions, position vectors, and control surface rotations are conveniently described in local coordinate systems. An Euler angle approach is utilized to track several coordinate systems and their relationships to an inertial reference frame. This approach closely mimics the one used in previous literature [13].

A.1 General Approach

An inertial reference system with made up of unit vectors $< \hat{e_1}, \hat{e_2}, \hat{e_3} >$ is defined. A moving reference frame that is attached to the body CG and aligned along the body is defined with unit vectors $< \hat{b_1}, \hat{b_2}, \hat{b_3} >$, as shown in Figure A.1. By using the body coordinate system, the locations to the control surfaces are simply defined. Additionally, the vectors defining the forces and moments can easily be resolved and applied within this reference system (similar to the moving coordinate system in the dive-plane model).

The Euler angle relationships between the differing coordinate systems used

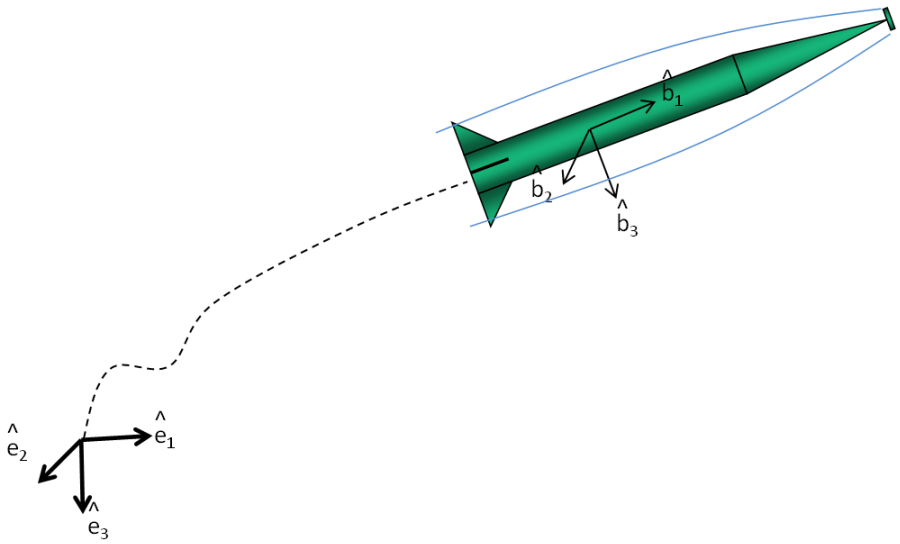

Figure A.1: Diagram of inertial and body reference frames.

in this work follow the ZYX convention. An example of transforming from the inertial frame $< \hat{e_1}, \hat{e_2}, \hat{e_3} >$, to the body frame $< \hat{b_1}, \hat{b_2}, \hat{b_3} >$, is shown in Figure A.2. The first rotation is about $\hat{e_3}$ axis with angle Ψ, generating the intermediate frame $< \hat{e_1}', \hat{e_2}', \hat{e_3}' >$. The second rotation is about $\hat{b_2}'$ with angle Θ, generating the intermediate frame $< \hat{e_1}'', \hat{e_2}'', \hat{e_3}'' >$. The final rotation is about $\hat{e_1}''$ with angle Φ, to the body fixed frame. The rotation matrix $[R_{e \to b}]$ that defines the transformation from the inertial to body reference frame can then be expressed as a chain of rotation matrixes as shown in Eq. (A.1).

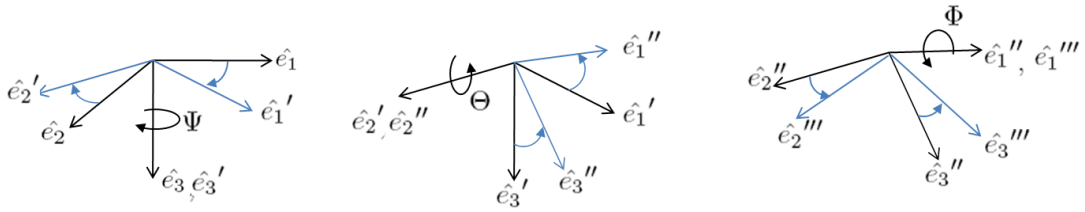

Figure A.2: ZYX rotation order used for Euler angle relationships.

$$\begin{Bmatrix} \hat{b_1} \\ \hat{b_2} \\ \hat{b_3} \end{Bmatrix} = \begin{bmatrix} 1 & 0 & 0 \\ 0 & cos\Phi & sin\Phi \\ 0 & -sin\Phi & cos\Phi \end{bmatrix} \begin{bmatrix} cos\Theta & 0 & -sin\Theta \\ 0 & 1 & 0 \\ sin\Theta & 0 & cos\Theta \end{bmatrix} \begin{bmatrix} cos\Psi & sin\Psi & 0 \\ -sin\Psi & cos\Psi & 0 \\ 0 & 0 & 1 \end{bmatrix} \begin{Bmatrix} \hat{e_1} \\ \hat{e_2} \\ \hat{e_3} \end{Bmatrix}$$
$$= [R_{e \to b}] \begin{Bmatrix} \hat{e_1} \\ \hat{e_2} \\ \hat{e_3} \end{Bmatrix} \tag{A.1}$$

The cavitator reference frame is one that follows the orientation of the cavitator as shown in Figure A.3. The cavitator is constrained to only one control actuation angle δ_c about the $\hat{b_2}$ or $\hat{c_2}$, axis. So the cavitator reference frame can be described by a single rotation from the body reference frame as shown in Eq. (A.2).

$$\begin{Bmatrix} \hat{c_1} \\ \hat{c_2} \\ \hat{c_3} \end{Bmatrix} = \begin{bmatrix} cos\delta_c & 0 & -sin\delta_c \\ 0 & 1 & 0 \\ sin\delta_c & 0 & cos\delta_c \end{bmatrix} \begin{Bmatrix} \hat{b_1} \\ \hat{b_2} \\ \hat{b_3} \end{Bmatrix} \tag{A.2}$$

The fin reference frames can be represented as shown in Figure A.4. For each fin, $\hat{f}_1$ is oriented forward along the fin, and $\hat{f}_2$ extends out along the fin axis. Two

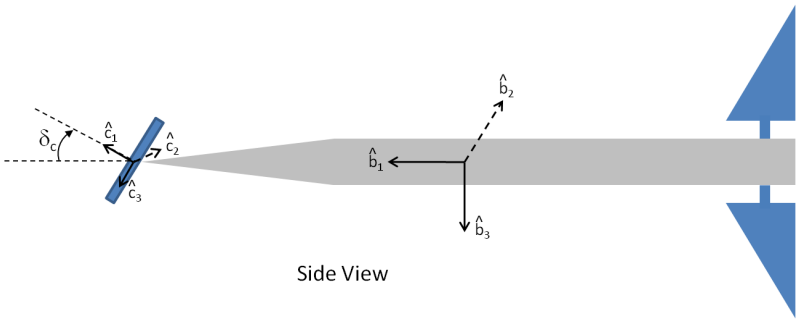

Figure A.3: Diagram of cavitator reference frame.

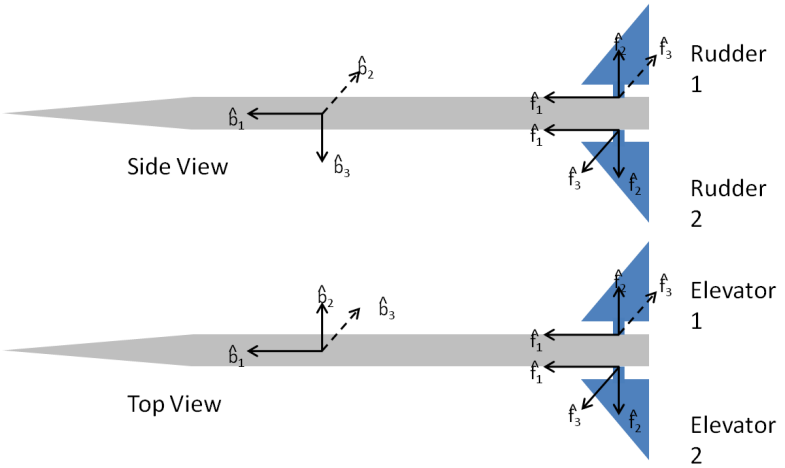

Figure A.4: Diagram of fin reference frames.

successive rotations define the fin reference frame, first, a sweepback angle rotation about the positive $\hat{f}_3$ axis, and a control angle δ_f rotation along the fin axis, $\hat{f}_2$. Each fin is associated with a unique transformation between the body and fin reference frames.

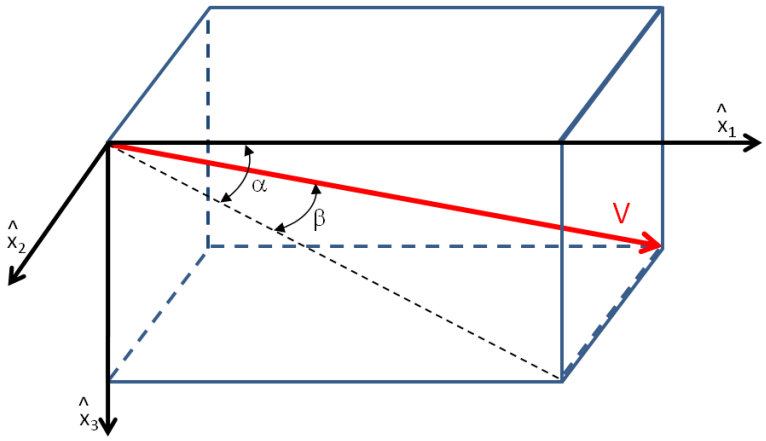

Figure A.5: Velocity direction shown with respect to a local coordinate system $< \hat{x_1}, \hat{x_2}, \hat{x_3} >$.

A.2 Fin Forces

The velocity at any point can be calculated by using rigid body kinematics. This velocity can then be expressed in any of the local reference frame basis by using the proper transformation matrixes. An example of a velocity vector shown with respect to some generic reference system, $< \hat{x_1}, \hat{x_2}, \hat{x_3} >$, is shown in Figure A.5. The velocity can be resolved in the local reference frame unit vecotrs as $\vec{V} = u\hat{x_1} + v\hat{x_1} + w\hat{x_1}$. The individual slip angles α and β can then be expressed according to Eqs. (A.3)-(A.4). Furthermore, a transformation from the local reference frame to a frame aligned along the velocity direction, can be described by two rotations about the slip angles α and β. The transformation matrix can be described by Eq. (A.5). The slip angles are important in determining the forces generated by the control surfaces.

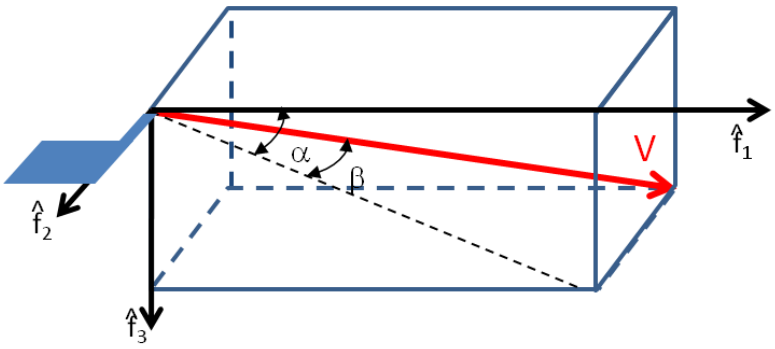

Figure A.6: Velocity direction at a fin.

$$tan(\alpha) = \frac{w}{u} \tag{A.3}$$

$$sin(\beta) = \frac{-v}{\|V\|} \tag{A.4}$$

$$\begin{Bmatrix} \hat{g_1} \\ \hat{g_2} \\ \hat{g_3} \end{Bmatrix} = \begin{bmatrix} C\alpha C\beta & -S\beta & S\alpha C\beta \\ C\alpha S\beta & C\beta & S\alpha S\beta \\ -S\alpha & 0 & C\alpha \end{bmatrix} \begin{Bmatrix} \hat{x_1} \\ \hat{x_2} \\ \hat{x_3} \end{Bmatrix} \tag{A.5}$$

The fin force is determined by using a simplified calculation. The fins are modeled as only generating lift and drag forces. A fin diagram and it's local velocity vector are shown in Figure A.6. The velocity at the fin can be calculated in the body reference frame according to Eq. (A.6), as the sum of the velocity due to the motion of the CG, along with the velocity due to rotation of the body ($\vec{r}_f^{\,b}$ represents the vector to the fin from the body CG in the body reference system). The velocity in the fin reference system can then be represented by a transformation as shown in Eq. (A.7).

$$\vec{V}_f^b = \vec{V}_{cg}^b + \vec{\omega}^b \times \vec{r}_f^b \tag{A.6}$$

$$\vec{V}_f^f = [R_{b\to f}]\vec{V}_f^b \tag{A.7}$$

From the expression for $\vec{V}_f^f$, the slip angles α and β can be calculated from Eqs. (A.3)-(A.4), and the rotation matrix $[R_{g\to f}]$ can be generated. The lift and drag forces are taken as only functions of the angle of attack α and they are defined according to Eqs. (A.8)-(A.9). The lift and drag forces for a control surface are generally defined with respect to the relative fluid velocity direction as shown in Figure A.7. Therefore the lift and drag forces can be directly represented in the velocity reference frame, and the overall force of the fin can be expressed according to Eq. (A.10), when transformed back into the body reference frame.

$$f_{drag} = \frac{1}{2}\rho\|V\|^2 c_d|\alpha| \tag{A.8}$$

$$f_{lift} = \frac{1}{2}\rho\|V\|^2 c_l\alpha \tag{A.9}$$

$$\vec{F}_{fin}^b = [R_{f\to b}][R_{g\to f}] \left\{ \begin{array}{c} -f_{drag} \\ 0 \\ -f_{lift} \end{array} \right\}^g \tag{A.10}$$

A.3 Cavitator Force

The cavitator force is calculated somewhat differently due to the cavitation. A diagram of the orientation of the lift and drag forces for the cavitator with respect to

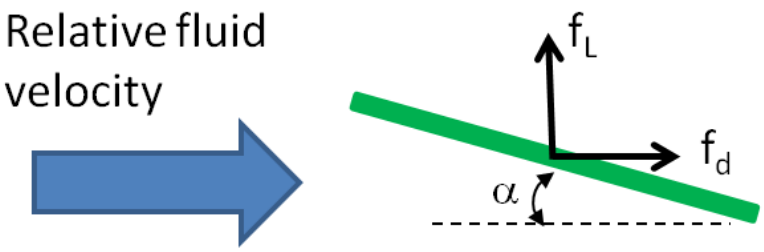

Figure A.7: Lift and drag forces on a control surface with respect to the relative fluid velocity direction.

the relative fluid velocity direction are shown in Figure A.8. Through experimental data, for a cavitating disc, it was found that the forces on the cavitator were predominantly due to pressure [18]. This means that the lift to drag ratio follows the relationship $f_l/f_d \approx tan(\alpha_c)$, or that the force is predominantly along the direction perpendicular to the wetted face of the cavitator. From experimental results, the coefficient of drag for flow along the axial direction of a disc cavitator is found to follow a relationship according to Eq. (A.11). So the overall cavitator force can be represented as given in Eq. (A.12), where $cos(\alpha_c) = \frac{u_c}{\|V_c\|}$. The cavitator force f_c is applied along the axial direction of the cavitator, so the vector representation of the cavitator force in the body reference system can is expressed as in Eq. (A.13).

$$C_d(\sigma, 0) = C_{D0}(1 + \sigma) \tag{A.11}$$

$$f_c = \frac{1}{2}\rho A_c \|V\|^2 c_d(\sigma, 0) cos(\alpha_c) \tag{A.12}$$

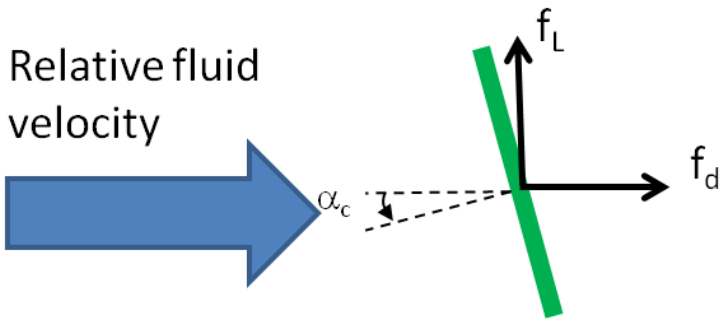

Figure A.8: Lift and drag forces for a cavitator with respect to the relative fluid velocity direction.

$$\vec{F}^{b}_{cav} = [R_{c\to b}] \left\{ \begin{array}{c} -f_c \\ 0 \\ 0 \end{array} \right\}^{c} \tag{A.13}$$

A.4 Cavity and Planing Force

Since various speeds are considered in the six DOF model, a closed form cavity model is utilized for faster generation of cavity shapes. A cylindrical cavity assumption (without cavity shift effects) is used for simplicity. The cavity shape is predicted by using a semi-empirical closed form solution formulated in reference [31]. As presented in Chapter 3, the cavity radius at a point along the cavity can be estimated by using Eq. (A.14). Here, again x represents the length from the cavitator, and d_c represents the cavitator diameter. An entire cavity profile can be generated by evaluating R_c at several points. Alternatively, as carried out here, an approximate cylindrical cavity can be generated by utilizing the cavity radius at $x = L$.

$$d_{max} = d_c\sqrt{0.82(1+\sigma)/\sigma}$$

$$l_m = d_c/2(1.92/\sigma - 3)$$

$$k_1 = 1.92(0.82(1+\sigma)/\sigma)^{-\frac{1}{2}}$$

$$k_2 = (x \cdot d_c - d_c)/l_m$$

$$R_c(x) = d_{max}/2\sqrt{1-(1-k_1^2)|1-k_2|^{2/.85}} \tag{A.14}$$

The planing formulations presented in the previous chapters are for planing in two dimensions. Since the body and cavity are both bodies of revolution, and both axes share a common point (the nose of the vehicle), the planing force can still be considered in two dimensions if an appropriate plane of planing is chosen. The plane of planing is the plane in which the vehicle immersion (when present) is symmetric, and hence, the two dimensional planing models are valid. This is the plane defined by the cavity and body axis (or the velocity direction and body axis). A diagram illustrative of this relationship is shown in Figure A.9. Here, the rotated planing frame $< \hat{p_1}, \hat{p_2}, \hat{p_3} >$ is defined with, $\hat{p_1} = \hat{b_1}$, $\hat{p_2} = \frac{\hat{p_1} \times \vec{V_c}}{\|\vec{V_c}\|}$, and $\hat{p_3} = \hat{p_1} \times \hat{p_2}$. The planing force is along the $\hat{p_3}$ direction with $\vec{F}_{plane} = f_p\hat{p_3}$, where f_p is the planing force calculated by using the cylinder-on-cylinder Paryshev formulation presented in Eq. (2.21).

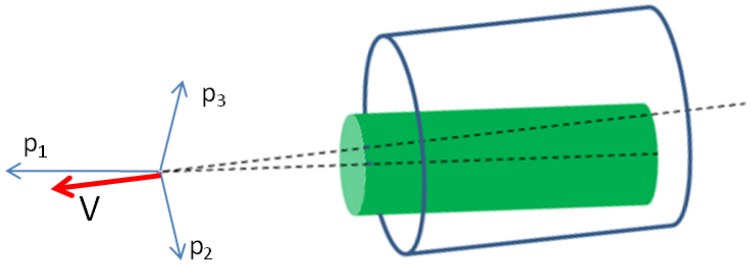

Figure A.9: Plane of planing defined by cavity axis (or velocity direction) and body axis.

A.5 Equations of Motion

The system has twelve states. The states considered are the body rotation angles $\begin{Bmatrix} \Psi \\ \Theta \\ \Phi \end{Bmatrix}$, the location of the CG $\begin{Bmatrix} x \\ y \\ z \end{Bmatrix}^e$, and the local velocities and rotation rates (in body reference system) $\begin{Bmatrix} u \\ v \\ w \end{Bmatrix}^b$ and $\begin{Bmatrix} p \\ q \\ r \end{Bmatrix}^b$. The propagation of the location coordinates can be expressed with the velocity as shown in Eq. (A.15). The local angular velocity is $\vec{\omega}^b$, and can be expressed in terms of the body rotation angle rates as given in Eq. (A.16). By utilizing transformations from the intermediate reference frames, the relationship between the body rotation angle rates and the angular velocities can be generated as shown in Eq. (A.17).

$$\begin{Bmatrix} \dot{x} \\ \dot{y} \\ \dot{z} \end{Bmatrix} = [R_{b\to e}] \begin{Bmatrix} u \\ v \\ w \end{Bmatrix} \tag{A.15}$$

$$\vec{\omega}^b = p\hat{b_1} + q\hat{b_2} + r\hat{b_3} = \dot{\Psi}\hat{e_3}' + \dot{\Theta}\hat{e_2}'' + \dot{\Phi}\hat{e_1}''' = \dot{\Psi}\hat{e_3} + \dot{\Theta}\hat{e_2}' + \dot{\Phi}\hat{b_1} \tag{A.16}$$

$$\begin{Bmatrix} p \\ q \\ r \end{Bmatrix} = \begin{bmatrix} -S\Theta & 0 & 1 \\ C\Theta S\Phi & C\Phi & 0 \\ C\Theta C\Phi & -S\Phi & 0 \end{bmatrix} \begin{Bmatrix} \dot{\Psi} \\ \dot{\Theta} \\ \dot{\Phi} \end{Bmatrix} \tag{A.17}$$

By applying Newton's and Euler's principles, the sum of the forces and the sum of the moments can be expressed as shown in Eqs. (A.18)-(A.19).

$$\sum \vec{F}^b = m \left[\begin{Bmatrix} \dot{u} \\ \dot{v} \\ \dot{w} \end{Bmatrix}^b + \vec{\omega}^b \times \vec{V}^b \right] \tag{A.18}$$

$$\sum \vec{M}^b = [I_{cg}] \begin{Bmatrix} \dot{p} \\ \dot{q} \\ \dot{r} \end{Bmatrix}^b + \vec{\omega}^b \times ([I_{cg}]\vec{\omega}^b) \tag{A.19}$$

The forces and moments that act upon the body come from the planing, the four fins, the cavitator, gravity, and the propulsive force F_{prop}.

Appendix B

Matlab Code

B.1 Partially Cavitating Vehicle Dynamics

```
%2/9/2009
%This code is setup so that the matrix algebra for the
    equations of motion
%are done within the odefunction.  This is required for the
    partial cavity
%simulations since the added mass terms cannot be simply
    added as forces
%since they affect acceleration (inertia matrix becomes
    dynamic).

clear;
close all;
clc;
global R L Rn L1 V M xcg Iyy rho T n g gcounter
    individualshift ycptrunc xcptrunc Lc r1;
gcounter=0;
```

```
%%%%%%%%BODY/RUN PARAMETERS
    %%%%%%%%%%%%%%%%%%%%%%%%%%%%%%%%%%%%%%%%%%%%%%
g = 9.81;
m = 2;       %density ratio
Rn = 0.0191;
R = 0.0508;
L = 1.8;

sigma=0.066925;
%sigma=0.046; %or 0.043 for using scax (supercav) to create
    partial cavity shape

n = 0.5;
Cx0 = 0.82;
Cx = Cx0*(1+sigma);
V = sqrt(0.03*75^2/sigma);

rho=1000;

L1=L/3; %length of the conical section of the body
L2=L-L1; %length of cylindrical section of body
```

```
r1=0; %radius of the front of the body


M=m*rho*pi*(R^2*L2+(R^3-r1^3)/(3*(R-r1))*L1);
xcg=1/4*(-3*R^2*L1^2+2*R*L1^2*r1+r1^2*L1^2+6*R^2*L^2)/(3*R
    ^2*L-2*R^2*L1+L1*R*r1+L1*r1^2);
xcg=-xcg;
Iyy=1/60*m*rho*(3*R^4+3*r1*R^3+12*R^2*L1^2+3*R^2*r1^2+6*R*r1
    *L1^2+3*R*r1^3+2*r1^2*L1^2+3*r1^4)*pi*L1+1/12*pi*R^2*(L-
    L1)*rho*m*(3*R^2+(L-L1)^2)+pi*R^2*(L-L1)*rho*m*(1/2*L
    +1/2*L1)^2;
T=.5*rho*pi*Rn^2*V*Cx;


%%%%%%%%%%%%%%CAVITY SHAPE MODEL
    %%%%%%%%%%%%%%%%%%%%%%%%%%%%%%%%%%%%%%%%%%%%%%%%%%%%%%%%
%data for initial cavity length vs. cavitation number to be
    converged upon
%for scax model
sigmafit=[0.03649 0.039992 0.042468 0.034994 0.03196
    0.029983 0.027951 0.025967 0.024977 0.045];
lengthfit=[50.934422 45.790226 42.768097 53.378616 59.052101
     63.461826 68.921989 74.727722 78.073776 40.031219];
```

```
cavlen=spline(sigmafit,lengthfit,sigma);


fid=fopen('body.dat','w');
fprintf(fid,'body.dat\nCONE\nC\nD\n');
fprintf(fid,'32\t16\t->MBOD, MEND\n');
fprintf(fid,'90.0\t0.5\t-> HALF CONE ANGLE (DEGREES), HEIGHT
    OF ENDPLATE\n');
fprintf(fid,[num2str(cavlen) '\t0.05\t-> CAVITY LENGTH,
    CAVITY NODE FACTOR (CJPT) TO DEFINE # OF NODES IN CAVITY\
    n']);
fprintf(fid,'1\t-> ITERATE ON CAVITATION NUMBER: 1=ITERATE,
    0=NOT ITERATE\n');
fprintf(fid,[num2str(sigma) '\t5.0E-5\t-> CAVITATION NUMBER
    TO BE CONVERGED ON,CONVERGENCE CRITERION\n']);
fprintf(fid,'1\t0.5\t-> 1-IF NON-DIMENSIONAL WITH BASE
    DIAMETR, BASE RADIUS OTHERWISE\n');
fprintf(fid,'2.0E-4\t-> EPS (EPSILON) for cavity length\n');
fprintf(fid,'0\t-> GRAVITY EFFECT: 1=ADD, 0=DO NOT ADD\n');
fprintf(fid,'104.0\t-> FROUDE NUMBER\n');
fprintf(fid,'0\t-> ANGLE OF ATTACK EFFECT: 1=ADD, 0=DO NOT
    ADD\n');
fprintf(fid,'10\t-> ANGLE OF ATTACK (IN DEGREES)\n');
```

```
fprintf(fid,'3.0E7\t-> REYNOLDS NUMBER');
fclose(fid);


%!scax.exe


%fid=fopen('control.xls'); %use this incase of using scax
fid=fopen('book1.csv'); %data from previous run for pscax
    sigma=0.066925;


Cd=str2num(fgetl(fid));
Mbod=str2num(fgetl(fid));
Mcav=str2num(fgetl(fid));
counter=1;
while(1)
    readstr=fgetl(fid);
    if readstr~=-1
        tester(counter,:)=str2num(readstr);
        counter=counter+1;
    else
        break
    end
end
```

```
fclose(fid);


xpos=tester(:,1);
ypos=tester(:,2);
xcp=[xpos(Mbod+1); tester(Mbod+1:Mcav+Mbod,3)]; %adds first
    x,y value to the cavity section of xcp/ycp data
ycp=[ypos(Mbod+1); tester(Mbod+1:Mcav+Mbod,4)];
%xcp=[x(Mbod+1); xcp];
%ycp=[y(Mbod+1); ycp];


normL=L/(Rn*2);                    %finds the normalized value
    for L
Lc=max(xcp)*Rn*2;
if L<Lc                            %only truncates if cavity length
    >L
    index=find(xcp<normL, 1, 'last' ); %finds the last x
        point index that is < L
    xcptrunc=[xcp(1:index); normL];        %integrates only
        up to length = L
    ycptrunc=[ycp(1:index); interp1(xcp,ycp,normL)];
else
    xcptrunc=xcp;
```

```
    ycptrunc=ycp;
end



%%%%%%CODE FOR MANUALLY MODIFIED CAVITY SHAPES %necessary
   when using
%%%%%%scax model to create partial cavity
if ycptrunc(end)*Rn*2 < R
    index=find((ycptrunc*Rn*2)>R,1,'last');
    xcptrunc=xcptrunc(1:index);
    ycptrunc=ycptrunc(1:index);
end
%%%%%%%%%%%%%%%%%%%%%%%%%%%%%%%%%%%%%%%%%%%%%%%

individualshift=-Cd/8*cumtrapz(xcptrunc,1./(ycptrunc.^2));

%%%%%ODE%%%%%INTEGRATION
   %%%%%%%%%%%%%%%%%%%%%%%%%%%%%%%%%%%%%%%%%%%%%%%%
delta_t=0.0001; x_init=[0.1 0.2 0 0]; i=1;
x_init=[0 0 0 0];
for t1=0:delta_t:1
    [t_state, x_state] = ode45(@ODEfunPC_mxinside_020809, [
```

```
        t1 t1+delta_t], x_init);
    x(i,:)=x_state(end,:);   t(1,i)=t_state(end);
    x_init=x_state(end,:);
    %size(t_state)
    clear x_state t_state;
    i=i+1
end

%
    ************************************************************

figure(1);
subplot(2,2,1);plot(t,x(:,1));ylabel('depth z (m)');grid on;
    xlabel('Time (s)');
subplot(2,2,2);plot(t,x(:,2));ylabel('velocity w (m/s)');
    grid on;xlabel('Time (s)');
subplot(2,2,3);plot(t,x(:,3));ylabel('pitch angle \theta (
    rad)');grid on;xlabel('Time (s)');
subplot(2,2,4);plot(t,x(:,4));ylabel('pitch rate q (rad/s)')
    ;grid on;xlabel('Time (s)');
function dxdt = ODEfunPC_mxinside_020809(t,x)
% 4-state model from Dzielski & Kurdila's paper
```

```
% x=[z w theta q]

global R L Rn L1 V M xcg Iyy rho T n g A B C D gcounter
    individualshift ycptrunc xcptrunc Lc r1;
%%%CREATING THE MX's FOR THE EOM%%%%%%%%%%%%%%%%%%%%%%%%%%%%%%%%%%%%%%%%%%%%
a11=T*(-1-n);
a12=M*V-T*n*L;
a21=-T*n*L;
a22=-M*xcg*V-T*n*L^2;

b11=-T*V*n;
b12=-T*V;
b21=-T*V*n*L;
b22=0;

if Lc<=L1          %cavity ends on forebody (which is
    truncated cone)
      c1=M*g-rho*g*pi(R^2*(L-L1)+1/3*(L1-Lc)*(R^3-((R-r1)/L1*
          Lc+r1)^3)/(R-((R-r1)/L1*Lc+r1)));
      c2=-M*g*xcg-rho*g*(1/4*pi*(R-r1)^2/L1^2*(L1^4-Lc^4)+2/3*
          pi*r1*(R-r1)/L1*(L1^3-Lc^3)+1/2*pi*r1^2*(L1^2-Lc^2)
          +1/2*pi*R^2*(L^2-L1^2)); %xcg is negative
```

```
    lamda22=-(c1-M*g)/g;
    lamda26=-(c2+M*g*xcg)/g;
    lamda66=rho*(1/5*pi*(R-r1)^2/L1^2*(L1^5-Lc^5)+1/2*pi*r1
        *(R-r1)/L1*(L1^4-Lc^4)+1/3*pi*r1^2*(L1^3-Lc^3)+1/3*pi
        *R^2*(L^3-L1^3));
elseif Lc<=L      %cavity ends on rear body (cylinder)
    c1=M*g-rho*g*pi*R^2*(L-Lc);
    c2=-M*g*xcg-.5*rho*g*pi*R^2*(L^2-Lc^2);
    lamda22=-(c1-M*g)/g;
    lamda26=-(c2+M*g*xcg)/g;
    lamda66=1/3*pi*rho*R^2*(L^3-Lc^3);
else              %cavity ends past body
    c1=M*g;
    c2=-M*g*xcg;
    lamda22=0;
    lamda26=0;
    lamda66=0;
end

d1=1;
d2=L;
```

```
%L1p=rho*pi*R^2;

M0=[M -M*xcg;-M*xcg Iyy];
A0=[a11 a12; a21 a22];
B0=[b11 b12; b21 b22];
C0=[c1;c2];
D0=[d1;d2];

%Added mass changes%%%%%%%%%%%%%%%%%%%%%%%%%%%%
M0=[M+lamda22 -M*xcg+lamda26;-M*xcg+lamda26 Iyy+lamda66];
%%%%%%%%%%%%%%%%%%%%%%%%%%%%%%%%%%%%%%%%%%%%%%%%

A2=M0\A0;
B2=M0\B0;
C2=M0\C0;
D2=M0\D0;

a22=A2(1,1); a24=A2(1,2); a42=A2(2,1); a44=A2(2,2);
b21=B2(1,1); b22=B2(1,2); b41=B2(2,1); b42=B2(2,2);
c2=C2(1,1);
d2=D2(1,1); d4=D2(2,1);
```

```
A=[0 1 -V 0; 0 a22 0 a24; 0 0 0 1; 0 a42 0 a44];

B=[0 0; b21 b22; 0 0; b41 b42];

C=[0;c2;0;0];

D=[0;d2;0;d4];

%

    %%%%%%%%%%%%%%%%%%%%%%%%%%%%%%%%%%%%%%%%%%%%%%%%%%%%%%%%%%%%%%%%%


C=[0;C2(1);0;C2(2)]; %now the second term in C2 is not = 0,
    especially with the bouyancy term, so it needs to be
    included unlike before


w = x(2,:);

delta_e = .12+.3*x(4,:);  %fin angle wrt body

%delta_e=.1;%passive fin input

%delta_c = -15*x(1,:)+30*x(3,:)+0.3*x(4,:); (Kurdila in JVC)

delta_c = 15*x(1,:)-30*x(3,:)-0.3*x(4,:);%-2*x(2,:)/V; %
    correction by Guojian Lin


alphacav=w/V+delta_c;
```

```
alpha=atan(w/V);


if (w>0)
    cavitycords=abs(-ycptrunc+individualshift*sin(alphacav)*
        cos(alphacav))*2*Rn;    %unnormalized cavity radii
        along planing location
else
    cavitycords=abs(ycptrunc+individualshift*sin(alphacav)*
        cos(alphacav))*2*Rn;
end
delta=abs(ycptrunc*2*Rn)-R;          %individual deltas (
    difference in radius of cavity vs body) unnormalized
xcords=xcptrunc*2*Rn;                %unnormalized x positions
bodycords=abs(xcords*tan(alpha))+R;


%refining mesh only where planing begins
index=find((bodycords>cavitycords).*(xcords>max(xcords)/3)
    ,1);  %finds first location of planing of the cylinder
    part of the body
if index>0   %if planing
    xcordsnew=linspace(xcords(index-2),xcords(end))';
```

```
    cavitycords=interp1(xcords,cavitycords,xcordsnew);
    delta=abs(interp1(xcords,ycptrunc,xcordsnew)*2*Rn-R);
    xcords=xcordsnew;                          %xcords becomes
       truncated to just the planing area
    bodycords=abs(xcords*tan(alpha))+R;
end

hdepths=(bodycords-cavitycords).*(bodycords>cavitycords);
        %finds immersion depths (only where body is planing
   )
if index>0          %only does this calculation if planing
    for j=1:length(xcords)       %requires "for" loop since
       delta+hdepths can =0 giving NaN
        if (bodycords(j)>cavitycords(j))     %calculation
           only where planing (on now truncated xcords)
            integrand(j)=2*delta(j)^2./(delta(j)+hdepths(j))
                ^3;
        else
            integrand(j)=0;
        end
    end
else
```

```
    integrand(1:length(xcords))=0;
end


hdots=V*sin(abs(alpha)-atan(diff(cavitycords)./diff(xcords))
    );%cavity angle = atan(diff(cavitycords)./diff(xcords))
FpnormNoncyl=-sum(diff(cumtrapz(xcords,integrand')).*hdots
    .^2)*sign(alpha);

%this DOES take into account the cavity slope. diff(cumtrapz
    ) gives the
%individual trapezoidal areas, this multiplied by hdot^2
    over that
%particular area gives the individual integral totals.
    summed up gives the
%entire planing force.

if FpnormNoncyl~=0
    xp=-sum(diff(cumtrapz(xcords,integrand'.*xcords)).*hdots
        .^2*sign(alpha))./FpnormNoncyl;
else
    xp=L;
```

```
end

gcounter=gcounter+1;

Fp=FpnormNoncyl*pi*rho*R^2;
%in original formulation these terms were accounted for
    within the D matrix
%and were therefore omitted from the planing force, in this
    formulation the
%D matrix is setup to handle the un-normalized planing force
    .

dxdt = A*x+B*[delta_e;delta_c]+C+D*Fp.*[1 1 1 (xp)/L]';
```

B.2 Maneuvering with the Non-Cylindrical Planing Model

```
clear
clc
close all

sigma=0.03;
%preamble used to setup all parameters needed for the
    function call.  it
```

```
%requires that sigma be specified in the workspace before
    calling.
global Rcdot Rp R V L A B C D Rn Rc gcounter individualshift
     ycptrunc xcptrunc;


%
    %%%%%%%%%%%%%%%%%%%%%%%%%%%%%%%%%%%%%%%%%%%%%%%%%%%%%%%%%%%%%%%%%


g = 9.81;
m = 2;
Rn = 0.0191;
R = 0.0508;
L = 1.8;



%sigma = 0.0335;  %0.035 or 0.03



%sigma=0.025;
%R=R*1.25;
%L=L*1.1;
```

```
n = 0.5;

Cx0 = 0.82;

Cx = Cx0*(1+sigma);

C = 1/2*Cx*Rn^2/R^2;

V = sqrt(0.03*75^2/sigma);


M0=[7/9 17*L/36; 17*L/36 11/60*R^2+133/405*L^2];

A0=C*V*[(1-n)/m/L -n/m; -n/m -n*L/m]+V*[0 7/9; 0 17*L/36];

B0=C*V^2*[-n/m/L 1/m/L; -n/m 0];

C0=[7/9; 17*L/36]*g;

D0=[1/m/L; 1/m];

D00=[1/m/L 0; 0 1/m/L];


% correction by Guojian Lin

A0=C*V*[(-1-n)/m/L -n/m; -n/m -n*L/m]+V*[0 7/9; 0 17*L/36];

B0=C*V^2*[-n/m/L -1/m/L; -n/m 0];


A2=inv(M0)*A0;

B2=inv(M0)*B0;

C2=inv(M0)*C0;

D2=inv(M0)*D0;
```

```
D22=inv(M0)*D00;

%data for initial cavity length vs. cavitation number to be
   converged upon
%for scax model
sigmafit=[0.03649 0.039992 0.042468 0.034994 0.03196
   0.029983 0.027951 0.025967 0.024977 0.045];
lengthfit=[50.934422 45.790226 42.768097 53.378616 59.052101
    63.461826 68.921989 74.727722 78.073776 40.031219];

%
   %%%%%%%%%%%%%%%%%%%%%%%%%%%%%%%%%%%%%%%%%%%%%%%%%%%%%%%%%%%%%%%%%%

a22=A2(1,1); a24=A2(1,2); a42=A2(2,1); a44=A2(2,2);
b21=B2(1,1); b22=B2(1,2); b41=B2(2,1); b42=B2(2,2);
c2=C2(1,1);
d2=D2(1,1); d4=D2(2,1);
d21=D22(1,1); d22=D22(1,2); d41=D22(2,1); d42=D22(2,2);

A=[0 1 -V 0; 0 a22 0 a24; 0 0 0 1; 0 a42 0 a44];
B=[0 0; b21 b22; 0 0; b41 b42];
C=[0;c2;0;0];
```

```
D=[0;d2;0;d4];
K=[0 0 0 0; -15 0 30 0.3];
K=[0 0 0 0; 15 0 -30 -0.3]; % corrected by Guojian Lin
%A=A+B*K;

%cavity model information
%sigma=.03*75^2/V^2;    %specific cavitator data from
    original model
%creates input file for scax code
cavlen=spline(sigmafit,lengthfit,sigma);

fid=fopen('body.dat','w');
fprintf(fid,'body.dat\nCONE\nC\nD\n');
fprintf(fid,'32\t16\t->MBOD, MEND\n');
fprintf(fid,'90.0\t0.5\t-> HALF CONE ANGLE (DEGREES), HEIGHT
    OF ENDPLATE\n');
fprintf(fid,[num2str(cavlen) '\t0.05\t-> CAVITY LENGTH,
    CAVITY NODE FACTOR (CJPT) TO DEFINE # OF NODES IN CAVITY\
    n']);
fprintf(fid,'1\t-> ITERATE ON CAVITATION NUMBER: 1=ITERATE,
    0=NOT ITERATE\n');
fprintf(fid,[num2str(sigma) '\t5.0E-5\t-> CAVITATION NUMBER
```

```
    TO␣BE␣CONVERGED␣ON,CONVERGENCE␣CRITERION\n']);
fprintf(fid,'1\t0.5\t->␣1-IF␣NON-DIMENSIONAL␣WITH␣BASE␣
    DIAMETR,␣BASE␣RADIUS␣OTHERWISE\n');
fprintf(fid,'2.0E-4\t->␣EPS␣(EPSILON)␣for␣cavity␣length\n');
fprintf(fid,'0\t->␣GRAVITY␣EFFECT:␣1=ADD,␣0=DO␣NOT␣ADD\n');
fprintf(fid,'104.0\t->␣FROUDE␣NUMBER\n');
fprintf(fid,'0\t->␣ANGLE␣OF␣ATTACK␣EFFECT:␣1=ADD,␣0=DO␣NOT␣
    ADD\n');
fprintf(fid,'10\t->␣ANGLE␣OF␣ATTACK␣(IN␣DEGREES)\n');
fprintf(fid,'3.0E7\t->␣REYNOLDS␣NUMBER');
fclose(fid);


!scax.exe


fid=fopen('control.xls');
Cd=str2num(fgetl(fid));
Mbod=str2num(fgetl(fid));
Mcav=str2num(fgetl(fid));
counter=1;
while(1)
    readstr=fgetl(fid);
    if readstr~=-1
```

```
        tester(counter,:)=str2num(readstr);
        counter=counter+1;
    else
        break
    end
end
fclose(fid);
%{
Cd=0.85167;
Mbod=32;
Mcav=203;
load tester.txt
%}
xpos=tester(:,1);
ypos=tester(:,2);
xcp=[xpos(Mbod+1); tester(Mbod+1:Mcav+Mbod,3)]; %adds first
   x,y value to the cavity section of xcp/ycp data
ycp=[ypos(Mbod+1); tester(Mbod+1:Mcav+Mbod,4)];
%xcp=[x(Mbod+1); xcp];
%ycp=[y(Mbod+1); ycp];

normL=L/(Rn*2);                    %finds the normalized value
```

```
    for L
index=max(find(xcp<normL));
xcptrunc=[xcp(1:index); normL];             %integrates only up
    to length = L
ycptrunc=[ycp(1:index); interp1(xcp,ycp,normL)];
%shiftCoeff=-Cd/8*trapz(xcptrunc,1./(ycptrunc.^2));       %
    normalized shift value w/o the sin(alpha)*cos(alpha) term
%unshiftedR=interp1(xcp,ycp,normL);
individualshift=-Cd/8*cumtrapz(xcptrunc,1./(ycptrunc.^2));
%%%%%%%%%%%%%END PREAMBLE
    %%%%%%%%%%%%%%%%%%%%%%%%%%%%%%%%%%%%%%%%%%%%%%%%%%%%%%%%%%%%%%%

global s x0 xf n m xf_index obst_cords obst_rs lowest
    lowestholder
lowest=inf;
lowestholder=[];
s=14;
m=2;
x0=[0 0 0 0 0]';
xf=[-20 0 0 0 80]';
xf_index=[1 5];
n=length(x0);
```

```
u_limit=[pi/2.5];
obst_cords=[-5 40];%coordinate of obstacle (z,x)
obst_rs=[6.5];
obst_rs=obst_rs.^2; %squares the radius for easier
    comparison in function

guessT=1.1;
guess_c=0.6;
guess_e=0;
guess=[ones(s,1)*guess_e;ones(s,1)*guess_c;guessT];
%data from previous run

options=optimset('Algorithm','interior-point','MaxFunEvals'
    ,80000,'TolCon',1e-3);%for fmincon
options=optimset('MaxFunEvals',10000);%for fminsearch/
    fminunc

UB=[ones(s*m,1)*u_limit;Inf];
LB=[-ones(s*m,1)*u_limit;0];
%for looper=1:10
tic
```

```
%[vars fval]= fminsearch(@objective_diveplane,guess),options
    );

Ainput=[eye(length(guess));-eye(length(guess))];
binput=[UB;-LB];

for looper=1:4
    [vars fval]= patternsearch(@objective_diveplane,guess,
        Ainput,binput);%,options);
    if fval<5
        guess=vars;
        obst_rs=(sqrt(obst_rs)+.5)^2;
    else
        break
    end
end
toc

%guess=vars;
%end
obst_rs
```

```
for i=1:m
    u(:,i)=vars((i-1)*s+1:s*i);
end
control=u;
T=vars(end);

control
T


delta_e=[];delta_c=[];
[int_t, int_x] = ode45(@dive_plane_noncyl,[0 T/s],x0,[],
   control(1,:));
delta_e=[delta_e;ones(length(int_t),1)*control(i,1)];
delta_c=[delta_c;ones(length(int_t),1)*control(i,2)];
times=T/s:T/s:T;
for i=2:length(times)
    [t, x] = ode45(@dive_plane_noncyl,[times(i-1) times(i)],
       int_x(end,:)',[],control(i,:));
    int_t=[int_t;t];
    int_x=[int_x;x];
    delta_e=[delta_e;ones(length(t),1)*control(i,1)];
```

```
    delta_c=[delta_c;ones(length(t),1)*control(i,2)];
end
K=[0 0 0 0; 0 0 0 -0.9]; %inner loop control law
tot_control=([delta_e'; delta_c']+K*int_x(:,[1 2 3 4])')'; %
   makes columns with [delta_e_tot, delta_c_tot]
delta_c_tot=tot_control(:,2);

%
   %%%%%%%%%%%%%%%%%%%%%%%%%%%%%%%%%%%%%%%%%%%%%%%%%%%%%%%%%%%%%%%%%

figure(1)
plot(int_x(:,5),int_x(:,1));xlabel('x (m)');ylabel('z (m)');
hold on
[t_inneronly, x_inneronly] = ode45(@dive_plane_noncyl,[0 T],
   x0,[],zeros(m,2));
plot(x_inneronly(:,5),x_inneronly(:,1),'--b');legend('inner 
   and outer loop','inner loop only')


%plots the obstacles
for i=1:length(obst_rs)
    xc=obst_cords(i,2);
```

```
    zc=obst_cords(i,2);
    rad=sqrt(obst_rs(i));
    xes=linspace(-rad,rad);
    z_plus=sqrt(rad^2-xes.^2)+obst_cords(i,1);
    z_minus=-sqrt(obst_rs(i)-xes.^2)+obst_cords(i,1);
    plot(xes+xc,z_plus,'r');plot(xes+xc,z_minus,'r');
end
legend('inner and outer loop','inner loop only','obstacle');

%plotting the body orientations
indexes=[find(int_t>int_t(end)*.20,1) find(int_t>int_t(end)
    *.40,1) find(int_t>int_t(end)*.65,1) length(int_t)];
ef=3;%enlargement factor
L=L*ef;R=R*ef;

xcordbody=[linspace(0,-L,4) linspace(-L,0,4)];
zcordbody=[0 R R R -R -R -R 0];

for i=1:length(indexes)
    theta=int_x(indexes(i),3);
    xpos=int_x(indexes(i),5);
    zpos=int_x(indexes(i),1);
```

```
xcord=xpos+xcordbody*cos(-theta)-zcordbody*sin(-theta);
zcord=zpos+zcordbody*cos(-theta)-(-xcordbody)*sin(-theta
    );
patch(xcord,zcord,'r')


w = int_x(indexes(i),2);
alphacav=w/V+delta_c_tot(indexes(i));
cavitycordstop=(ycptrunc+individualshift*sin(alphacav)*
    cos(alphacav))*2*Rn;
cavitycordsbottom=(-ycptrunc+individualshift*sin(
    alphacav)*cos(alphacav))*2*Rn;
xcords=-xcptrunc*2*Rn;


cavitycordstop=cavitycordstop*ef;cavitycordsbottom=
    cavitycordsbottom*ef;xcords=xcords*ef;


cavxt=xpos+xcords*cos(-theta+w/V)-cavitycordstop*sin(-
    theta+w/V);
cavzt=zpos+cavitycordstop*cos(-theta+w/V)-(-xcords)*sin
    (-theta+w/V);
cavxb=xpos+xcords*cos(-theta+w/V)-cavitycordsbottom*sin
    (-theta+w/V);
```

```
      cavzb=zpos+cavitycordsbottom*cos(-theta+w/V)-(-xcords)*
          sin(-theta+w/V);
      plot(cavxt,cavzt,'g');plot(cavxb,cavzb,'g')
end
L=L/ef;R=R/ef;
%
    %%%%%%%%%%%%%%%%%%%%%%%%%%%%%%%%%%%%%%%%%%%%%%%%%%%%%%%%%%%%%%%%%


figure(2);
subplot(2,2,1);plot(int_t,int_x(:,1));ylabel('depth z (m)');
    grid on;xlabel('time (s)');
subplot(2,2,2);plot(int_t,int_x(:,2));ylabel('velocity w (m/
    s)');grid on;xlabel('time (s)');
subplot(2,2,3);plot(int_t,int_x(:,3));ylabel('pitch angle \
    theta (rad)');grid on;xlabel('time (s)');
subplot(2,2,4);plot(int_t,int_x(:,4));ylabel('pitch rate q (
    rad/s)');grid on;xlabel('time (s)');

figure(3);
subplot(2,1,1);plot(int_t,delta_e);ylabel('Fin angle (rad)')
    ;title('Outer loop control only');xlabel('time (s)');
```

```
subplot(2,1,2);plot(int_t,delta_c);ylabel('Cavitator angle (
    rad)');title('Outer loop control only');xlabel('time (s)'
    );

figure(4)
subplot(2,1,1);plot(int_t,delta_c_tot);ylabel('Cavitator
    angle (rad), total');xlabel('time (s)');
subplot(2,1,2);plot(int_t(2:end),diff(delta_c_tot)./diff(
    int_t));ylabel('Cavitator angle rate (rad/s), total');
    xlabel('time (s)');

function val = objective_diveplane(var)
%var is split up into [x1(ts) x2(ts) ... xn(ts) u1(ts) u2(ts
    ) ... um(ts) T]
%the ts are split up to T/s, s is the number of steps
%n is the number of states, m is the number of control
    variables
%x0 are the initial states, xf is the final state and
%xf_index is the index of the final states that are desired
    to be fixed.
%for instance if only the first two states are desired to be
     fixed,
```

```
%xf_index=[1  2]

global s x0 xf m xf_index obst_cords obst_rs lowest
    lowestholder

for i=1:m
    u(:,i)=var((i-1)*s+1:s*i);
end
% creates a mx of x = [u1(1) u2(1) ... un(1);
%                      u1(2) u2(2) ... un(2);
%                            ...
%                      u1(s) x2(s) ... un(s);

T=var(end);

c=[];
totalx=[]; %keep track of entire trajectory

%equality constraints: dynamic constraints betweens states,
    and gluing
%constraint for x(s)=xf
```

```
%constraint for first x(1)
[t xtemp]=ode45(@dive_plane_noncyl,[0,T/s],x0,[],u(1,:));
x2=xtemp(end,:);
totalx=[totalx;xtemp];

%constraints to make sure w<6
for i=2:s
    [t xtemp]=ode45(@dive_plane_noncyl,[T/s*(i-1),T/s*(i)],
        x2',[],u(i,:));
    x2=xtemp(end,:);
    c=[c; abs(x2(2))-6];
    totalx=[totalx;xtemp];
end

%obstacle constraints
for i=1:length(obst_rs)
    closestdist=min((totalx(:,1)-obst_cords(i,1)).^2+((
        totalx(:,5)-obst_cords(i,2)).^2));
    c=[c; obst_rs(i)-closestdist];
end

c
```

```
%control bounds
for i=1:length(var)-1
    c=[c; abs(var(i))-pi/2.5];
end

%enforces final condition
ceq=xf(xf_index)-x2(xf_index)';
u
T
c
ceq

val=var(end) + 100*sum((c>0).*abs(c))+100*sum(abs(ceq));
val
if val<lowest
    lowest=val;
    lowestholder=var;
end
function dxdt = dive_plane_noncyl(t,y,u)
% 4-state model from Dzielski & Kurdila's paper
% x=[z w theta q]
```

```
global Rcdot R V L A B C D Rn Rc gcounter individualshift
    ycptrunc xcptrunc;

x=y(1:4,:);
w = x(2,:);
delta_e = 0;
%delta_c = -15*x(1,:)+30*x(3,:)+0.3*x(4,:); (Kurdila in JVC)
delta_c = 15*x(1,:)-30*x(3,:)-0.3*x(4,:);%-2*x(2,:)/V; %
    correction by Guojian Lin
delta_c=-0.9*x(4,:);

%delta_c=30*x(1,:)-60*x(3,:)-0.6*x(4,:);%applying true 2x
    feedback (affects
%cavity shape as well instead of just adding it into the A
    mx with
%A=A=B*K (where K contains the linear feedback law)

delta_c = delta_c+u(2);
delta_e = delta_e+u(1);

%delta_c = -30*x(3,:)-0.3*x(4,:);%-2*x(2,:)/V; %no depth
```

```
    feedback

%delta_c=0 %no feedback;

%delta_c=15*x(1,:)-30*x(3,:)-6*x(4,:);%bifurcation control
%delta_c = 15*x(1,:)-90*x(3,:)-0.9*x(4,:); %gain augmented
    feedback
alphacav=w/V+delta_c;

% if (w>0) %planes on bottom  Rcdot<0 so sgn(alpha)=sgn(w)
%       alpha = w/V;
% else  %planes on top
%       alpha = w/V;
% end
alpha=atan(w/V);

if (w>0)
     cavitycords=abs(-ycptrunc+individualshift*sin(alphacav)*
         cos(alphacav))*2*Rn;    %unnormalized cavity radii
         along planing location
else
```

```
    cavitycords=abs(ycptrunc+individualshift*sin(alphacav)*
        cos(alphacav))*2*Rn;
end
delta=abs(ycptrunc*2*Rn)-R;          %individual deltas (
    difference in radius of cavity vs body) unnormalized
xcords=xcptrunc*2*Rn;                %unnormalized x positions
%alphageometric = atan(w/V);
bodycords=abs(xcords*tan(alpha))+R;

%refining mesh only where planing begins
index=find((bodycords>cavitycords).*(xcords>max(xcords)/3)
    ,1);  %finds first location of planing of the cylinder
    part of the body
if index>0   %if planing
    xcordsnew=linspace(xcords(index-2),xcords(end))';
    cavitycords=interp1(xcords,cavitycords,xcordsnew);
    delta=abs(interp1(xcords,ycptrunc,xcordsnew)*2*Rn-R);
    xcords=xcordsnew;                        %xcords becomes
        truncated to just the planing area
    bodycords=abs(xcords*tan(alpha))+R;
end
```

```
hdepths=(bodycords-cavitycords).*(bodycords>cavitycords);
        %finds immersion depths (only where body is planing
    )
if index>0              %only does this calculation if planing
    for j=1:length(xcords)      %requires "for" loop since
        delta+hdepths can =0 giving NaN
        if (bodycords(j)>cavitycords(j))    %calculation
            only where planing (on now truncated xcords)
            integrand(j)=2*delta(j)^2./(delta(j)+hdepths(j))
                ^3;
        else
            integrand(j)=0;
        end
    end
else
    integrand(1:length(xcords))=0;
end


hdots=V*sin(abs(alpha)-atan(diff(cavitycords)./diff(xcords))
    );%cavity angle = atan(diff(cavitycords)./diff(xcords))
%hdots=V*sin(alpha);
```

```
FpnormNoncyl=-sum(diff(cumtrapz(xcords,integrand')).*hdots
    .^2)*sign(alpha);

%this DOES take into account the cavity slope. diff(cumtrapz
    ) gives the
%individual trapezoidal areas, this multiplied by hdot^2
    over that
%particular area gives the individual integral totals.
    summed up gives the
%entire planing force.

%FpnormNoncyl=-V^2*trapz(xcords,integrand)*sin(alpha)^2*sign
    (alpha);  %sign to get the proper sign on planing force
%this also assumes that the planing angle is alpha (does not
     take into
%account slope of cavity shape).  also alpha in this case
    takes into
%account the Rcdot term, is that right??

if FpnormNoncyl~=0
    %xp=-V^2.*trapz(xcords,integrand.*xcords).*sin(alpha)
        ^2.*sign(alpha)./FpnormNoncyl;  %effective point
```

```
        location of planing force (from front of vehicle)
    xp=-sum(diff(cumtrapz(xcords,integrand'.*xcords)).*hdots
        .^2*sign(alpha))./FpnormNoncyl;
else
    xp=L;
end



gcounter=gcounter+1;


n=FpnormNoncyl;


dxdt_4 = A*x+B*[delta_e;delta_c]+C+D*n.*[1 1 1 (xp)/L]';



theta=x(3,:);
dzdt=w*cos(theta)-V*sin(theta);
xdot=V*cos(theta)+w*sin(theta);


dxdt=[dzdt; dxdt_4([2 3 4],:); xdot];
```

B.3 Maneuvering with Delay and Impact Model

```
clc
clear
close all

global Rcdot Rp R V L A B C D delay V;
%%%%%%%%%%%%%%%%%%%%%%%%%%%%constants section
    %%%%%%%%%%%%%%%%%%%%%%%%%%%%%%%%%%%%%%%%
g = 9.81;
m = 2;
Rn = 0.0191;
R = 0.0508;
L = 1.8;
sigma = 0.0241;  %0.035 or 0.03
sigma=0.03;
n = 0.5;
Cx0 = 0.82;
Cx = Cx0*(1+sigma);
C = 1/2*Cx*Rn^2/R^2;
V = sqrt(0.03*75^2/sigma);

M0=[7/9 17*L/36; 17*L/36 11/60*R^2+133/405*L^2];
A0=C*V*[(1-n)/m/L -n/m; -n/m -n*L/m]+V*[0 7/9; 0 17*L/36];
```

```
B0=C*V^2*[-n/m/L  1/m/L; -n/m  0];

C0=[7/9;  17*L/36]*g;

D0=[1/m/L;  1/m];

D00=[1/m/L  0;  0  1/m/L];


% correction by Guojian Lin

A0=C*V*[(-1-n)/m/L -n/m; -n/m -n*L/m]+V*[0  7/9;  0  17*L/36];

B0=C*V^2*[-n/m/L  -1/m/L; -n/m  0];


A2=inv(M0)*A0;

B2=inv(M0)*B0;

C2=inv(M0)*C0;

D2=inv(M0)*D0;

D22=inv(M0)*D00;


K1 = L/Rn/(1.92/sigma-3)-1;

K2 = sqrt(1-(1-4.5*sigma/(1+sigma))*K1^(40/17));

Rc = Rn*(0.82*(1+sigma)/sigma)^0.5*K2;

Rp = (Rc-R)/R;

Rcdot = -20/17*(0.82*(1+sigma)/sigma)^0.5*V*(1-4.5*sigma/(1+
    sigma))*K1^(23/17)/K2/(1.92/sigma-3);
```

```
a22=A2(1,1); a24=A2(1,2); a42=A2(2,1); a44=A2(2,2);

b21=B2(1,1); b22=B2(1,2); b41=B2(2,1); b42=B2(2,2);

c2=C2(1,1);

d2=D2(1,1); d4=D2(2,1);

d21=D22(1,1); d22=D22(1,2); d41=D22(2,1); d42=D22(2,2);


A=[0 1 -V 0; 0 a22 0 a24; 0 0 0 1; 0 a42 0 a44];

B=[0 0; b21 b22; 0 0; b41 b42];

C=[0;c2;0;0];

D=[0;d2;0;d4];

K=[0 0 0 0; -15 0 30 0.3];

K=[0 0 0 0; 15 0 -30 -0.3]; % corrected by Guojian Lin

K=[0 0 0 0; 0 0 0 -0.9]; %changed to remove dependence on z
    or theta

%A=A+B*K; %this has the built in inner loop control already


%
    %%%%%%%%%%%%%%%%%%%%%%%%%%%%%%%%%%%%%%%%%%%%%%%%%%%%%%%%%%%%%%%%%%


delay=L/V;


global s x0 xf num_in xf_index obst_cords obst_rs u_init
```

```
s=14;

num_in=2;

x0=[0 0 0 0 0]';

xf=[-20 0 0 0 80]';

xf_index=[1 5];

%n=length(x0);

u_limit=[pi/2.5];

obst_cords=[-5 40];%coordinate of obstacle (z,x)

obst_rs=[6];

u_init=zeros(num_in,1);


obst_rs=obst_rs.^2; %squares the radius for easier
    comparison in function


guessT=.8;

guess_c=0;

guess_e=0;

guess=[ones(s,1)*guess_e;ones(s,1)*guess_c;guessT];


options = psoptimset('TolCon',1e-3);


UB=[ones(s*num_in,1)*u_limit;Inf];
```

```
LB=[-ones(s*num_in,1)*u_limit;0.1];
tic
%[vars fval]= fmincon(@objective_diveplane,guess
    ,[],[],[],[],LB,UB,[],options);
[vars fval exitflag]= patternsearch(@objective_diveplane,
    guess,[],[],[],[],LB,UB,[],options);
toc



for i=1:num_in
     u(:,i)=vars((i-1)*s+1:s*i);
end
control=u;
T=vars(end);


control
T


for i=1:num_in
     upp(i)=spline(0:T/s:T,[u_init(i);u(:,i)]);
end
```

```
sol = dde23(@(t,y,Z) dive_plane(t,y,Z,upp),[delay],@(t) [x0
    (1:4); sqrt(V^2+x0(2)^2)*t],[0 T],[]);
int_t=sol.x';
int_x=sol.y';



figure(1)
plot(int_x(:,5),int_x(:,1));xlabel('x (m)');ylabel('z (m)');
hold on


u_inner=zeros(s,m);
for i=1:num_in
     upp_inner(i)=spline(0:T/s:T,[u_init(i);u_inner(:,i)]);
end
sol_inner = dde23(@(t,y,Z) dive_plane(t,y,Z,upp_inner),[
    delay],@(t) [x0(1:4); sqrt(V^2+x0(2)^2)*t],[0 T],[]);
t_inneronly=sol_inner.x';
x_inneronly=sol_inner.y';


plot(x_inneronly(:,5),x_inneronly(:,1),'b--');
```

```
%plots the obstacles
for i=1:length(obst_rs)
    xc=obst_cords(i,2);
    zc=obst_cords(i,2);
    rad=sqrt(obst_rs(i));
    xes=linspace(-rad,rad);
    z_plus=sqrt(rad^2-xes.^2)+obst_cords(i,1);
    z_minus=-sqrt(obst_rs(i)-xes.^2)+obst_cords(i,1);
    plot(xes+xc,z_plus,'r');plot(xes+xc,z_minus,'r');
end
legend('inner and outer loop','inner loop only','obstacle')

figure(2);
subplot(2,2,1);plot(int_t,int_x(:,1));ylabel('depth z (m)');
    grid on;xlabel('time (s)');
subplot(2,2,2);plot(int_t,int_x(:,2));ylabel('velocity w (m/
    s)');grid on;xlabel('time (s)');
subplot(2,2,3);plot(int_t,int_x(:,3));ylabel('pitch angle \
    theta (rad)');grid on;xlabel('time (s)');
subplot(2,2,4);plot(int_t,int_x(:,4));ylabel('pitch rate q (
    rad/s)');grid on;xlabel('time (s)');
```

```
figure(3);
delta_c = ppval(upp(2),int_t);
delta_e = ppval(upp(1),int_t);
subplot(2,1,1);plot(int_t,delta_e);ylabel('Fin angle (rad)')
    ;title('Outer loop control only');xlabel('time (s)');
subplot(2,1,2);plot(int_t,delta_c);ylabel('Cavitator angle (
    rad)');title('Outer loop control only');xlabel('time (s)'
    );

figure(4)
tot_control=([delta_e'; delta_c']+K*int_x(:,[1 2 3 4])')'; %
    makes columns with [delta_e_tot, delta_c_tot]
delta_c_tot=tot_control(:,2);
subplot(2,1,1);plot(int_t,delta_c_tot);ylabel('Cavitator
    angle (rad), total');xlabel('time (s)');
subplot(2,1,2);plot(int_t(2:end),diff(delta_c_tot)./diff(
    int_t));ylabel('Cavitator angle rate (rad/s), total');
    xlabel('time (s)');
function val = objective_diveplane(var)
%var is split up into [u1(ts) u2(ts) ... um(ts) T]
%xf_index is the index of the final states that are desired
```

```
    to be fixed.
%for instance if only the first two states are desired to be
    fixed,
%xf_index=[1 2]

global s x0 xf num_in xf_index obst_cords obst_rs u_init
    delay V

for i=1:num_in
    u(:,i)=var((i-1)*s+1:s*i);
end
% creates a mx of x = [u1(1) u2(1) ... un(1);
%                      u1(2) u2(2) ... un(2);
%                            ...
%                      u1(s) x2(s) ... un(s);

T=var(end);

c=[];
totalx=[]; %keep track of entire trajectory

for i=1:num_in
```

```
    upp(i)=spline(0:T/s:T,[u_init(i);u(:,i)]);
end


%equality constraints: dynamic constraints betweens states,
   and gluing
%constraint for x(s)=xf


%constraint for first x(1)
sol = dde23(@(t,y,Z) dive_plane(t,y,Z,upp),[delay],@(t) [x0
   (1:4); sqrt(V^2+x0(2)^2)*t],[0 T],[]);
t=sol.x;
totalx=sol.y';


%constraint to make sure w<6
c=[c; max(abs(totalx(:,2)))-6];


%obstacle constraints
for i=1:length(obst_rs)
    closestdist=min((totalx(:,1)-obst_cords(i,1)).^2+((
       totalx(:,5)-obst_cords(i,2)).^2));
    c=[c; obst_rs(i)-closestdist];
end
```

```
xend=totalx(end,:);
%enforces final condition
ceq=xf(xf_index)-xend(xf_index)';

val=var(end) + 100*sum((c>0).*abs(c))+100*sum(abs(ceq));
u
T
c
ceq
val

function dxdt = dive_plane(t,y,Z,upp)
% 4-state model from Dzielski & Kurdila's paper
% x=[z w theta q x]

global Rcdot Rp R V L A B C D;
thetat=Z(3,1);
xt=Z(5,1);
zt=Z(1,1);
wt=Z(2,1);
thetact=thetat-atan(wt/V);
```

```
z=y(1,:);

w=y(2,:);

theta=y(3,:);

q=y(4,:);

x=y(5,:);

oldstates=y(1:4,:);


zdot=w*cos(theta)-V*sin(theta);

xdot=V*cos(theta)+w*sin(theta);


a=cos(thetact)*(x-xt)+sin(thetact)*(zt-z);

a=L*cos(theta-thetact); %this is necessary when dropping the
    delay close to 0

b=sin(thetact)*(x-xt)-cos(thetact)*(zt-z);

adot=xdot*cos(thetact)-zdot*sin(thetact);

bdot=xdot*sin(thetact)+zdot*cos(thetact);


hhat=a*tan(theta-thetact)+b; %this is the relative position
   of the body wrt cavity (can be neg or pos)

h=max([abs(hhat)-Rp*R,0]);  %this is the immersion depth,
   positive no matter what side is immersed
```

```
hdot=(a*sec(theta-thetact)^2*q+adot*tan(theta-thetact)+bdot)
    *sign(hhat)-Rcdot; %the multiplication by sign(hhat) is
    to make sure that the immesion rate is in the direction
    of the immersion
hdot=max(hdot,0); %the planing force formulation only works
    for an immerstion rate that is in the direction of the
    immersion so only positive immersion rates are available



delta=Rp*R;


if h>0
     Fplane=-hdot^2*1/tan(abs(theta-thetact)).*(1-delta^2./(h
         +delta).^2)*sign(hhat);
else
     Fplane=0;
end


delta_c = ppval(upp(2),t)-0.9*oldstates(4,:);
delta_e = ppval(upp(1),t);
```

```
n=Fplane;

dolddt = A*oldstates+B*[delta_e;delta_c]+C+D*n;


dxdt=[zdot; dolddt([2 3 4],:); xdot];
```

Bibliography

[1] S.S. Ahn. *An Integrated Approach to the Design of Supercavitating Underwater Vehicles*. PhD Thesis, Georgia Institute of Technology, August 2007.

[2] J. Awrejcewicz and M.M. Holicke. *Smooth and Nonsmooth High Dimensional Chaos and the Melnikov-type Methods*. Word Scientific Publishing, Hackensack, NJ, 2007.

[3] J. Awrejcewicz and C.H. Lamarque. *Bifurcation and Chaos in Nonsmooth Mechanical Systems*. Word Scientific Publishing, River Edge, NJ, 2003.

[4] D. Barrett, M. Grosenbaugh, and M. Triantafyllou. The optimal control of a flexible hull robotic undersea vehicle propelled by an oscillating foil. In *Autonomous Underwater Vehicle Technology, 1996. AUV '96., Proceedings of the 1996 Symposium on*, pages 1 –9, June 1996.

[5] C.E. Brennen. *Hydrodynamics of Pumps*. Concepts NREC, Junction, VT, 1994.

[6] I. Chakraborty and B. Balachandran. Off-resonance cantilever dynamics in the presence of attractive and repulsive tip-interaction forces. *International Journal of Structural Stability and Dynamics*, 11(4):603 – 620, 2011.

[7] J. Dzielski. Planing model discrepancies. 2004. private communication.

[8] J. Dzielski and A. Kurdila. A benchmark control problem for supercavitating vehicles and an initial investigation of solutions. *Journal of Vibrations and Control*, 9:791–804, 2003.

[9] P. Encarnacao and A. Pascoal. 3d path following for autonomous underwater vehicle. In *Proceedings of the 39th IEEE Conference on Decision and Control, Sydney, Australia*, 2000.

[10] E. Esmailzadeh, A. Goodarzi, and G. R. Vossoughi. Optimal yaw moment control law for improved vehicle handling. *Mechatronics*, 13(7):659 – 675, 2003.

[11] E. Frazzoli, M.A. Dahleh, and E. Feron. A hybrid control architecture for aggressive maneuvering of autonomous helicopters. In *Decision and Control, 1999. Proceedings of the 38th IEEE Conference on*, 1999.

[12] E. Frazzoli, M.A. Dahleh, and E. Feron. Robust hybrid control for autonomous vehicle motion planning. In *Decision and Control, 2000. Proceedings of the 39th IEEE Conference on*, 2000.

[13] A. Goel. *Control Strategies for Supercavitating Vehicles*. Masters Thesis, University of Florida, 2002.

[14] S. Hassan. Analysis of hydrodynamic planing forces associated with cavity riding vehicles. 1999. private communication.

[15] M. A. Hassouneh, B. Balachandran, and E. H. Abed. Delay effects in supercavitating vehicle dynamics. *ASME Conference Proceedings*, 2009(49019):653–660, 2009.

[16] M.A. Hassouneh, V. Nguyen, B. Balchandran, and E. H. Abed. Analysis, control, and maneuvering of supercavitating vehicles. In *Proceedings of the ASME International Mechanical Engineering Congress and Exposition, Vancouver, British Columbia, Canada*, Vancouver, British Columbia, Canada, November 2010.

[17] T. Kalmr-Nagy, R. D'Andrea, and P. Ganguly. Near-optimal dynamic trajectory generation and control of an omnidirectional vehicle. *Robotics and Autonomous Systems*, 46(1):47 – 64, 2004.

[18] T. Kiceniuk. An experimental study of the hydrodynamic forces acting on a family of cavity producing conical bodies of revolution inclined to the flow. Technical Report CIT Hydrodynamic Report E-12.17, California Institute of Technology, Pasadena, CA, 1954.

[19] I.N. Kirschner, J.S. Uhlman., A.N. Varghese, and I.M. Kuria. Supercavitating projectiles in axisymmetric subsonic liquid flows. In J. Katz and Y. Matsumoto, editors, *Proceedings of the ASME & JSME Fluids Engineering Annual Conference & Exhibition, Cavitation and Multiphase Flow Forum, FED 210*, 1995. , Hilton Head Island, SC.

[20] I. Kirshner, B. Rosenthal, and J. Uhlman. Simplified dynamical systems analysis of supercavitating high-speed bodies. In *Fifth International Symposium on Cavitation (CAV2003), Osaka, Japan*, 2003.

[21] M. Kunze. *Non-smooth Dynamical Systems*. Springer, New York, 2000.

[22] L. Lapierre, D. Soetanto, and A. Pascoal. Nonlinear path following with applications to the control of autonomous underwater vehicles. In *Proceedings of the 42nd IEEE Conference on Decision and Control, Maui, HI USA*, 2003.

[23] R.I. Leine and H. Nijmeijer. *Dynamics and Bifurcations of Non-smooth Mechanical Systems*. Springer, New York, 2004.

[24] Z. Li, Y. Soh, and C. Wen. *Switched and Impulsive Systems*. Springer, Berlin, 2005.

[25] C. M. Liao, B. Balachandran, M. M. Karkoub, and Y. L. Abdel-Magid. Drillstring dynamics: Reduced-order models and experimental studies. *ASME-Journal of Vibration and Acoustics*, 133, 2011.

[26] G. Lin and B. Balachandran. E.H. Abed. Absolute stability of second-order systems with asymmetric sector boundaries. *Automatic Control, IEEE Transactions on*, 55(2):458 –463, Feb. 2010.

[27] G. Lin, B. Balachandran, and E. Abed. Dynamics and controls of supercavitating bodies. In *Proceedings of the ASME International Mechanics Engineering Congress and Exposition, Anaheim, CA*, Anaheim, California, November 2004.

[28] G. Lin, B. Balachandran, and E. Abed. Bifurcation behavior of a supercavitating vehicle. In *Proceedings of the ASME International Mechanical Engineering Congress and Exposition, Chicago, IL*, Anaheim, California, 2006.

[29] G. Lin, B. Balachandran, and E. Abed. Nonlinear dynamics and bifurcations of a supercavitating vehicle. *IEEE journal of Oceanic Engineering*, 32:753–761, 2007.

[30] G. Lin, B. Balachandran, and E. Abed. Dynamics and control of supercavitating vehicles. *ASME Journal of Dynamic Systems, Measurements, and Control*, 130:021003–1–021003–11, 2008.

[31] G.V. Logvinovich. *Hydrodyanmics of Free-Boundry Flows*. Translated from Russian, Kiev, 1969.

[32] G.V. Logvinovich. Some problems in planing surfaces. *Trudy TsAGI*, 2052, 1980. , translated from Russian.

[33] X.H. Long, G. Lin, and B. Balachandran. Grazing bifurcations in an elastic struction excited by harmonic impactor motions. *Physica D*, 237:1129–1138 fd, 2007.

[34] V. Nguyen and B. Balachandran. Supercavitating vehicles with noncylindrical, nonsymmetric cavities: Dynamics and instabilities. *Journal of Computational and Nonlinear Dynamics*, 6(4):041001, 2011.

[35] V. Nguyen, B. Balachandran, and A. Varghese. Supercavitating vehicle dynamics with non-cylindrical, non-symmetric cavities. In *Proceedings of the ASME International Mechanical Engineering Congress and Exposition*, Seattle, Washington, November 11-15 2007.

[36] M. Numatsu, H. Yabuno, A. Dick, M. Kuroda, K. Ashida, and B. Balachandran. Control of an impacted cantilever to maintain a constant magnitude for specific frequency component of the response. In *Proceedings of the ASME 2007 International Design Engineering Technical Conference, Las Vegas, NV USA*, 2007.

[37] E. Paryshev. Mathematical modeling of unsteady cavity flows. In *Fith International Symposium on Cavitation (CAV2003), Osaka, Japan*, 2003.

[38] M.S. Queiroz, M. Malisoff, and P. Wolenski. *Optimal Control, Stabilization and Nonsmooth Analysis*. Springer, Berlin, 2004.

[39] M. Ruzzene, R. Kamada, C.L. Bottasso, and F. Scorcelletti. Trajectory optimization strategies for supercavitating underwater vehicles. *Journal of Vibrations and Control*, 14(5):611–644, 2008.

[40] Y.N. Savchenko. Supercavitation - problems and perspectives. In *Fourth International Symposium on Cavitation (CAV2001), Pasedena, CA USA*, 2001.

[41] G. Tao and F. L. Lewis. *Adaptive Control of Nonsmooth Dynamical Systems*. Springer, London, 2001.

[42] J.S. Uhlman, A.N. Varghese, and I.N. Kirschner. Boundary element modeling of axisymmetric supercavitating bodies. In *Proceedings of the 1st Symposium on Marine Applications of Computational Fluid Dynamics, Hydrodynamic/Hydroacoustic Technology Center, Mclean, VA.*, Hydrodynamic/Hydroacoustic Technology Center, Mclean, VA, 1998.

[43] B. Vanek, J. Bokor, G. J. Balas, and R. E. Arndt. Longitudinal motion control of a high-speed supercavitation vehicle. *Journal of Vibration and Control*, 13(2):159–184, 2007.

[44] A.N. Varghese, J.S. Uhlman, and I.N. Kirschner. High-speed bodies in partially cavitating axisymmetric flow. In *Fifth International Symposium on Cavitation (CAV2003), Osaka, Japan*, 2003.